

REMOTE LASER SPECTROSCOPY
AT STANDOFF DISTANCES
FOR HERITAGE APPLICATIONS

YU LI

A thesis submitted in partial fulfilment of the
requirements of Nottingham Trent University
for the degree of Doctor of Philosophy

June 2022

Copyright statement

The copyright in this work is held by the author. You may copy up to 5% of this work for private study, or personal, non-commercial research.

Any re-use of the information contained within this document should be fully referenced, quoting the author, title, university, degree level and pagination.

Queries or requests for any other use, or if a more substantial copy is required, should be directed to the author.

To the memory of my father

Abstract

In this project, remote standoff laser spectroscopy systems working at 3–15 m have been developed for cultural heritage research, employing Raman spectroscopy, laser induced breakdown spectroscopy (LIBS), and laser induced fluorescence spectroscopy (LIF). To address the problems encountered during *in situ* analysis due to environmental restrictions, the adoption of remote techniques offers advantages such as convenient deployment on the ground, allowing sensitive measurements over long integration time and there is no need to redeploy for different areas of interest. The research focuses on the design and development of remote standoff laser spectroscopy systems with special needs in heritage research considered, as well as their application for *in situ* analysis.

A remote standoff Raman system was developed and optimised. It is the first of its kind that is dedicated to cultural heritage research. It can identify most of common historic artist pigments. A daylight subtraction procedure enables the remote standoff Raman system to operate in the presence of indoor ambient light. Laser induced degradation effect was studied using various laser configurations on a range of common pigments. The remote standoff Raman system is proved to be safe for the analysis of most pigments tested when using typical integration time required for Raman measurements. *In situ* remote macro-Raman mapping is achieved in two field campaigns, revealing the pigments distribution on wall paintings and salt distribution in historical buildings in coastal environments.

A remote standoff LIBS system was developed. Assisted with Raman and reflectance spectroscopy, a multimodal approach allowing *in situ* standoff depth-resolved material identification of wall paintings was demonstrated for the first time. The combined elemental, molecular and reflectance information contributes to a more complete data

interpretation. Consequently, the stratigraphy of whitewashed wall paintings was successfully uncovered in a unique field campaign.

Acknowledgments

I would like to express my gratitude to my direct of studies, Prof Haida Liang, who guided me throughout this research project. I would also like to show my appreciation to my second supervisors, Dr Quentin Hanley and Dr Golnaz Shahtahmassebi, for their help and support during this study.

The funding by Nottingham Trent University for my PhD studentship that enabled the development of the remote standoff laser spectroscopy systems is greatly appreciated. I would also like to thank the Institute of Physics (IOP) for the Bell Burnell Graduate Scholarship Fund (BBGSF) Covid-19 Hardship Fund Award, which supported me through tough times during the pandemic.

I wish to extend my special thanks to the whole team of the ISAAC research centre. The support I have had in studying and living from every member has always been brilliant. In particular, I would like to express my gratitude to Dr Sammy Cheung, who instructed me in the research and helped me a lot in many aspects of my life. I will never forget the happy hours we shared on the football pitch.

My sincere thanks also go to my colleagues and collaborators for their help in field campaigns: 1) Dr Ana Souto of Nottingham Trent University, and Fr Philip McBrien of the Diocesan Art and Architecture Commission for the information on the architectural background of the Cathedral Church of St Barnabas, Nottingham. 2) Mr. Stig Evans for arranging the field campaign in the Royal Pavilion in Brighton. 3) Dr David Thickett of English Heritage for arranging the field campaign for salt damage analysis in Fort Brockhurst, Gosport. 4) Dr Lucas Goehring of Nottingham Trent University for arranging the field campaign in the Convent of Mercy, Nottingham.

I would also like to thank my family and friends for their endless love, support, and encouragement throughout my pursuit for education. I hope this achievement will fulfil the dream they envisioned for me.

List of publications

1. Yu Li, Chi Shing Cheung, Sotiria Kogou, Florence Liggins, and Haida Liang. “Standoff Raman spectroscopy for architectural interiors from 3-15 m distances.” *Optics Express* 27, no. 22 (2019): 31338-31347.
2. Yu Li, Chi Shing Cheung, Sotiria Kogou, Alex Hogg, Haida Liang, and Stig Evans. “Standoff laser spectroscopy for wall paintings, monuments, and architectural interiors”. In *Transcending Boundaries: Integrated Approaches to Conservation. ICOM-CC 19th Triennial Conference Preprints*, Beijing, 17–21 May 2021, ed. J. Bridgland. Paris: International Council of Museums.
3. Yu Li, Amelia Suzuki, Chi Shing Cheung, Yuda Gu, Sotiria Kogou, and Haida Liang. "A study of potential laser-induced degradation in remote standoff Raman spectroscopy for wall paintings." *The European Physical Journal Plus* 137, no. 10 (2022): 1102.
4. Yu Li, Sotiria Kogou, Amelia Suzuki, Chi Shing Cheung, Haida Liang. “Uncovering stratigraphy of whitewashed historical wall paintings: *in situ* depth-resolved material identification using multimodal remote standoff spectroscopies” (to be submitted)

Table of Contents

Chapter 1: Introduction	5
1.1. Fundamentals	5
1.1.1. Raman spectroscopy	5
1.1.2. Laser induced breakdown spectroscopy (LIBS)	9
1.1.3. Laser induced fluorescence (LIF)	15
1.2. Challenges of <i>in situ</i> cultural heritage research	18
1.3. Literature review of remote laser spectroscopy techniques	21
1.3.1. Raman spectroscopy	21
1.3.2. LIBS	25
1.3.3. LIF	29
1.3.4. Multimodal analysis.....	31
Chapter 2: Instrumentation	36
2.1. Remote standoff Raman spectroscopy	36
2.1.1. Introduction.....	36
2.1.2. Original experimental setup.....	38
2.1.3. Sources of noise	40
2.1.4. Choice of excitation wavelength.....	42
2.1.5. Raman efficiency comparison between CW and pulsed laser	44
2.1.6. Experimental updates.....	47
2.1.7. Signal processing	48

2.1.7.1. Wavelength/wavenumber calibration	48
2.1.7.2. Background subtraction and spectral response correction.....	52
2.1.8. Daylight subtraction	52
2.1.9. Pigment survey	54
2.2. LIBS	56
2.2.1. Introduction	56
2.2.2. Instrumental design	58
2.2.3. Signal processing.....	61
2.2.4. Pigment survey	63
2.2.5. Depth-profiling analysis	65
2.3. LIF	69
2.3.1. Introduction	69
2.3.2. Experimental setup	70
2.3.3. Pigment survey	72
2.4. Conclusions	75
Chapter 3: Laser induced degradation of paints	76
3.1. Introduction	76
3.2. Intensity and fluence comparison of common laser techniques	78
3.3. Selection of pigment samples	79
3.4. Experimental setup and procedure.....	81
3.5. A comparison of degradation induced by three laser sources	84
3.5.1. CW versus pulse laser at 532 nm	91
3.5.2. CW lasers at 532 nm versus 780 nm	92

3.6. 780 nm CW laser induced degradation effects on a range of common pigments	93
3.7. Sensitivity of Raman spectroscopy for monitoring laser-induced degradation effects...	97
3.8. Conclusions	100
Chapter 4: Applications of remote standoff Raman spectroscopy	102
4.1. Standoff <i>in situ</i> analysis of painting materials at the St Barnabas Cathedral, Nottingham	102
4.1.1. Complementary methods	103
4.1.2. Analysis of painting materials	104
4.2. Standoff <i>in situ</i> investigation of wall paintings at the Convent of Mercy, Nottingham..	109
4.3. Remote standoff macro-Raman mapping.....	112
4.3.1. Hardware control for scanning.....	112
4.3.2. Macro-Raman mapping: Wall paintings at the Brighton pavilion	115
4.4. Standoff <i>in situ</i> investigation of salt damage at Fort Brockhurst.....	119
4.4.1. Mock-up experiments in laboratory environment.....	120
4.4.2. <i>In situ</i> analysis of salts in Fort Brockhurst	123
4.5. Conclusions	133
Chapter 5: Remote standoff depth-resolved multimodal spectroscopic analysis..	134
5.1. Introduction.....	134
5.2. Remote standoff spectroscopy system for multimodal analysis	136
5.3. Laboratory evaluation of remote standoff multimodal spectral analysis	140
5.4 <i>In situ</i> analysis of wall paintings.....	152
5.5. Interpretation of the wall painting structure.....	159
5.6. Conclusions	163

Chapter 6: Conclusions	164
Bibliography	171
Appendix 1: Pigment survey	197
Appendix 2: Laser safety	199

Chapter 1

Introduction

1.1. Fundamentals

1.1.1. Raman spectroscopy

When a beam of light impinges on the molecule, most of the deflected photons remains unchanged in energy. This dominant process is regarded as elastic scattering, or Rayleigh scattering. However, the energy of a very small amount of scattered photons (only one in every $10^6 - 10^8$ photons) will differ from the original state due to the interaction between the incident light and the molecule. The energy exchange results from the inelastic scattering process. This weak process is discovered by the Indian physicist Sir Chandrasekhar Venkata Raman in 1928 [1], therefore named after him as the Raman effect. For this work, he was awarded the 1930 Nobel Prize in Physics. The Raman effect is so weak that when it was first discovered, it might take a whole day to record a spectrum when using filtered sunlight for excitation. It was only when the laser was invented in 1960s and low noise and high quantum efficiency (QE) detectors emerged since 1980s that Raman spectroscopy became an increasingly prevalent technique.

The Raman effect can be viewed as the inelastic scattering of electromagnetic radiation. During this interaction, energy transfer between the photons and the molecular vibrations occurs, resulting in the scattered photons possess a different energy when compared with the incident photons.

In the classical description, Raman scattering results from a change in polarisability with the motion (vibrational or rotational) of the molecule [2,3]. When a molecule is situated

in an electric field \mathbf{E} of the incident light, an electrical dipole moment \mathbf{p} is induced and the scattered light is radiated. The relation between the electrical field and the induced dipole moment can be expressed as a power series in Equation (1.1):

$$\mathbf{p} = \alpha \cdot \mathbf{E} + \frac{1}{2}\beta \cdot \mathbf{E}^2 + \frac{1}{6}\gamma \cdot \mathbf{E}^3 + \dots \quad (1.1)$$

where α , β , and γ are tensors, named as polarisability, hyperpolarisability and 2nd hyperpolarisability, respectively. Since each tensor is 10 orders of magnitude weaker than the previous one, hyperpolarisability and 2nd hyperpolarisability can be neglected, thus the polarisability is typically approximated by the first polarisability tensor, α . Equation (1.1) can then be rewritten, due to the first order approximation of the polarisability function, as in Equation (1.2):

$$\mathbf{p} = \alpha \cdot \mathbf{E} \quad (1.2)$$

where the induced dipole moment \mathbf{p} can be therefore considered as directly proportional to the electrical field \mathbf{E} . Light can be regarded as an oscillating electrical field, thus the electric field vector at time t can be expressed as in Equation (1.3):

$$\mathbf{E} = \mathbf{E}_0 \cdot \cos(2\pi\nu_0 t) \quad (1.3)$$

where ν_0 is the vibrational frequency of the electromagnetic radiation.

The polarisability α depends on the chemical bonds, of which the shape and dimension change during the vibrations of the molecule. A Taylor expansion can be performed on α , as in Equation (1.4):

$$\alpha = \alpha_0 + \sum_k \left(\frac{\partial \alpha}{\partial Q_k} \right)_0 \cdot Q_k + \frac{1}{2} \sum_{k,l} \left(\frac{\partial^2 \alpha}{\partial Q_k \partial Q_l} \right)_0 \cdot Q_k \cdot Q_l + \dots \quad (1.4)$$

which describes the total polarisability along the given normal coordinates, Q_k , Q_l , etc. Q_k and Q_l are related to the k^{th} and l^{th} normal vibrations with the vibrational frequencies ν_k and ν_l , respectively.

Remembering that the electric field is assumed to be harmonic oscillator, the normal coordinate oscillates accordingly, as in Equation (1.5):

$$Q_v = Q_{v0} \cdot \cos(2\pi\nu_v t + \varphi_v) \quad (1.5)$$

where Q_{v0} is the amplitude of the normal vibration, and φ_v a phase angle. ν_v is the vibrational frequency of the normal coordinate of the molecule in the harmonic oscillation.

The first approximation of the polarisability function maintains the first two terms. Equation (1.5) can then be substituted into Equation (1.4) and then combined with Equation (1.3) to yield a fully expanded expression of the simplified definition of the dipole moment \mathbf{p} (Equation (1.2)) as in Equation (1.6):

$$\mathbf{p} = \alpha_0 \cdot \mathbf{E}_0 \cdot \cos(2\pi\nu_0 t) + \alpha'_v \cdot \mathbf{E}_0 \cdot Q_{v0} \cdot \cos(2\pi\nu_0 t) \cos(2\pi\nu_v t + \varphi_v) \quad (1.6)$$

where $\alpha'_v = \left(\frac{\partial \alpha}{\partial Q_v} \right)_0$.

Considering that $\cos \alpha \cdot \cos \beta = \frac{1}{2} \cos(\alpha - \beta) + \frac{1}{2} \cos(\alpha + \beta)$, Equation (1.6) can be transformed into Equation (1.7):

$$\begin{aligned} \mathbf{p} = & \alpha_0 \cdot \mathbf{E}_0 \cdot \cos(2\pi\nu_0 t) \\ & + \frac{1}{2} \alpha'_v \cdot \mathbf{E}_0 \cdot Q_{v0} \cdot \cos[2\pi(\nu_0 - \nu_v)t - \varphi_v] \\ & + \frac{1}{2} \alpha'_v \cdot \mathbf{E}_0 \cdot Q_{v0} \cdot \cos[2\pi(\nu_0 + \nu_v)t + \varphi_v] \quad (1.7) \end{aligned}$$

The first term corresponds to elastic scattering of the Electromagnetic radiation, or Rayleigh scattering. The second and third term represent the inelastic part of light scattering (Figure 1.1). The second term gives rise to new frequency at $\nu_0 - \nu_v$ (Stokes scattering), which relates to a lower energy of the scattered radiation when compared with the incident light, while the third term leads to higher frequency at $\nu_0 + \nu_v$ (anti-Stokes scattering).

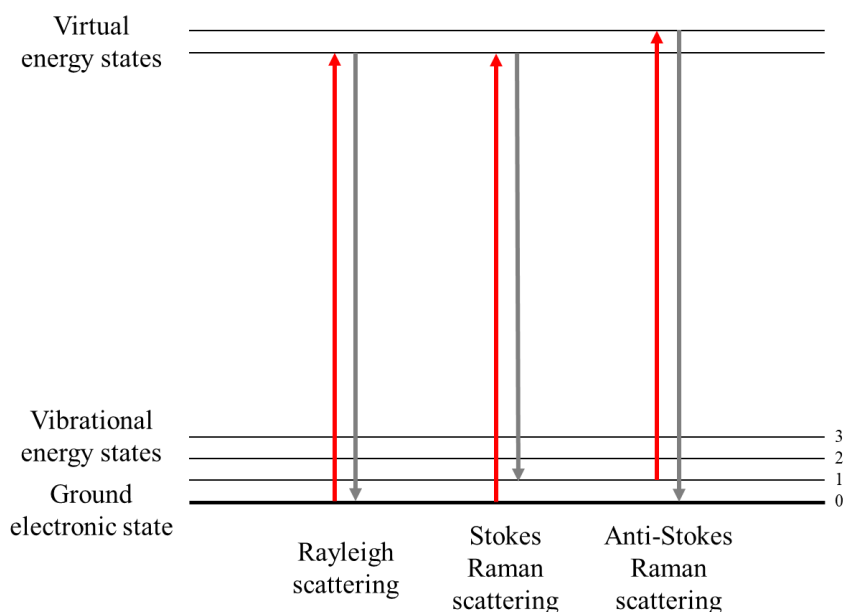


Figure 1.1. Energy level diagram of Raman and Rayleigh scattering.

From Equation (1.7), it can be seen that an essential requirement for Raman effect is that $\alpha'_v \neq 0$ so that the 2nd and 3rd terms in Equation (1.7) are non-zero. The basic selection rule is that Raman scattering results from a change in polarisability in the molecule during the normal vibration, as shown in Equation (1.8):

$$\alpha'_v = \left(\frac{\partial \alpha}{\partial Q_v} \right)_0 \neq 0 \quad (1.8)$$

The position of a Raman signal (Raman shift) in the spectrum depends on the energy gap between the ground state and the first vibrationally excited state. In a simplified approach, the bonding of a diatomic molecule can be considered as a vibrating spring, therefore Hooke's law can be applied [4]. Using the harmonic oscillation approximation, the vibrational frequency is:

$$\nu = \frac{1}{2\pi \cdot c} \sqrt{\frac{\kappa}{\mu}} \quad (1.9)$$

where two factors determine the Raman band position: the force constant of the bond and the type of vibration (κ) and the reduced mass ($\mu = \frac{m_1 \cdot m_2}{m_1 + m_2}$). Therefore, Raman signals from lighter atoms usually occur at higher frequency. The force constant is a measure of the bond strength and is heavily influenced by the inter- and intramolecular interactions, thus stronger bonds yield higher frequency.

1.1.2. Laser induced breakdown spectroscopy (LIBS)

Laser induced breakdown spectroscopy (LIBS) is an analytical technique that focuses a high-energy laser pulse to ablate a small piece of the sample and thus creates a plasma. The electrons from the atoms and ions at the excited electronic states decay when the plasma cools down, bringing about light emission. The fingerprint spectral feature consisting of multiple discrete narrowband emission lines allows qualitative elemental analysis. The intensity of the lines, measured at each element's characteristic wavelength, is proportional to the concentration of that element in the plasma, enabling quantitative analysis as well as elemental identification.

The laser was invented in 1960. Shortly afterwards, Brech and Cross firstly demonstrated the formation of a laser-induced plasma [5]. This discovery resulted quickly to the

emergence of LIBS. In 1964, Runge developed the LIBS approach [6]. In the early stages of LIBS development, the scientific community's focus was largely on the underlying physics of plasma formation. LIBS gained traction during the 1990s as lasers, detectors and spectrographs used in LIBS equipment improved. LIBS has been widely applied to many areas, including material inspection, metal recycling, quality control, environmental survey, explosives detection, biomedical, pharmaceutical, and archaeology.

Understanding the physics behind the plasma formed during the laser-matter interaction is crucial to determine the optimal experimental parameters and therefore to better process the data. LIBS is such a sensitive analytical technique that its signal depends strongly on the experimental conditions, including the laser parameters (predominantly pulse fluence and pulse duration), sample surface condition, and surrounding atmosphere. Here the focus is on plasma formation and atomic emission spectroscopy (AES), linking the physical phenomenon and the observed spectra. The discussion will be mainly on nanosecond pulsed lasers and for solids (as the main concern is for painting materials).

The irradiance of the laser beam must be above a certain threshold before it can create plasma on the sample. The threshold values typically range from a few GW/cm^2 to hundreds of GW/cm^2 and differ from one material to another. They are also affected by laser wavelength and pulse width [7]. The threshold sets certain requirements for laser sources used in LIBS. A pulsed laser is typically required to achieve the requisite irradiance on the sample surface. To further increase the irradiance above the threshold, the pulsed beam is usually focused by a lens.

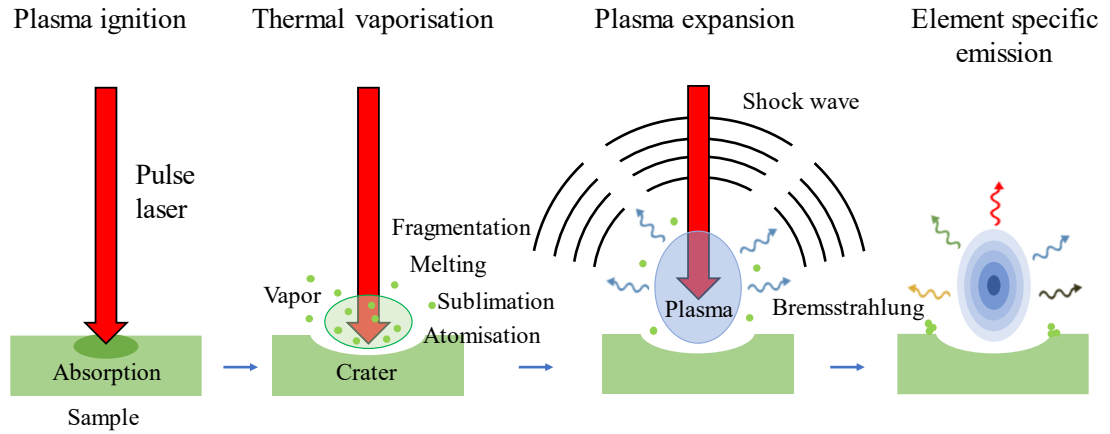


Figure 1.2. Main events in the plasma formation process on solid sample.

When a laser pulse is focused on a sample, the material absorbs the energy from the beam and is ablated. During the period, complex laser-matter interactions including fragmentation, atomisation, vaporisation, sublimation, and melting all contribute to the formation of a crater on the laser spot. There are two steps for plasma breakdown: the creation of some initial free electrons and then the rapid ionisation. Thermionic emissions, which generate free electrons above the surface, can be induced by the high temperature plume. At high irradiances, significant multiphoton production of electrons can occur through:



where m is the number of photons, A is the atom of interest and A^+ is the corresponding ion, respectively.

As free electrons accelerate in the electric field generated by the laser pulse, collisions with neutral species can thermalise the electrons quickly. A small portion of electrons in the tail of Maxwellian distribution will have enough energy to ionise atoms through:



The process of electron multiplication continues and initiates plasma formation.

Alternatively, free electrons can absorb energy from photons in the three-body collisions with the material, through a process known as inverse bremsstrahlung (IB), to produce other free electrons:



When the density of electrons reaches a critical level, electrical breakdown occurs, in which process insulating neutral gas transforms into plasma. With the creation of shockwaves, the plasma expands and produces emission signals of elements and chemical compounds. During expansion, the continuous emission decreases and characteristic emissions can be identified once the plasma cools and decays as its constituents release their energies in various ways [7,8]. Bremsstrahlung emission (free-free transitions of electrons, when photons are emitted from electron-ion interactions) is responsible for the first stage of intensive continuous emission. Recombination of ions with electrons (free-bound electron transitions) dominates later [8]. After highly excited species with electrons bound in higher energy levels decay to lower energy levels through spontaneous emission, characteristic lines emerge (Figure 1.3). Ions and electrons recombine to generate neutral atoms. In some cases, molecules can be formed (detection of molecules is possible at later stages) [7].

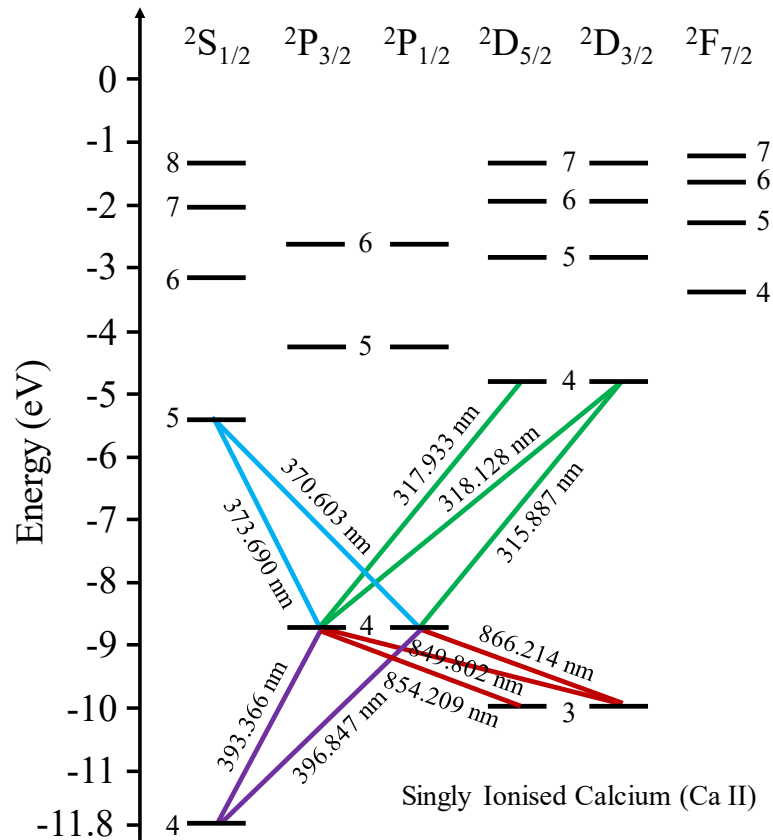


Figure 1.3. Energy diagram (Grotrian) for some of the transitions observed experimentally from singly ionised calcium (Ca II) indicating electron configurations and terms for the states related to the transitions.

The time gap between laser triggering and detector acquisition is critical since LIBS is highly time dependent. Figure 1.4 depicts the emission process graphically. The sample is heated and ablated in the first nanosecond after the irradiation of a laser pulse, resulting in the creation of a plasma. A continuum emission is detected a short time after plasma formation. This "white" light has no atomic information and can cause the detector to become saturated. As the plasma cools, spectral line emissions become more prominent. For LIBS measurements, the detector can be gated in order to block out the continuum signal and collect only the spectral line data of interest. Increasing the gate delay not only decreases the continuum background as well as overall intensity, but it also affects the

types of emission lines being collected. Ionic lines are often stronger at the early stage in the plasma lifetime, while information of molecules is available only at later stages with longer gate delays when cooling plasma leads to the formation of molecules. Therefore, the time-gated measurements need to be optimised with certain delay time and suitable gate width. Typically, a digital delay generator (DDG) with the capability to set gate delay and gate width is used to control the detector.

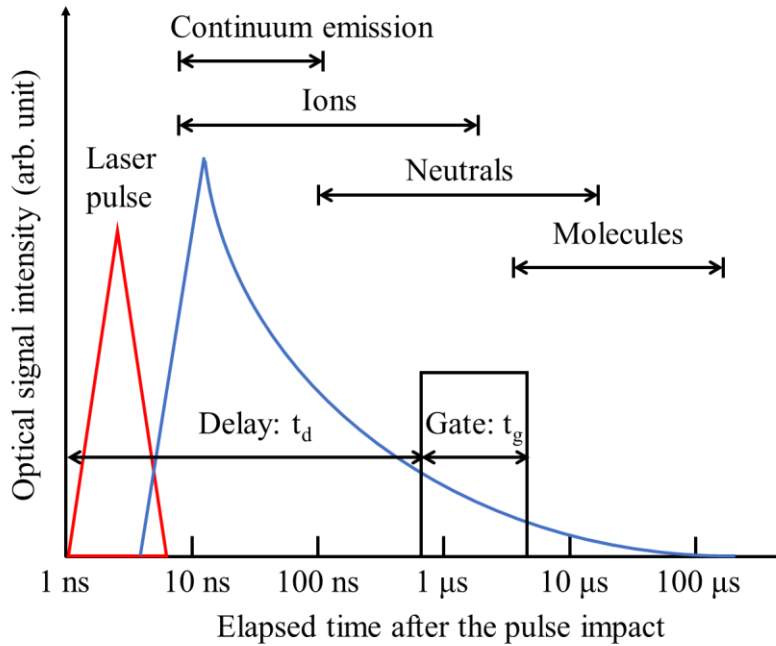


Figure 1.4. schematic overview of the evolution of a typical LIBS event.

LIBS can be used for quantitative analysis. If the laser-induced plasma is assumed to be in a state of local thermodynamic equilibrium (LTE), the spectral line radiant intensity for any atomic transition can be given as a function that involves the number density of the species (represented by the Boltzmann distribution), relevant spectroscopic parameters and the plasma electron temperature:

$$I_{mp} = \frac{hcgA_{mp}}{4\pi\lambda U(T)} N \cdot e^{-\frac{E}{kT}} \quad (1.13)$$

where m and p represent the m^{th} and p^{th} energy level, A_{mp} denotes the probability of the electron transition from the m^{th} to p^{th} energy level (also known as the Einstein coefficient), λ is the line wavelength, $U(T)$ is the partition function (usually the statistical weight of the ground state), g is the degeneracy of the upper energy level, E is the energy level of the upper level, k is the Boltzmann constant, and T is the temperature, respectively.

1.1.3. Laser induced fluorescence (LIF)

Laser induced fluorescence (LIF) is an optical spectroscopic technique in which a sample is excited with a laser and the fluorescence generated by the sample is recorded by a photodetector. LIF is a type of fluorescence spectroscopy. In the case of a laser instrument, this method employs a laser source rather than the traditional lamp for excitation. While lasers are now commonly utilised as excitation sources in photoluminescence spectrometers, LIF was first developed as an independent laser spectroscopy approach. Just like LIBS, LIF was developed shortly after the laser was invented in 1960s. Richard N. Zare published the results of the first LIF experiment in 1968 [9], though the phenomenon of induced fluorescence was first discussed by R. W. Wood in 1905 [10].

Laser-induced fluorescence is the re-emission of absorbed electromagnetic radiation from atoms or molecules that have been excited by laser irradiation. A graphic illustration of this process is shown in Figure 1.5. The absorption of photons excites an atom or molecule to any of the higher vibrational states of an excited state (E_n) [56]. The excited molecule is not stable thus will decay spontaneously. It will move to the lowest vibrational state of the excited state (E_1) by non-radiative processes, and then emit a photon to de-excite the atom or molecule to some vibrational level of the ground state energy level (E_0). Because

the de-excited electron can revert to any of the ground state vibrational level, the fluorescence feature can be broad.

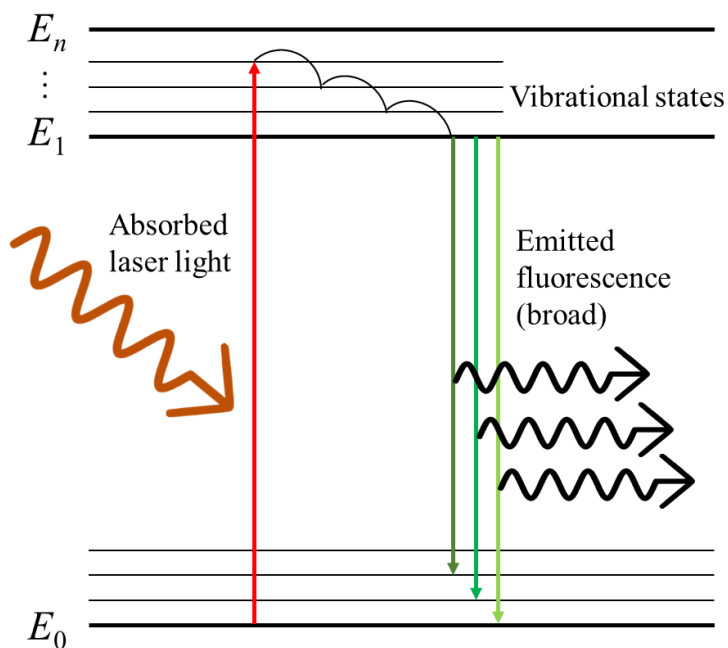


Figure 1.5. Diagram of molecular energy level depicting the process of laser-induced fluorescence.

Compared to absorption spectroscopy, LIF offers various advantages: 1) The fluorescence signal is detected against a dark background, therefore LIF has good detection sensitivity. 2) The detection of the emitted radiation can be at various angles with regard to the incident laser beam as the fluorescence emission occurs in all directions. 3) Spectrally resolved fluorescence can reveal information about transitions of the sample from the excited state to various vibrational states of lower energy levels. 4) It is feasible to analyse the processes of de-excitation and potential changes of the excited molecules due to the time delay between excitation and detection.

Depending on the laser and detection system employed, there are various forms of laser induced fluorescence spectroscopy. This technique can be commonly applied in

excitation or emission LIF spectroscopy. The excitation wavelength is adjusted using a tunable laser in excitation LIF, allowing the vibrational structure of the excited state to be resolved. The molecules fluoresce from the lowest vibrational level of an excited singlet state, returning to a series of vibrational levels in the ground state. Excitation spectra record fluorescent light at a fixed emission wavelength or a range of wavelengths. Between the sample and the photomultiplier tube (PMT) is a bandpass filter that is used to detect all of the emission from the sample while filtering out the scattered laser light. For that reason, an excitation wavelength in the UV region (normally 266 nm) is widely used which does not interfere with the collection of broad emission signals in the UV–vis spectral region (~200–800 nm). In emission LIF, the sample is excited with a fixed pump wavelength. The emission spectrum is then analysed using a monochromator for the selected detection wavelength. Single-point detection with a PMT is commonly adopted, while an array detector (CCD or CMOS) can also be used to collect the entire spectrum in one shot.

Laser-induced fluorescence can alternatively be performed in a continuous-wave or time-resolved manner. Continuous-wave (CW) LIF, which employs a CW laser for excitation, is conducted when only the spectrum is required. As the excitation is continuous, information such as fluorescence lifetime cannot be acquired. On the contrary, a pulsed laser is used to excite the sample in time-resolved LIF, and the sample's emission (either a single wavelength or the entire spectrum) is monitored as a function of time. This gives useful time-resolved information, such as lifetimes and spectral evolution of chemical intermediates. With various time delays, the acquisition of the evolution of the full LIF spectrum can be achieved.

1.2. Challenges of *in situ* cultural heritage research

The study of cultural heritage objects involves questions on their origin, dating, materials, manufacturing techniques, attribution, authenticity, and status of damage and/or degradation. Traditionally, historical documents and archives contribute to the understanding of various aspects of the above questions. Unfortunately, in some cases the background information has been lost. More often, heritage objects have no records at all, which necessitates modern scientific analysis so that the missing information can be re-established from the physical or chemical properties of the works of art. The application of scientific methods in the field of cultural heritage leads to the emergence of an interdisciplinary domain called heritage science.

Scientific investigations of cultural heritage objects are frequently confronted with a variety of analytical difficulties. Identification of materials such as pigments is crucial in the study of murals in caves, tombs, and buildings as they can disclose information about art history, trade, and cultural exchanges, as well as conditions of degradation. Technological developments in the past century give rise to a wide range of analytical methods which can be used for physical and chemical characterisation of the materials and therefore answering the cultural/historical/conservation questions.

It is known that many analytical techniques at their early stages of development were difficult to perform due to technical restrictions and thus only limited to research laboratories for a long time. That is feasible for small-size objects that can be delivered to laboratories. Sample preparation might be required for inconvenient objects. However, for cultural heritage studies, investigations in a non-destructive manner are usually preferred according to conservation ethics. In practice, some objects are immovable (rock art, wall paintings, facades, statues, monuments) or inaccessible for conventional

examination, which requires *in situ* analysis. The availability of new equipment and instrumental innovations in the past few decades have contributed to the transition of many analytical methods from the research laboratory to the real world. Small portable and mobile instruments are now available and fibre optics probe heads for spectroscopy techniques enable investigations from a distance.

Material identification is one of the most important topics in heritage science. Heritage objects are often composed of heterogeneous materials such as pigments, minerals, metals, stones, ceramics, glass, and jewellery. For characterisation of the above materials, physical and chemical analyses can provide information about a sample in various aspects, such as a quantitative characterisation of its constituents or a qualitative assessment of the materials on an elemental or molecular level. Several analytical approaches, particularly spectroscopy-based techniques, are available to extract the desired information (qualitative or quantitative, elemental or molecular). A range of spectroscopy approaches are becoming increasingly prevalent for *in situ* analysis of cultural heritage objects, including fibre optic reflectance spectroscopy (FORS), X-ray fluorescence (XRF), X-ray diffraction (XRD), Raman spectroscopy, Fourier transform infrared spectroscopy (FTIR), LIBS, etc.

However, environmental conditions and technical restrictions present new challenges specific to *in situ* investigation. XRF can only be performed up close, as the fluorescent X-ray can be easily absorbed by air or the sample itself (emissions from light elements even struggle to escape from the sample without being absorbed). Being micro-destructive, LIBS typically samples very small amounts of material (~0.1 µg to 1 mg), which still raises considerable concerns for its safe use in heritage science. Other challenges particular to wall paintings could emerge from the remoteness of the locations, the inaccessible height of the works of art and the problem in controlling the surrounding

environment. Scaffolding is a common practice that gives researchers access to areas of interest, such as upper parts of high walls or ceilings. It has several disadvantages: 1) can be relatively costly; 2) does not conveniently enable researchers to reach the desired position for investigation; 3) may not be steady, which is crucial for sensitive measurements. Hence the introduction of mobile ground-based analytical instruments that can work in a contactless way is highly desirable.

In our research group (Imaging & Sensing for Archaeology, Art History & Conservation Research Centre), remote and standoff instruments have been developed in recent years. A visible/near infrared (VIS-NIR) remote spectral imaging system, PRISMS, is built with the ability to image wall paintings at sub-millimeter resolutions from a distance of tens of meters [11]. However, reflectance spectroscopy alone in some cases is not sufficient to give definitive identification of painting materials (for example, various yellow pigments share similar spectral features). Complementary techniques that can provide other information such as elemental composition or molecular structure are needed. For *in situ* analysis of wall paintings in a UNESCO site, Mogao caves in Dunhuang, China, machine learning (ML) methods were applied to automatically process the spectral imaging data acquired by PRISMS, clustering similar spectra and therefore mapping material distribution. A mobile Raman spectroscopy instrument was mounted on a tripod to investigate the pigments at ground level. The results were used to complement PRISMS data to ascertain the pigment mixture on the ground area and extrapolate the material identification results to the upper level in the same cluster, when there are areas on the ground level clustered with areas at the upper parts. A standoff Raman spectroscopy system, which can reveal molecular structure of painting materials at remote distances (e.g. upper parts of the wall, or the ceiling), is needed to complement PRISMS remote standoff reflectance spectral imaging. In addition, supporting remote and standoff

techniques for elemental characterisation are required in certain cases where reflectance spectroscopy and Raman spectroscopy might not be sufficient thus are unable to give definitive identification. The most common instrument for *in situ* elemental analysis is portable XRF. However, XRF cannot be performed remotely as emitted X-rays can be easily absorbed by air. LIBS is an ideal alternative to XRF with unique advantages. In particular, it can perform rapid analysis with one single laser pulse within one second and is sensitive to all elements.

Sharing similar instrumental configuration, another technique, LIF, can be a useful tool in distinguishing highly fluorescent materials, such as semi-conductor based pigments and aged organic materials. It is non-destructive. Time-resolved analysis can be achieved by using a pulsed laser source and time-gated detectors, which is good for measurements in ambient light conditions for *in situ* analysis.

1.3. Literature review of remote laser spectroscopy techniques

1.3.1. Raman spectroscopy

Though the Raman effect was discovered in 1928, the extensive use of Raman spectroscopy was not forthcoming until the invention of lasers during the 1960s. The application of Raman spectroscopy on works of art was not realised until the emergence of the so-called MOLE (molecular optics laser examiner) Raman microprobe in 1975 [12]. In 1979, the same group used the coupling of a microscope and a Raman spectrometer for applications in a range of fields including archaeology and gemmology, where a spectrum of a Chinese vase was presented [13]. Early studies were also focused on the

biodeterioration of Italian Renaissance frescoes, specifically the oxalates in lichen encrustations, in early 1990s [14,15]. Later in 1995, the molecular state of archaeologically unearthed biomaterials, namely the 5200-year-old skin of Ötzi the Alpine Iceman, has been investigated using Raman spectroscopy [16]. Materials identification using Raman spectroscopy is usually based on the comparison of the Raman signals of the unknown substance with a spectral database of reference materials. Bell et al. published the Raman spectroscopic library of pre-1850 pigments in 1997, which led to the explosive growth of the application of this technique in artworks [17]. As the spot size can be reduced to micron level, the use of microscopic Raman spectroscopy (or Raman microspectroscopy) to interrogate microgram and sub-microgram quantities of material is made possible. It is worth noting that the research focus for pigments later extended to their degradation in artworks [18,19]. Microscopic Raman spectroscopy is commonly considered as non-destructive, provided the laser power is kept relatively low. Raman spectroscopists soon realised that the Raman laser could easily degrade, damage or even burn the sample, which brings about the investigation of the safety of Raman instruments and laser-induced degradation effect on heritage materials [20]. Over the years, microscopic Raman spectroscopy became an established technique of choice for heritage/conservation researchers, because of the small spot size that allows the identification of individual components and minimises the contribution of fluorescence from the large matrix.

As previously stated, advancements in instrumentation are directly responsible for the evolution of Raman spectroscopy. Thanks to the development of laser optics and the miniaturisation of lasers and detectors, the application of Raman spectroscopy in archaeology and cultural heritage has advanced rapidly, which brings the laboratory closer to the objects of interest. The introduction of fibre optics into the field of Raman

spectroscopy [21], paved the way for the advent of mobile Raman instrumentation for *in situ* analysis of heritage objects (in museums or in the field) [22]. Soon, mobile Raman systems equipped with a compact detector and an optical fibre probe became commercially available. In recent years, due to its convenient use in fieldwork, mobile Raman spectroscopy has been extensively applied in the *in situ* studies of a variety of archaeological or heritage scenarios, e.g. museum items and outdoor objects such as rock arts and newly excavated archaeological materials. The analysed materials include illuminated manuscripts, paintings, minerals, gems, stones, rocks, pottery, porcelain, glass, enamel, and etc [23,24].

In atmospheric scattering investigations during the 1960s, the idea of conducting Raman measurements remotely arose [25,26]. Long optical fibres enabled the remote detection of samples at distances of several metres to dozens of metres [27]. However, this kind of remote Raman instruments means that only the operators are kept away while the probe is still required to be in close contact with the sample. It is not a good solution for objects at heights and it requires moving of the probe to another positions for another measurement. The combination of telescopes with Raman spectrometers leads to remote/standoff Raman spectroscopy *sensu stricto*, which can work in the range of several metres all the way up to over 1 kilometre [28–31]. This newly emerged technique is best suited to investigations where targets are inaccessible or too dangerous. Explosives detection is one of such applications, where small quantities (a few milligrams) of explosives, e.g. tri-amino tri-nitrobenzene (TATB) and octogen (HMX), can be identified at a standoff distance [32–34]. The most well-known field where remote Raman spectroscopy is adopted is planetary exploration. The remote standoff Raman systems is more convenient to probe a large area without moving the system. International collaboration has been established over the years for the development and test of such a

remote instrument on earth [35,36]. It was not used in real space environment until NASA's Mars 2020 mission. The Perseverance Rover is equipped with SuperCam, a suite of remote-sensing instruments including a remote Raman spectrometer at 532 nm that can investigate targets up to 12 m from the rover [37]. Remote standoff Raman spectroscopy also demonstrates great potentials in plant stress response research [38].

Unfortunately, before our work, there is no remote/standoff Raman system that are dedicated to cultural heritage research, though the advantages and the demand for such technique in *in situ* heritage applications are becoming increasingly prominent. The ambiguous use of the term 'remote' in heritage science is confusing as it is often achieved with remote probe and optic fibres. For instance, a paper reported the non-contact remote Raman scanning but the claimed working distance can be merely 20 cm [39]. A clear definition of 'remote' in terms of working distances is lacking. The application of telescope-based Raman spectroscopy most closely related to cultural heritage is a series of studies on stones/rocks/minerals by Sharma et al [40–42], though the purposes were mainly for planetary sciences. Most remote/standoff Raman systems use high-power pulsed laser sources with large telescopes [35]. The working distance is usually dozens or hundreds of metres, which is more suitable for outdoor investigations but not for indoor works with space limits. The spot size can be a few centimetres, resulting in poor spatial resolution not suitable for analysis of artworks. A truly remote/standoff Raman system for cultural heritage applications is much needed. It is of crucial importance that unique requirements for heritage objects, such as low laser intensity (to avoid laser-induced damage) and high spatial resolution, must be taken into consideration.

1.3.2. LIBS

The past two decades has witnessed substantial growth of LIBS applications in archaeology and cultural heritage research [43–45]. Offering preferable performance, benchtop LIBS systems are often employed for quantitative analysis of elemental compositions in heritage objects. Lazic et al. demonstrated different approaches for quantitative LIBS analysis with applications of archaeological materials including bronzes, marbles and ceramics [46].

LIBS offers unique advantages, such as being able to detect light elements and could reveal elemental information beyond sample surface when applying repeatedly laser pulses on the same spot and analysing the generated plasma emission, which makes LIBS a very efficient option for *in situ* elemental analysis, especially for depth profiles and for the simultaneous detection of a wide range of elements. Compared to Raman spectroscopy instrumentation, typical LIBS setups are relatively simple. It usually comprises of a pulsed laser source for generating plasma from the target, an optical fibre to collect the light emission, and a spectrometer that records the spectrum. Since the plasma emission occurs later than the laser pulse, a signal generator is normally used to synchronise the laser trigger and the collection of the spectrum. Nowadays it is usually integrated into the laser source or the spectrometer for LIBS applications. The technological advances, especially the miniaturisation of components, make mobile LIBS systems possible. Portable instruments, such as man-portable and handheld instruments, are now commercially available. The development of portable LIBS instruments was reviewed in detail and compared with XRF [47]. *In situ* LIBS analysis are mostly performed with mobile instruments. Mobile LIBS systems have been successfully employed for *in situ* analysis in various applications [48,49].

The LIBS analysis of distant objects from several meters to dozens of metres from the instruments can be achieved using both field-deployable mobile instrumentation and telescopes for long-distance delivery of the laser radiation and collection of the emission light. Just like remote Raman spectroscopy, remote LIBS has found applications in areas including explosives detection and space exploration.

The U.S. Army Research Laboratory utilised standoff LIBS spectra acquired at 20 m to discriminate between explosives and non-explosives [50]. Multivariate statistical analysis such as partial least squares discriminant analysis (PLS-DA) has been introduced for explosives detection [51]. Laserna et al. reported on rapid detection and classification of different kinds of explosives at standoff distances up to 45 m using LIBS [52,53].

The first demonstration of remote LIBS technique applied in space science was the ChemCam remote sensing suite on board the Curiosity rover, which landed on Mars in 2012. The LIBS instrument on ChemCam can target a rock or soil sample over a 1.5–7 m range, utilising pulses from a 1067 nm Nd:KGW laser with >30 mJ pulse energy, and then observing a spectrum between 240 nm and 800 nm [54]. The next generation remote sensing module, SuperCam, on board the Perseverance rover has successfully performed quantitative remote LIBS analysis on Mars [55].

For industrial applications, Anglos et al. demonstrated the *in situ* examination of types and ageing conditions of composite polymeric insulators in overhead high voltage electricity pylons by a remote LIBS system [56]. Lang et al. performed standoff LIBS depth profiles in an argon environment for Sr and Cs contaminated nuclear plant steel with different laser pulse energy [57].

For cultural heritage applications, remote LIBS provides long-range elemental analysis capability which XRF could not offer. However, the adoption of this micro-destructive

technique is always treated with caution. The concern is not only for the safety of the objects, but also for the health and safety of people as long-range open-path laser pulses could pose a threat to anyone nearby. There are not many archaeological or cultural heritage studies involving remote or standoff LIBS. Several remote or standoff LIBS systems have been developed for *in situ* characterisation of stones and metals. Grönlund et al. demonstrated a mobile lidar system mounted on a truck, where remote LIBS analysis of several metal and mineral samples were successfully carried out at a distance of 60 m [58]. With rich experience in developing remote LIBS technique for explosives detection, Laserna's research group at the University of Malaga deployed a remote mobile LIBS system for the analysis of the façade of the Cathedral of Málaga (Spain) at 35 m [59]. Lazic et al. proposed a laboratory prototype LIBS system with oblique design that could work from 8–30 m, for analysis of multi-layered ceramic materials [60].

The ability to virtually analyse any kind of substance (solid, liquid, gaseous) in various environments, including air, vacuum, fluids, and even under harsh conditions such as high temperature, high pressure, and toxic environments contributes to the widespread use of LIBS. It soon draws attention of underwater archaeologists, since a large number of archaeological artifacts are discovered submerged in maritime environments, which demands a unique technique for elemental analysis in their research. Recently, Laserna et al. has contributed a lot to this field, with several publications presenting fibre-optics based and telescope based standoff remote submarine LIBS analysis [61–63]. In standoff mode, samples can be analysed at distances up to 80 cm from the instrument at the solid–water interface.

As mentioned earlier, one of the unique applications of LIBS is precisely being micro-destructive. When delivering repetitive laser pulses on the same spot, depth profiles of a wide range of elements can be obtained. This kind of work is mostly done with benchtop

LIBS systems. Recently, some studies demonstrated the potential of remote *in situ* depth-profiling analysis. For archaeological and cultural heritage research, depth-resolved LIBS analyses have been carried out both at close ranges [64,65] and in a remote/standoff manner. When surveying the Cathedral of Málaga, Laserna et al. traced the depth profile of a Cu line at 406.3 nm from 500 laser pulses delivered to a metallic seal [59]. Depth profiles of a range of elements (Al, Ti, Si, Fe, Ba, Mn, Pb) from 500 laser pulses on ‘clean’ and ‘crust-coated’ sections within the Solomonic column were presented as well. However, they had limited success because of the wandering beam caused by the wind.

Two papers mentioned earlier on close-range depth-profiling LIBS also utilised complementary techniques (XRF and OCT, respectively) which provided additional information corresponding to each layer [64,65]. Remote Raman spectroscopy seems to be an ideal choice, as the instrumentation shares similar designs. Detalle et al. proposed an experiment where LIBS is used to ablate the surface of wall painting pigments, and then Raman spectroscopy reveals the molecular information underneath [66]. When performed repeatedly, this enables a layer-by-layer analysis using LIBS and Raman spectroscopy. This idea can be practiced remotely. The SuperCam on Perseverance rover has the potential for such application but so far depth profiles has been conducted by LIBS aided by acoustic monitoring [67]. Raman spectroscopy was only used to acquire mineral information in the LIBS crater. In addition, the integrated use of LIBS and SWIR reflectance spectroscopy for depth profiles was proposed in China's first Mars exploration [68].

1.3.3. LIF

LIF applications in cultural heritage and archaeology has been critically reviewed by Nevin et al, summarising studies in a variety of materials including stones, minerals, pigments, varnishes, and binding media [69]. As a versatile, non-destructive analytical technique, LIF has great potential as a tool of painted artwork diagnostics. Semiconductor pigments can yield characteristic fluorescence features under excitation due to the small band gap, which is responsible for the relatively narrow emissions. Miyoshi et al. reported the LIF analysis of 40 pigment samples using a pulsed N₂ laser ($\lambda = 337.1$ nm) for excitation, and found that several pigments are highly fluorescent, e.g. zinc white (ZnO) and cadmium-based pigments [70]. Anglos et al. demonstrated an LIF application in pigment analysis, focusing on the differentiation of a range of cadmium-based pigments by their fluorescence emission using three laser wavelengths at 248, 355, and 532 nm, respectively [71]. It was found that fluorescence emission increases in the wavelength with higher concentration of Se. LIF was utilised by Pantani et al. for the study of stone monuments in the aspects of biodeteriogen monitoring (green algae and cyanobacteria on the marble substrate), stone fluorescence signatures, and surface treatments [72,73]. Spizzichino et al. reported the application of LIF for the characterisation of treatments with ancient and modern materials on the surface of marble artworks, with methods of rapid identification and mapping developed and tested using discriminant fluorescence features [74]. Lazic et al. presented LIF signals from the glaze and lustre of different colours and discussed the surface plasmon resonance (SPR) peaks of copper and silver nanoparticles which might be responsible for the optical properties and colours of Renaissance Italian lustre pottery [75].

Wall paintings are ideal objects of study for mobile LIF instruments. Fantoni et al. demonstrated a mobile LIF system which is capable of large-area scanning of cultural

heritage surfaces. Reference materials of binders and pigments were tested in the laboratory before the field campaign conducted on medieval frescoes by Giusto de' Menabuoi in the Padua Baptistery [76]. Capobianco et al. reported a case study of Vincenzo Pasqualoni's wall paintings in S. Nicola in Carcere (Rome) [77]. Time-gated LIF helped identify the sporadic use of egg binder and detect of synthetic compounds and ZnO in different part of the fresco, used in past restoration treatments.

Sharing almost identical instrumentation design, remote LIF is often achieved along with remote LIBS technique. The combined use will be discussed in the next section. It is noteworthy that remote and standoff LIF has found extensive applications in biochemistry. Chappelle et al. published several papers on remote LIF applications of green plants, which thoroughly discussed the use of remote LIF technique in plant stress detection, species differentiation, nutrient deficiencies detection, and photosynthesis rate estimation [78–81]. For cultural heritage, this might be related to potential applications of remote LIF in biodeterioration studies.

Grönlund et al. published a series of papers during the 2000s [82], demonstrating a mobile lidar system mounted on a truck that could perform remote LIBS and LIF analysis in heritage sites. The system was firstly tested with remote measurement campaign on six brick samples using five different excitation wavelengths in a laboratory setting [83]. *In situ* LIF analysis was conducted on an ornamental urn on the roof of the main building at Övedskloster castle, presenting distinct emission features at different areas [84]. LIF mapping was performed on the main façade of the Övedskloster castle at ~40 m distance, showing the distribution of chlorophyll, which has strong fluorescence characteristics at ~690 nm [58]. The same mobile lidar system was successfully deployed in a joint Italian-Swedish field campaign at the Colosseum in Rome. Determination of different types of biodeteriogens and chlorophyll content assessment on several areas were achieved.

Monitoring of soiling was illustrated by thematic mapping to reveal the cleaning effect of a contaminated area by fluorescence imaging [85]. Discrimination of masonry materials, reinforcement structures, and protective coatings applied in previous conservation interventions by their fluorescence signatures were implemented [86].

1.3.4. Multimodal analysis

Multimodal analysis using various analytical methods with separate instruments is common for archaeology and cultural heritage studies. Having discussed the principles and instrumentation of the three laser spectroscopy techniques, namely Raman spectroscopy, LIBS and LIF, we have demonstrated that the integration of two or three techniques are feasible. It enables different analyses to be performed on the same spot. In addition, the combination could provide complementary information using a versatile compact setup, which is important for mobile instruments that are suitable for *in situ* analysis. There are numerous research papers on combined instrumentation but most of them presented two laser spectroscopies: LIBS-Raman, LIBS-LIF, or Raman-LIF. The integrated systems are mostly benchtop setups for laboratory use. Mobile or remote instruments are rather few.

LIBS-Raman hybrid:

Laserna et al. published a series of papers on the development of combined standoff Raman and LIBS systems for explosives detection [87–89]. Though one of their LIBS systems was employed for the investigation of the façade of the Cathedral of Málaga, it seems that remote Raman spectroscopy was not used in this field campaign. The SuperCam remote sensing suite on Perseverance rover is equipped with a compact integrated system capable of performing standoff LIBS and Raman analysis [37].

Sharma and co-workers at the University of Hawaii are one of the most active groups in this field that designed a series of combined remote Raman and LIBS instruments for planetary sciences, ranging from compact-sized instruments as modules on space rovers and large mobile systems mounted on trollies with the ability to detect minerals from distances of hundreds of metres [90–93]. The optical setups share a single pulsed laser as excitation source for both LIBS and Raman, while telescopes and spectrometers could be separate for the two techniques or a single collection system can be used. The problem of using a single spectrometer for LIBS and Raman lies in the required spectral range for both techniques. Raman spectra usually covers a wavelength range of ~200–300 nm starting from the Rayleigh line, while typical LIBS signals span 200–850 nm, much broader than Raman spectra. It is a trade-off between spectral range and spectral resolution when using a single grating. There are other issues such as spectral sensitivity (sensor response) at different wavelength regions. To overcome such issues, Echelle spectrograph with the ability to cover broad wavelength range with good spectral resolution is used for combined LIBS-Raman systems [94,95]. Recently a two-component approach was proposed to focus the laser beam and significantly improve remote Raman and LIBS capabilities for chemical detection using remote controlled car or unmanned aerial vehicle (UAV) carrying a small remote lens near the target [93].

LIBS-LIF hybrid:

Anglos et al. [96] reported a simultaneous application of LIBS and LIF using a single optical setup on a model sample comprising of a cadmium yellow ($\text{CdS}\cdot\text{ZnS}\cdot\text{BaSO}_4$) paint layer on top of a white paint made of gypsum ($\text{CaSO}_4\cdot 2\text{H}_2\text{O}$) containing small amounts of zinc white (ZnO). The work was a demonstration of the LIBS technique with abilities of conducting depth profiles and elemental analysis, which is then complemented by the time-integrated LIF analysis of the sample. Both techniques shared the same

excitation wavelength at 355 nm. High energy pulses were used for LIBS, while pulses with energy below the ablation threshold followed for LIF analysis. Pouli et al. investigated the depth profile of protective coatings on historic metal objects using LIBS, which was aided by LIF with lower laser pulse energy (below the ablation threshold) at the same wavelength (at 193 nm for excitation) and geometry [97]. During the depth profiling, in between each LIBS measurement, the pulse energy was attenuated so that the time-integrated LIF spectrum was collected after irradiation of the sample with 100 probe pulses.

As stated above, a research group at Lund University developed a mobile lidar system mounted on a truck with the ability to record remote LIBS and LIF spectra at 60 m. The system was successfully deployed in field campaigns in heritage sites both in Sweden (Övedskloster castle) and Italy (the well-known Colosseum). Details of their LIF analyses are described in the previous section. However, it seems that LIBS analysis was only performed on several metal samples in tests conducted on the university campus but not at heritage sites [98].

Raman-LIF hybrid:

In recent years, the Raman-LIF hybrid draws attention of planetary scientists due to the extensive use of LIF in biochemistry. Combining Raman spectroscopy with LIF for the analysis on the same target could enhance the confidence of a potential biosignature detection.

Sharma et al. proposed a combined inelastic (Raman) and elastic (Mie-Rayleigh) scattering and LIF active remote sensing (RLIF) system for Mars Science Laboratory (MSL) mission [99]. In laboratory tests, Raman spectra of a collection of minerals, organic and molecular gases could be acquired at 100 m at any time of day or night. LIF

spectra of biogenic materials and minerals could complement the Raman data. Sharma et al. also modified a remote Raman spectroscopy system in oblique geometry for composite Raman and LIF measurements of minerals at 10 m [100]. Raman spectra of cyclohexane, ice and gypsum, as well as fluorescence spectra of chlorophyll-a and ruby were presented respectively. The combined LIF and Raman spectra of chalk (CaCO_3) indicated a photo-quenching effect with increased time, as well as a corresponding signal-to-noise ratio (SNR) enhancement for Raman.

LIBS-Raman-LIF hybrid:

Several research groups are working on the development of a single apparatus that combines Raman, LIBS, and LIF, and to address the corresponding instrumental issues of selecting laser sources, collection optics, and experimental configurations that provide the optimum compromise for the three techniques.

Osticioli et al. proposed a compact and potentially transportable prototype instrument capable of performing Raman, LIBS and LIF using a single pulsed laser source for the analysis of cultural heritage objects [101]. A pulsed laser at the second harmonic (532 nm) was used for both Raman and LIBS. Frequency doubling was achieved with a potassium titanyl phosphate (KTP) crystal so that the fourth harmonic at 266 nm was used for LIF. A time-gated intensified CCD (ICCD) detector sensitive at 180–900 nm allowed for the collection of LIBS spectra and can also be employed for both LIF and time-resolved Raman spectroscopy. Natural and synthetic ultramarine pigments were analysed with LIBS and Raman. Raman provided molecular confirmation of both materials as ultramarine, while elemental differences were clearly revealed by LIBS. For organic materials, LIF successfully distinguished egg white from rabbit skin glue, while LIBS showed lines of CN and Ca for both.

Similarly, Martínez-Hernández et al. developed a compact laboratory hybrid Raman, LIF and LIBS system using a single Q-switched Nd:YAG laser at its second (532 nm), third (355 nm) and fourth (266 nm) harmonics and a spectrograph coupled to a time-gated ICCD detector [102]. It is noteworthy that the spectrograph utilised two interchangeable diffraction gratings and entrance slit widths, respectively, providing varying spectral range and resolution for different techniques. Raman and LIF spectra of a range of heritage stone samples excited at 355 nm and 532 nm were compared, while irradiation at 355 nm was used for LIBS. Several model wall painting samples were analysed with all three methods, presenting complementary information for material identification.

A research group at the Centre de recherche et de restauration des musées de France (C2RMF) reported the development of a single LIBS-LIF-Raman hybrid system for cultural heritage analysis [103,104]. Nd:YAG lasers working with 4 different wavelengths of 1064, 532, 355 and 266 nm were employed. Several detection systems such as Czerny-Turner spectrometer coupled with ICCD detector, Echelle spectrometer, and small commercial spectrometer were utilised to collect different signals. This benchtop setup later evolved into a single multi-spectroscopic mobile device for *in situ* analysis of cultural heritage [105].

Chapter 2

Instrumentation

2.1. Remote standoff Raman spectroscopy

2.1.1. Introduction

The identification of painting materials is crucial to the study of wall paintings in caves, tombs, and historical buildings as it can provide related information regarding art history, historical trade and cultural exchanges. However, it can be difficult to perform *in situ* close contact measurements. The remoteness of the locations, the paintings' unattainable height, and the difficulty in controlling the environment they are in are some of the difficulties unique to wall paintings studies. Scaffolding is typically required for the investigation of the upper parts of a wall or ceiling. It can be expensive, difficult to deploy, and, most importantly for scientific analysis, unstable for sensitive measurements where a long acquisition time is needed [106].

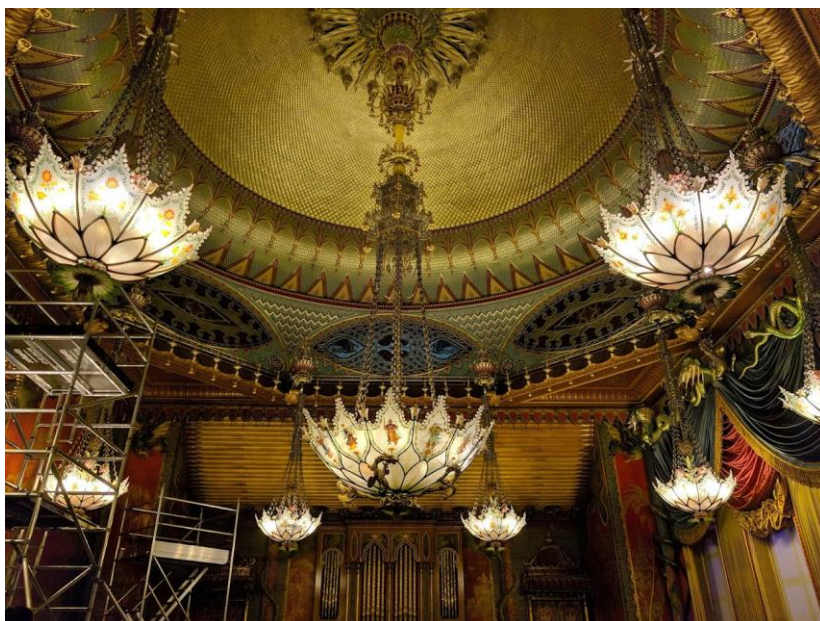


Figure 2.1. Scaffolds for the examination of wall paintings in the Royal Pavilion, Brighton.

In NTU ISAAC lab, our solution is an in-house developed VIS-NIR remote spectral imaging system, PRISMS, which can image wall paintings at sub-millimeter resolutions from a distance of 3–30 m [11]. However, spectral reflectance information acquired by PRISMS alone is not able to differentiate pigments in certain cases (e.g. some yellow pigments share similar reflectance patterns). To address this issue, we need to adopt other analytical methods to complement spectral imaging. Remote standoff Raman spectroscopy seems a good choice.

Raman spectroscopy is a powerful analytical technique which precisely identifies materials by their fingerprints in molecular vibrations. The emergence of lasers in 1960s and the technological advances in sensitive detectors since the 1980s enable Raman spectroscopy to become a useful tool in many application fields. In cultural heritage research, it has been utilised for non-invasive material identification (such as pigments), investigations of degradation products, provenance determination, etc. [107–111].

There are controversies in the community of remote sensing and cultural heritage with regard to the accurate use of the term ‘remote’. To avoid any confusion, here we define remote standoff Raman systems as instruments that can work at a distance of 3–50 m between the instrument and the object. The idea of performing Raman measurements remotely was first reported during the 1960s [25,26]. Nowadays, the majority of remote and standoff Raman systems have been developed for planetary sciences and explosive detection, mostly using high-power pulsed lasers for excitation [35]. However, the Raman efficiency and potential laser induced damage should be considered when designing Raman instruments for cultural heritage research. Both aspects need to be balanced to achieve material identification in acceptable acquisition time while ensuring the safety of heritage objects.

2.1.2. Original experimental setup

The design of a remote standoff Raman spectroscopy for wall paintings should take the following requirements into consideration: 1) for sensitivity, it should be able to detect and identify the majority of common historic artist pigments at a distance of 3–15 m (suitable for most indoor investigations) with an comparable spectral resolution to commercial mobile Raman system ($\sim 8 \text{ cm}^{-1}$) in 30 min; 2) The intensity and fluence (accumulated in typical time required for detection) of the excitation laser should be safe for all pigments; 3) it should be mobile to enable *in situ* measurements; 4) it should be able to operate in normal indoor light conditions (with daylight from windows) as it is not always feasible to perform Raman measurements at night; 5) a co-axial geometry of the laser beam and the collection optics is preferred for the alignment of the excitation and collection beams to be independent of distance; 6) the size of the laser spot on target should be $< 10 \text{ mm}$ in diameter at a distance of 10 m to achieve an acceptable spatial resolution; 7) Positions of the measured spot should be recorded online.

Figure 2.2 shows the original design of a remote standoff Raman spectroscopy system for working at distances of 3–15 m. The instrument consists of a CW laser source (Newport TLB-7113-01) for excitation at 780 nm with a maximum output power of 90 mW, a Maksutov-Cassegrain reflector telescope (Meade ETX-90) with 90 mm clear aperture and 1250 mm focal length, and a Czerny-Turner spectrograph (Andor Shamrock SR-193i) coupled with a high sensitivity CCD detector (Andor iDus 416), which is thermoelectrically cooled to -75°C for normal Raman measurements. Two mirrors positioned at a 45° angle reflect the laser beam, making it coaxial with the telescope. The output laser beam is collimated, with a tiny divergence that leads to a spot size of $\sim 4 \text{ mm}$ at 3 m and $\sim 8 \text{ mm}$ at 8 m. A narrowband laser clean-up filter centred at 780 nm with a FWHM bandwidth of $\sim 3 \text{ nm}$ is used to eliminate optical noise from unwanted laser

background, non-lasing (plasma) lines and spontaneous emission. The telescope collects the reflected light, which passes through a 780 nm longpass filter with a sharp cut-off to block the Rayleigh scattered line and into a collection fibre (Thorlabs M75L02) with a core size of 200 μm in diameter. A PC-controlled motor adjusts the primary mirror of the telescope for focusing. A dichroic beamsplitter at 770 nm is directly coupled to the rear port of the telescope to send the reflected light <770 nm to a guiding camera for imaging, which can be used to evaluate the focusing of the telescope and inspect the measured area. A pair of plano-convex lenses are employed to better couple the received signals >780 nm into the fibre. The received signals then pass through an entrance slit of 50 μm into the spectrograph. The entire system is mounted on rails atop an altitude-azimuth telescope stage, which is controlled by a hand controller (Meade Autostar). The cut-off wavenumber, dictated by the dichroic beamsplitter and the longpass filter, is ~ 130 cm^{-1} . The spectral resolution is ~ 4 cm^{-1} over a spectral range of 140–1300 cm^{-1} when recorded with a 1200 l/mm grating, or ~ 8.5 cm^{-1} over 140–3300 cm^{-1} using a 500 l/mm grating.¹

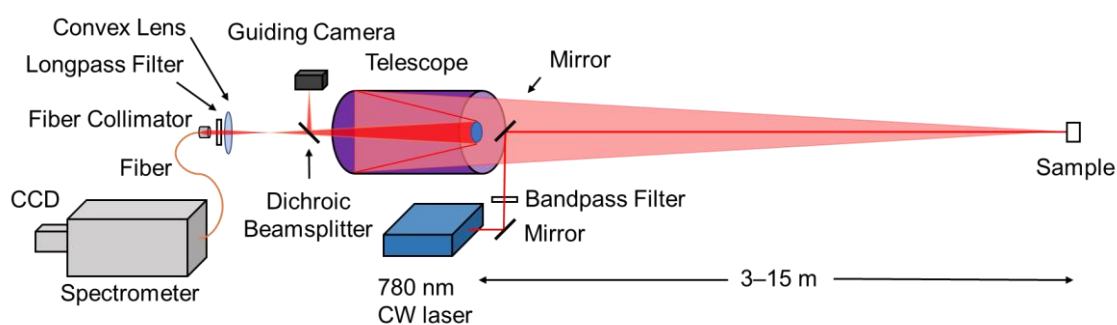


Figure 2.2. Schematic of the original remote standoff Raman system employing a CW laser at 780 nm co-axial with the collection optics. Adapted with permission from [112] © Optica Publishing Group.

¹ The spectral resolution, as reported in one of our papers [112], of ~ 15 cm^{-1} with a 500 l/mm grating and ~ 9 cm^{-1} with a 1200 l/mm grating for the entire spectral spectrum, resulted from an issue of the grating turret that made the gratings tilted. It was fixed and the spectral resolution improved consequently.

2.1.3. Sources of noise

Noise is an important issue to all spectroscopy techniques. It is crucial to understand the sources of different types of noises in order to optimise the collection of Raman signals thus improve the signal-to-noise ratio (SNR).

In the case of photon detection, there is an inherent statistical variation in the arrival rate of incoming photons incident on the detector (CCD in our case) called shot noise (or photon noise in optics). It is a quantum noise effect related to the discreteness of the energy in the electromagnetic field of photons.

The counts of electric signals N converted from photons incident on the detector can be given by:

$$N = P \cdot \eta \cdot t \quad (2.1)$$

where P is the photon flux (photons/pixel/second), η is the quantum efficiency (QE) of the device, and t is the integration time (seconds).

Shot noise obeys the Poisson distribution, so that it is equal to the square root of the average counts of events N :

$$\sigma_s = \sqrt{N} = \sqrt{P \cdot \eta \cdot t} \quad (2.2)$$

It is noteworthy that in Raman measurements the total shot noise is related to all the signals recorded, including Raman signals of the material of interest, Raman signals of other components in the sample (matrix), fluorescence generated by laser irradiation and then collected by the detector, stray light and cosmic rays entering in the detector, etc. Some of the irrelevant signals can be removed by data processing, such as the subtraction of the broad fluorescence signals or the subtraction of the background spectrum to correct for ambient light contributions. However, shot noise generated by these components cannot be eliminated.

There are sources of noises from the detectors. The dark noise comes from the statistical variation in the number of charges thermally generated in the silicon structure of the CCD. Silicon at temperature above zero kelvin can eject valence electrons into the conduction band in response to internal temperature, even in the absence of photons. The resulting small electric current that flows through the CCD at a given temperature is referred to as dark current. The dark noise follows a Poisson relationship to dark current as square root of the amount of thermal electrons generated within the integration time:

$$\sigma_d = \sqrt{I_D \cdot t} \quad (2.3)$$

Dark noise is highly dependent on device temperature, thus can be reduced by cooling the detector. Technical advances in CCD allow modern high-performance devices to be deep cooled to a temperature at which dark current is reduced to negligible levels over a typical integration time.

The contribution of dark noise is the main reason why normal spectrometers that are thermoelectrically cooled to -25°C are unable to perform long-time Raman analysis lasting >5 min for materials with low Raman scattering cross-section. The accumulation of dark noise can be significantly greater than weak Raman signals of interest. Therefore, a high-performance deep-cooled detector is necessary for Raman measurements.

Another source of noise from the detectors is the readout noise, which is a combination of noises inherent to the readout process of amplifying and converting the photoelectrons into a change in analogue voltage signal for quantification, as well as the subsequent analogue-to-digital (A/D) conversion. The main source of readout noise is the on-chip amplifier. For the same device, readout noise increases with read-out rate or frame rate, as the speed of charge transfer (current) can affect the temperature of the devices. Improvements in CCD design enable high-performance detectors to significantly reduce the level of readout noise. Readout noise is directly related to the numbers of readouts.

For Raman measurements, the accumulation or average mode should be used with caution to minimise the contribution of multiple readouts.

The total noise is the quadrature sum of different types of noise sources discussed above, therefore the SNR can be calculated as:

$$SNR = \frac{N}{\sigma_{total}} = \frac{N}{\sqrt{\sigma_s^2 + \sigma_d^2 + \sigma_r^2}} = \frac{P \cdot \eta \cdot t}{\sqrt{P \cdot \eta \cdot t + I_D \cdot t + \sigma_r^2}} \quad (2.4)$$

In Raman analysis, if the dark current is stronger than Raman signals, the dark current will dominate over other noise components (dark noise limited). If the dark current is minimal and Raman signals are stronger, the detection is photon noise limited so that $SNR \sim \sqrt{P \cdot \eta \cdot t}$. If both the dark current and Raman signals are weak, then at short integration time t , the noise could be dominated by readout. Photon noise can eventually take over with increasing integration time t .

In addition, long time laser irradiation could increase the risks of potential laser induced degradation. Therefore, the integration time needs to be carefully determined for each sample. A deep cooled detector operating in modes with minimum readouts, is preferred for Raman measurements.

2.1.4. Choice of excitation wavelength

A CW laser at 780 nm was chosen for the remote standoff Raman system with several factors taken into consideration, including the Raman detection efficiency, overall reduction in fluorescence in most materials of interest, the cost of optical components and detectors for the corresponding wavelength range and the laser induced damage threshold for various materials.

The Raman scattering strength is proportional to the incident light intensity and inversely proportional to the wavelength to the fourth power. Consequently, a shorter excitation wavelength can yield a stronger Raman signal from a given sample.

Fluorescence is often the practical limitation to the effective use of Raman spectroscopy. When illuminated by a laser, many materials can generate strong photoluminescence to overwhelm the Raman signal, since photoluminescence has a much higher probability of occurring than does Raman scattering. One may argue that the background subtraction of the photoluminescent background would be sufficient to reveal the Raman spectrum from the superimposed Raman and photoluminescent signals. In this case, the shot noise can be separated into contributions of Raman signals of interest and the fluorescence. If the photoluminescence is so strong that its signal is much greater than Raman signal, in which case the signal noise will also dominate over instrument noise, the SNR for Raman detection given by:

$$SNR \sim \frac{N}{\sigma_s} \sim \frac{N_{Raman}}{\sqrt{\sigma_{s_fluorescence}^2}} = \frac{P_{Raman}}{\sqrt{P_{fluorescence}}} \cdot \sqrt{\eta \cdot t} \quad (2.5)$$

will be rather small, and therefore, it can be difficult to distinguish the Raman signal from the shot noise due to fluorescence.

Fluorescence typically occurs in the ultraviolet-visible (UV/VIS) region at wavelengths above ~300 nm, independent of excitation wavelength. To avoid that, excitation wavelength for Raman spectroscopy in the near-infrared (NIR) region, such as 785 nm or 1064 nm where fluorescence is weaker has an advantage. However, Raman efficiency is much lower in the NIR and at the longer wavelength of 1064 nm, normal Si based CCD does not have much response and the more expensive InGaAs or MCT (mercury-cadmium-telluride) detectors that also need deep cooling to reduce the noise are required.

Excitation wavelength in the UV region, such as 266 nm (quadrupled, diode-pumped Nd:YAG lasers) and 248.6 nm (NeCu hollow-cathode metal-ion lasers) can also have an advantage, since a typical Raman spectrum with 4000 cm^{-1} wavenumber range would not reach 300 nm and the Raman efficiency is much higher owing to the much shorter wavelength. On the other hand, the narrow spectral range in terms of wavelength at UV region requires a high spectral resolution (e.g. a 4 cm^{-1} difference in wavenumber equals $\sim 0.03\text{ nm}$ in wavelength for 266 nm excitation, compared to $\sim 0.25\text{ nm}$ for 785 nm excitation), therefore excitation lasers with narrower linewidth, filters with steeper cut-off edge, and high-resolution gratings are needed. In addition, UV-enhanced CCD cameras are required for acceptable response. All the above optical components for UV region are technically demanding, thus more expensive. Another challenge with UV illumination is that the higher energy of UV photons can be more destructive to the sample. For the above reasons, UV Raman is so far not widely used in the heritage field.

All things considered, 785 nm seems a balanced choice which offers sufficient Raman scattering strength, has cheaply available optical components and good detector response, and suppresses intense fluorescence.

2.1.5. Raman efficiency comparison between CW and pulsed laser

Most remote Raman systems employ pulsed lasers for excitation, as high peak power laser pulses allow for gated collection of Raman signals, which also minimises the collection of daylight during the Raman measurements. Such remote systems are mostly adopted in fields such as planetary sciences (e.g. remote detection of rocks and minerals on planets), and explosives detection (e.g. identification of trace amounts of explosives and their residues from standoff distances) [113,114]. For these kinds of work, laser

induced degradation effects are not the main concern of the studies as long as the materials are not completely altered to lose their original spectral features.

Higher laser intensity leads to higher Raman efficiency (since Raman intensity is proportional to laser intensity) and also greater risks of laser induced degradation when the laser intensity exceeds the damage threshold of the material. For practical Raman analysis, this is a trade-off that needs to be carefully considered, especially in the field of cultural heritage research where the conservation of heritage objects is of paramount importance. For pulsed lasers and CW lasers, the damage threshold in intensity may differ as the corresponding degradation mechanisms can be different due to thermal effects, e.g. heat dissipation between pulses may result in a higher damage threshold for pulsed lasers than for CW lasers.

Here we will discuss the Raman efficiency between CW and pulsed lasers at the same wavelength. The calculations are based on assumptions that damage threshold for CW and pulsed lasers are equal. Raman intensity S_{CW} is proportional to laser intensity, the irradiated area (assume that the laser spot A_L equals the detected area A_D so that all Raman signals can be detected), and the measurement time t_{CW} . For a CW laser:

$$S_{CW} \propto I_{CW} A t_{CW} \quad (2.6)$$

where I_{CW} denotes the intensity of the CW laser, A is the area of the laser spot on the sample, and t_{CW} is the measurement time.

Similarly, for a pulsed laser, the Raman signal S_p is expressed as:

$$S_p \propto I_p A N \tau \quad (2.7)$$

where I_p is the peak intensity of a laser pulse, N is the number of pulses in the measurement, and τ is the pulse width.

The total measurement time required in the measurement is then given by

$$t_p = \frac{N}{f_{rep}} \quad (2.8)$$

where f_{rep} is the repetition rate.

Assume that the area of the laser spot on the sample, A , is the same for both cases, to achieve the same level of Raman signals, the ratio of the effective measurement times between using a CW laser and a pulse laser is given by:

$$\frac{t_{CW}}{t_p} = \frac{I_p f_{rep} \tau}{I_{CW}} \quad (2.9)$$

For Raman analysis of materials that are not sensitive to high-intensity laser irradiation, a pulsed laser can take full advantage of its high peak intensity, which is several orders of magnitude higher than the intensity of a CW laser ($I_p \gg I_{CW}$). However, this advantage can be eclipsed by the short pulse duration in nanoseconds and the low repetition rate.

From another perspective, consider that to generate sufficient Raman signals detectable (signals above the instrument noise) using a single pulse so that $t_p = \tau$ and $N = 1$, the ratio of the effective measurement times between using a CW laser and a pulse laser can be given by:

$$\frac{t_{CW}}{\tau} = \frac{I_p}{I_{CW}} \quad (2.10)$$

In the case of using a single laser pulse for Raman analysis, as long as the Raman signals generated by the single pulse is strong enough to be detected and the degradation threshold for the pulsed laser is the same or greater than that for the CW laser, the pulsed laser is always more efficient. If more pulses are required to detect the Raman signal, then the pulsed laser becomes inefficient due to the low duty cycle.

Consequently, the adoption of a CW laser as the excitation source of the remote standoff Raman system is recommended for the safe measurement of light-sensitive pigments on historical wall paintings. For scenarios where low laser intensity is necessary, pulsed lasers cannot take advantage of their high peak intensity.

2.1.6. Experimental updates

There are options for the laser beam configuration. The collimated beam allows for easy operation *in situ* since ideally focusing is not required when measuring spots at different distances. However, it was found that in the original remote standoff Raman setup, the collimated laser beam was still slightly diverging, which results in a ~4 mm spot at 3 m and a ~8 mm spot at 8 mm. To achieve higher spatial resolution, the mobile remote standoff Raman system has been redesigned and upgraded to fit in a 5X beam expander (Thorlabs BE05M) which could be used to focus the beam at different distances. A higher laser intensity means that less acquisition time is required for detection. The spot diameter of the focused beam at sample is ~1 mm, regardless of the distance in the range of 3–15 m. The maximum laser power at sample is 43 mW, corresponding to an irradiance of 5.5 W/cm².

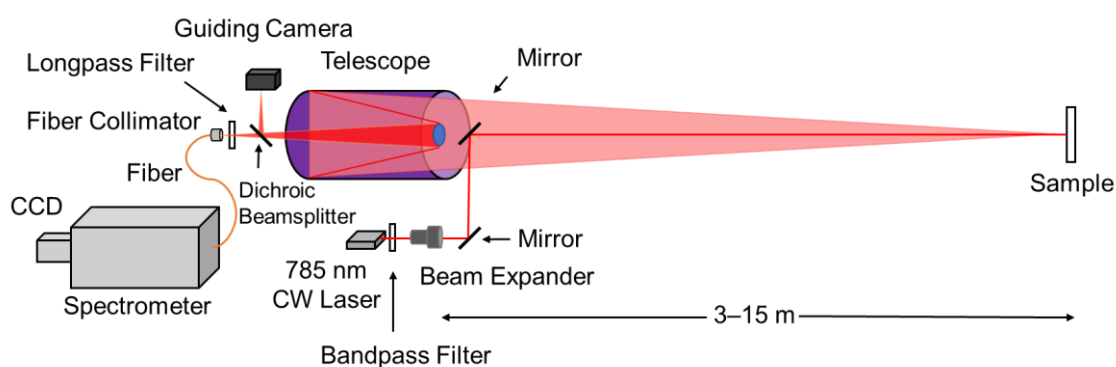


Figure 2.3. Schematic of the standoff Raman instrument setup.

To improve the collection efficiency, a SMA fibre (Ocean Optics QP1000-2-VIS-NIR) with a core size of 1000 μm was adopted to replace the original 200 μm FC/PC one. With much larger core size, the pair of plano-convex lenses used to couple the received signals into the fibre were not needed, which makes the whole design more compact and setting up *in situ* much easier, saving a lot of time for alignments.

The remote standoff Raman system has recently been redesigned for miniaturisation and cost reduction. Although the original 780 nm CW laser source offers narrow linewidth, a compact laser source is preferred for field work. In addition, 780 nm is not a common wavelength for Raman analysis, which means the bandpass and longpass filters and the dichroic beamsplitter are hard to acquire and more expensive. More options are available for components such as filters and lasers at 785 nm, one of the most common wavelengths for Raman spectroscopy. Therefore, a matchbox-size ultra-compact 785 nm CW laser (Integrated Optics 0785L-21A-NI-NT-CF) is employed as the excitation source for the new system. It comes with a pre-installed bandpass filter for eliminating unwanted allowed longitudinal modes and spontaneous emission from the laser output. The maximum output power is increased to 130 mW. The traditional laser controller was not required as all the functions are integrated thus can be controlled by the computer. New dichroic beamsplitter and longpass filter for 785 nm are fitted accordingly to achieve a cut-off wavenumber of $\sim 120\text{ cm}^{-1}$.

2.1.7. Signal processing

2.1.7.1. Wavelength/wavenumber calibration

In order to ensure the accuracy of the collected Raman spectra, and therefore the correct interpretation of the Raman spectra, for any Raman applications, it is of paramount

importance to calibrate the instrument. It is necessary to come up with an accurate calibration procedure before collecting the data, and it is necessary to repeat this calibration process routinely. Over time, even a well-calibrated system will deviate from its optimal working state. Laser wavelength stability could change with operation time and temperature. Optical components such as grating, mirrors, lenses may move slightly over time due to thermal expansion of materials, leading to miscalibration.

Two approaches were widely adopted in wavelength/wavenumber calibration: 1) using a known spectrum from a calibration lamp for wavelength calibration of the spectrometer and the laser line, followed by subsequent wavenumber calibration; 2) direct wavenumber calibration using a range of known standard materials, regardless of the calibration of the excitation wavelength. These standards (e.g. naphthalene and cyclohexane) contain multiple sharp peaks (normally >10) in their Raman spectra with well-known wavenumber information regarding the peak positions. A polynomial fitting can be performed to these peak positions to calibrate the entire wavenumber range. The second method is straightforward and commonly used in commercial Raman systems, while the first method is more orthodox.

To better understand the factors affecting the calibration process, the conversion between wavelength and wavenumber needs to be discussed. Raman shifts are usually reported in wavenumbers, with the typical unit of cm^{-1} . To convert wavelength to wavenumbers of shift in the Raman spectrum, the following formula can be used:

$$\Delta\tilde{\nu} = \frac{1}{\lambda_{ex}} - \frac{1}{\lambda} \quad (2.11)$$

where $\Delta\tilde{\nu}$ is the Raman shift expressed in wavenumber, λ_{ex} is the excitation wavelength, and λ is the Raman spectrum wavelength.

According to the formula, to obtain an accurate Raman spectrum, both the excitation wavelength (λ_{ex}) and the Raman spectrum wavelength (λ) need to be calibrated.

In most cases, the wavelength range in a Raman spectrum starts above the excitation wavelength to avoid the very intense Rayleigh scattering and collect Stokes scattering information. Therefore the Rayleigh line is not collected in the Raman spectrum so that the excitation wavelength (λ_{ex}) cannot be acquired directly. In addition, the excitation source for Raman spectroscopy is typically a single-frequency laser (sometimes called a single-wavelength laser), which operates on a single resonator mode that emits quasi-monochromatic radiation with a very narrow linewidth. However, the excitation wavelength stability may vary depending on environmental factors such as temperature and humidity. From the above reasons, a calibration process for ascertaining the excitation wavelength (λ_{ex}) is required.

The Andor Shamrock 193i spectrograph employed in our remote Raman setup features a motorised dual grating turret, achieving variable wavelength range that is recorded on the CCD camera. This is realised by using a stepper motor. However, no motor can provide exactly the same steps therefore precise repeatability with respect to the rotation angle. In addition, the gratings in the spectrograph automatically reset to zero position when powered off. Therefore, a daily calibration for Raman spectrum wavelength (λ) is required, which would not be a problem for conventional compact spectrometers that use fixed grating configuration.

The calibration process can be described as follows:

- 1) Move the grating to make the wavelength range start at 770 nm, thus covering the Rayleigh line (noted that it is heavily attenuated by the dichroic beamsplitter and longpass filter). Collect a spectrum of the laser line.

- 2) At the same spectral range, collect a spectrum of the Argon/Mercury calibration lamp. A second order polynomial fitting is performed to 13 known spectral lines between 790 and 970 nm. The calibrated laser wavelength can be established.
- 3) Move the grating to make the wavelength start at 780 nm, thus avoiding the Rayleigh line and covering the actual spectral range for Raman measurements. Collect a spectrum of the Argon/Mercury calibration lamp again. A second order polynomial fitting is performed to 13 known spectral lines between 790 and 970 nm. The calibrated wavelength for Raman signals can be established.
- 4) Convert the wavelength to wavenumber using the above formula with calibrated wavelengths of the laser line and the Raman signals.

Since 780 nm was the excitation wavelength for our remote Raman setup, a calibration lamp that has multiple lines covering the wavelength range of 700–1000 nm is preferred. An Ocean Optics HG-1 Mercury Argon Calibration Light Source was selected for the wavelength calibration. The rms residual of the polynomial fitting is ~ 0.03 nm, which translates to an uncertainty of $\sim 0.3\text{--}0.5$ cm^{-1} in Raman shift for a range of $0\text{--}3000$ cm^{-1} using 785 nm excitation (Figure 2.4). The calibration program is written within the MATLAB software package.

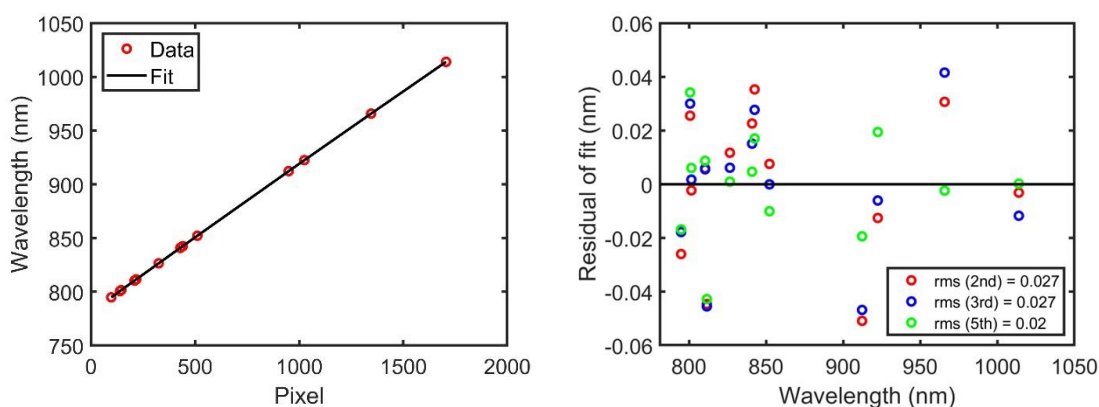


Figure 2.4. Representative 2nd order polynomial fitting and rms residuals of 2nd, 3rd, 5th order polynomial fittings for Raman calibration.

2.1.7.2. Background subtraction and spectral response correction

Background subtraction is performed to remove the contribution from ambient light using the same integration time as the target spectrum but with the laser off. In daylight conditions, the daylight subtraction procedure collects cycles of spectra with the same short integration time, e.g. 1 s. Therefore the problem of varying daylight intensity can be addressed.

The background subtracted spectra were then corrected for the system spectral response. A standard Spectralon white target is mounted at the same distance of the real sample. Then a spectrum of the reflected light on the white standard, illuminated by a Tungsten light source (Ocean Optics DH-2000, with a known continuous smooth spectrum) is acquired.

The baseline subtraction is conducted by smoothing this spectrum using a moving median window, which is then subtracted from the spectral response corrected spectrum. The size of the moving median window can be adjusted depending on the shape of the spectrum. A large window will be efficient in removing the contribution from broad or blended Raman peaks with closely spaced lines, while also removing instrument related broad spectral features which we would want to retain to subtract from the original Raman spectrum such that only Raman peaks remain. For complicated situations, manual subtraction can be performed by a linear or second order polynomial fitting in user-defined regions of interest.

2.1.8. Daylight subtraction

The existence of fluctuating ambient daylight during working hours presents a significant challenge for *in situ* Raman measurements in cultural heritage research. Though the

remote standoff Raman system is designed mainly for indoor work, it is sometimes difficult to prevent daylight in architecture such as cathedrals and palaces that have enormous windows without curtains, and it is usually not easy to gain access for scientific analysis at night. High-power pulsed lasers and time-gated detectors synchronised to the laser pulse duration are normally employed to collect Raman spectra in a short period, which makes daylight contribution insignificant [115]. As discussed earlier, the use of high-power pulsed lasers is not suitable in cultural heritage studies as the potential laser induced degradation poses a threat to heritage objects. The high peak intensity due to a pulse duration of several nanoseconds could easily exceed the damage threshold. The detailed work on laser induced degradation effect will be presented in the following chapter. CW lasers have also been used for long-range outdoor remote Raman measurements, however the experiment was carried out during the night to avoid daylight [116]. An automated online daylight subtraction program was developed in MATLAB software package to address the issue. It can quickly respond to the dramatic change of daylight intensity within seconds using laser modulation (Figure 2.5).

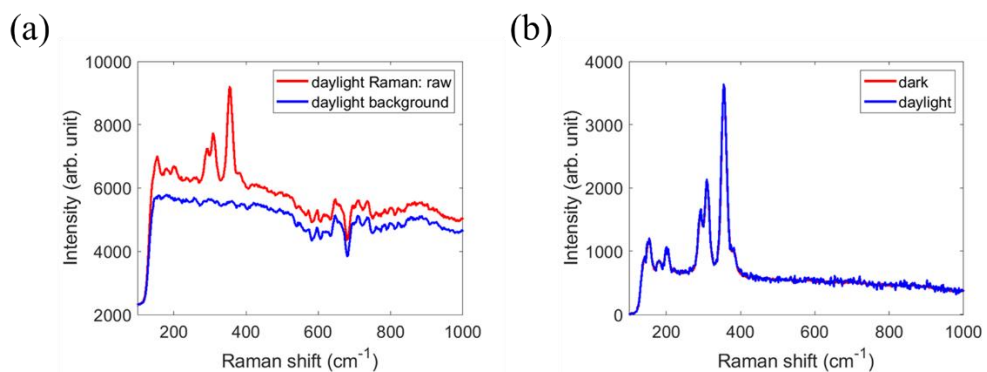


Figure 2.5. Daylight subtraction Raman spectra of an orpiment in animal glue sample. (a) comparison between the Raman spectrum of orpiment at 3.3 m distance placed in front of the window using the remote standoff Raman system with 780 nm CW laser on and off; the absorption band around 675 cm⁻¹ corresponds to H₂O absorption lines at ~823 nm from the atmosphere; (b) comparison of daylight subtracted Raman spectrum with that taken in dark environment. Adapted with permission from [112] © Optica Publishing Group.

2.1.9. Pigment survey

A total of 58 reference paint samples made of typical historical artist pigments in linseed oil, egg tempera, or animal glue were used in this survey [117,118]. The pigment compositions were confirmed by other analytical techniques prior to this study. Details of the pigment composition are given in [117]. The reference paint samples in different binding media were examined by the 780 nm remote standoff Raman system at 4 m employing the collimated beam, resulting in a spot size of ~4 mm at sample. The detailed results are given in Table A1 in Appendix 1.

The remote standoff Raman system is able to identify the majority of the pigments in 1 min and nearly all of them in 30 min, with the exception of most of organic pigments in yellow and red, some copper pigments, (e.g. most of the green pigments), and cadmium pigments. Representative Raman spectra of pigments with different Raman scattering efficiencies are given in Figure 2.6.

Most of yellow pigments are typically hard to distinguish using reflectance spectroscopy alone [118]. For comparison, the remote standoff Raman system can identify almost all inorganic yellow pigments as well as the yellow organic pigment gamboge. Vermilion, realgar, red lead, and chrome red are among the red pigments that are easily identified since they are known to have strong Raman signals [119]. Cadmium red is the only inorganic red pigment that is not detected, due to strong laser-induced fluorescence from cadmium sulfoselenide at this wavelength [71] that saturates the detector within seconds. As discussed in Section 2.1.4, fluorescence has an impact on their spectra, which lowers the signal to noise ratio by increasing shot noise [17,119]. Copper pigments are difficult to detect due to their low intrinsic Raman scattering efficiency and significant absorption at 780 nm [119].

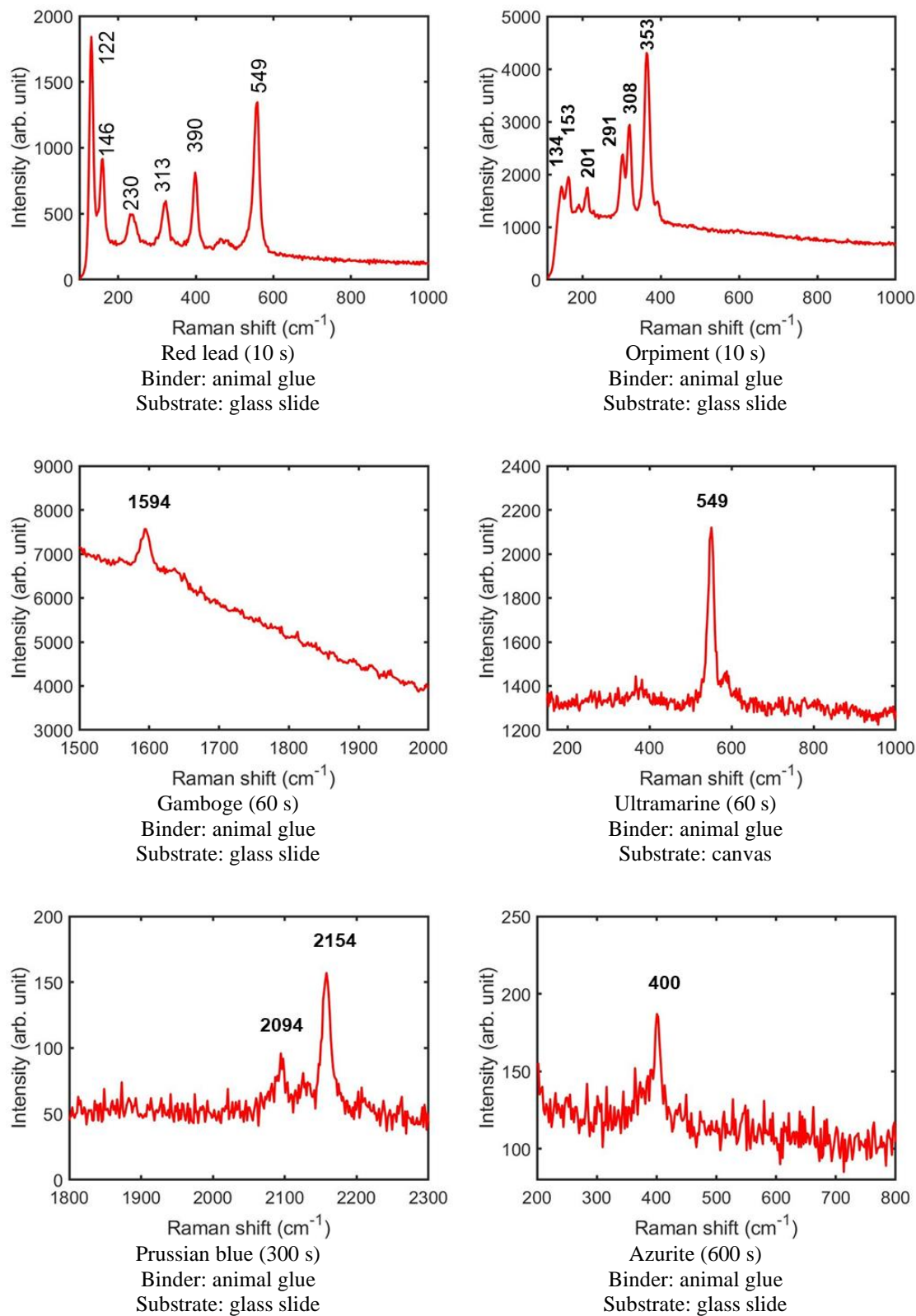


Figure 2.6. Representative Raman spectra of pigments.

2.2. LIBS

2.2.1. Introduction

As stated in the Introduction chapter, remote spectroscopic techniques are required to address the challenges of *in situ* analysis of cultural heritage objects, such as wall paintings, monuments and architectural interiors. Remote Raman spectroscopy has been developed [112] to complement our remote spectral imaging system, PRISMS, for cultural heritage studies, especially for wall paintings. In addition, elemental analysis is often required to confirm the chemical composition of the pigments. However, in rare cases reflectance spectroscopy and Raman spectroscopy combined are still not sufficient to determine definitively the painting materials. For example, Osticioli et al. demonstrated that the Raman spectroscopy managed to detect the blue pigment ultramarine but this technique is not capable of discriminating between the natural and synthetic materials since both have almost the same molecular formula [101]. Elemental analysis by LIBS highlighted calcium impurities in the natural ultramarine, which are absent in the synthetic form [120]. It is known that the differentiation is also difficult for reflectance spectroscopy, as both natural and synthetic ultramarine give similar spectral characteristics.

In a field campaign in a UNESCO site, Mogao caves in Dunhuang, China, machine learning (ML) algorithms were used to automatically interpret the spectral imaging data acquired on wall paintings by PRISMS, identifying the pigments based on their spectral features [121]. Mobile Raman spectroscopy and XRF instruments were used at ground level so that the acquired molecular and elemental information could be used to confirm the pigment classification results based on the spectral reflectance data. XRF is currently the most widely used elemental analysis technique in cultural heritage research, given its

great advantage as being non-destructive. However, emitted X-rays can be easily absorbed by air, which makes it difficult to perform XRF remotely. Worse yet, emissions from light elements are too feeble to escape from the sample without being absorbed. Though being micro-destructive, LIBS can be a suitable alternative to XRF that has its own set of benefits. It is sensitive to all elements and collects elemental information only from the thin ablated layer unlike XRF which gives the bulk signal thus is not depth resolved. No sample preparation is needed. It is possible to conduct LIBS in extreme conditions, such as in vacuum or beneath water. Most important of all, it can be performed remotely by delivering laser pulses at distances and collecting the emissions using telescopes.

The majority of pigments used in paintings, from ancient times to the present, are inorganic compounds that are either naturally occurring coloured minerals or synthesised chemicals. Therefore, pigment identification can be assisted by LIBS analysis if the elements detected in the colorants correspond to chemical compounds of known pigments, as shown in earlier instances.

Significant effort has been paid to the development of stratigraphic analytical methods capable of investigating numerous interfaces across the sample. For instance, paintings are normally heterogeneous systems with a multi-layered structure. One of the most important topics in scientific studies of cultural heritage is to understand the stratigraphy of the paintings in order to evaluate the separate layers, which is technically challenging. Being micro-destructive, one of the unique advantage of LIBS is the ability to conduct depth-profiling analysis of a sample by delivering multiple laser pulses on the same spot and collecting the generated emission signals. Depth profiles can be acquired rapidly, as collection for each spectrum could be done within one second. Depth profiles by LIBS could also be accomplished remotely by using telescopes.

2.2.2. Instrumental design

Raman spectroscopy usually covers a wavelength range of ~200–300 nm starting from the Rayleigh line, which requires high-resolution gratings at appropriate blaze wavelengths. For example, a spectral resolution of 4 cm^{-1} in wavenumber for 532 nm laser excitation translates to 0.1 nm in wavelength. Typical LIBS signals emerge at a wavelength range of ~200–900 nm, much broader than Raman spectra, while the spectral resolution is required to be at a comparable level of 0.1–0.2 nm to distinguish sharp emission lines. It is a trade-off between spectral range and spectral resolution when using a single grating. Other related issues include different spectral sensitivity (sensor response) at different wavelength regions. The conventional solution can be a multi-channel detection system where a fibre bundle is used to distribute the emitted lights to several spectrometers with each configured to cover a narrow spectral range. Alternatively, Echelle spectrograph with the ability to cover broad wavelength range with high spectral resolution can be used for LIBS systems [94,95]. In multi-channel spectrometer configuration or Echelle spectrograph designs, there are no moving parts, allowing a robust design lending itself to incorporation into portable mobile LIBS systems suitable for *in situ* analysis.

Two temporal acquisition modes, namely time-integrated and time-resolved, are feasible for LIBS (Figure 2.7). In the time-integrated mode, the gate width can be long enough to accommodate the entire process of the plasma emission, so that all the emitted photons during the plasma evolution are captured. Non-gated detectors, such as normal CCD, which have a minimum integration time in the order of milliseconds (much longer than the plasma persistence time) can be used for such analysis. In the time-resolved mode, a narrow gate width is used to collect only a portion of the plasma emission, which requires

precise synchronisation of the laser trigger and the fast-gating detector, such as ICCD with a shutter time down to hundreds of picoseconds.

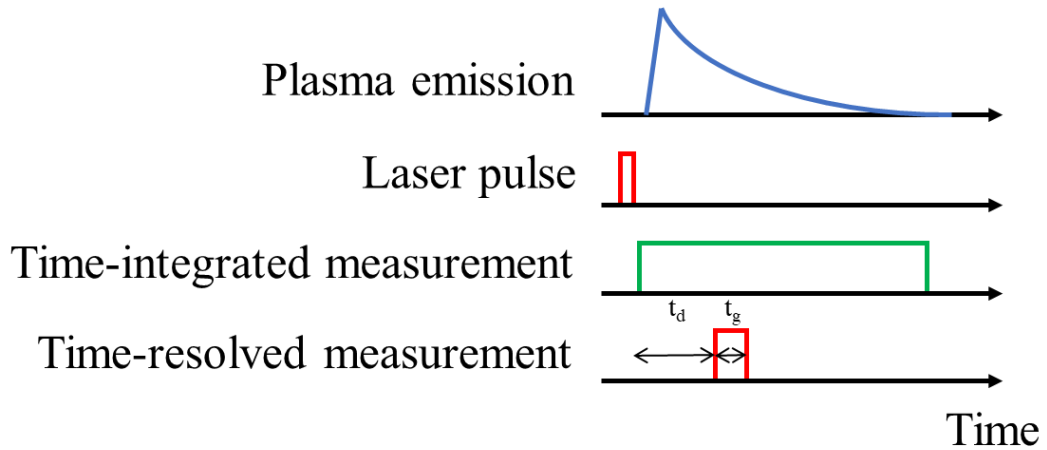


Figure 2.7. Schematics of the temporal evolution of LIBS and the two modes of LIBS measurements.

Designed in an oblique geometry, the overall instrumental design of our standoff LIBS is relatively simpler than that of the standoff Raman spectroscopy system, which adopted a co-axial design. In the oblique mode the laser is directly focused at the distant target and the adjacent telescope collects the emitted lights at an oblique angle, which is mainly determined by the distance between the target and the standoff LIBS system (typically smaller than 1°). The scheme of the standoff LIBS system developed for working at distances > 6 m is shown in Figure 2.8. The Continuum Minilite Nd:YAG laser source can provide 50 mJ pulses (5-7 ns pulse width) centred at 1064 nm, at the repetition rate of 15 Hz. The excitation wavelength of 1064 nm is chosen for not interfering with the LIBS signals (because it is outside of the spectrometer range). A 15X beam expander (Thorlabs BE15M) is used to focus the laser beam to ~ 1 mm in diameter on a distant surface. With the maximum pulse energy of 50 mJ, the peak intensity of the laser pulse

at sample could reach 1.27 GW/cm^2 . A Meade ETX-90 telescope (a Maksutov-Cassegrain reflector with 90 mm clear aperture and 1250 mm focal length) is used for collecting the return light. A 600 μm optical fibre is attached to the rear port of the telescope to send the signals to an Avantes AvaSpec-ULS2048CL spectrometer, configured for 364-925 nm, with a spectral resolution of $\sim 0.5 \text{ nm}$ over the spectral range recorded with a 600 lines/mm grating. The detector is a CMOS with 2048 linear pixels having dimensions of $14 \mu\text{m} \times 200 \mu\text{m}$. Since the main application of this system is to do depth profiles, time-integrated measurement is performed in order to capture the entire emission process. For each spectrum, the detector collected the emission over a period of 1 s, during which a single laser pulse is shot. It is worth noting that wavelengths below $\sim 380 \text{ nm}$ are cut off due to UV absorption by the glass correction plate at the aperture of the telescope. The entire system is mounted atop motorised altitude-azimuth stage, which are controlled by handsets. Another telescope equipped with a guide camera is employed to help remotely align the laser beam and the telescope for collection, and record the position where the LIBS measurement is performed.

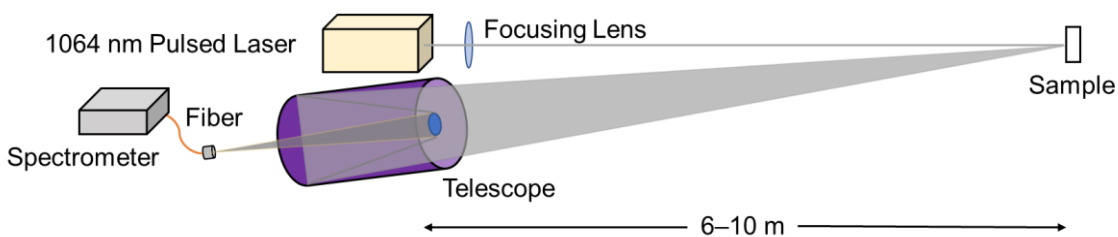


Figure 2.8. Schematic diagram of the standoff LIBS setup.

2.2.3. Signal processing

For LIBS, an in-house written program has been developed in MATLAB software package to batch process the spectra for automated line assignments (Figure 2.9). The peak assignment process can be described as follows:

- 1) First of all, the reference LIBS spectral line database is constructed from lines of common elements extracted from NIST atomic spectral database [122], combined with a table of major analytical emission lines of elements by D. Anglos et al. [123].
- 2) For the experimental spectra, background subtraction is performed using a moving median filter so that net counts for each peak could be calculated. The size of the moving median window can be adjusted depending on the shape of the spectrum. It is found that a large moving median window is suitable for the subtraction of the broad continuum emission (Bremsstrahlung emission).
- 3) Emission lines are identified using the built-in findpeaks function within MATLAB package, with the positions recorded. Then the noted positions are compared with the reference data so that the element identification is achieved with the most likely match. For lines that do not precisely match the reference data, criteria such as a narrow spectral wavelength window can be applied to list possible assignments within the range. Parameters such as threshold of line intensity can be defined to filter out weak signals to accelerate the batch processing.
- 4) All the identified lines are numbered, and the overall results are combined into a table for output.

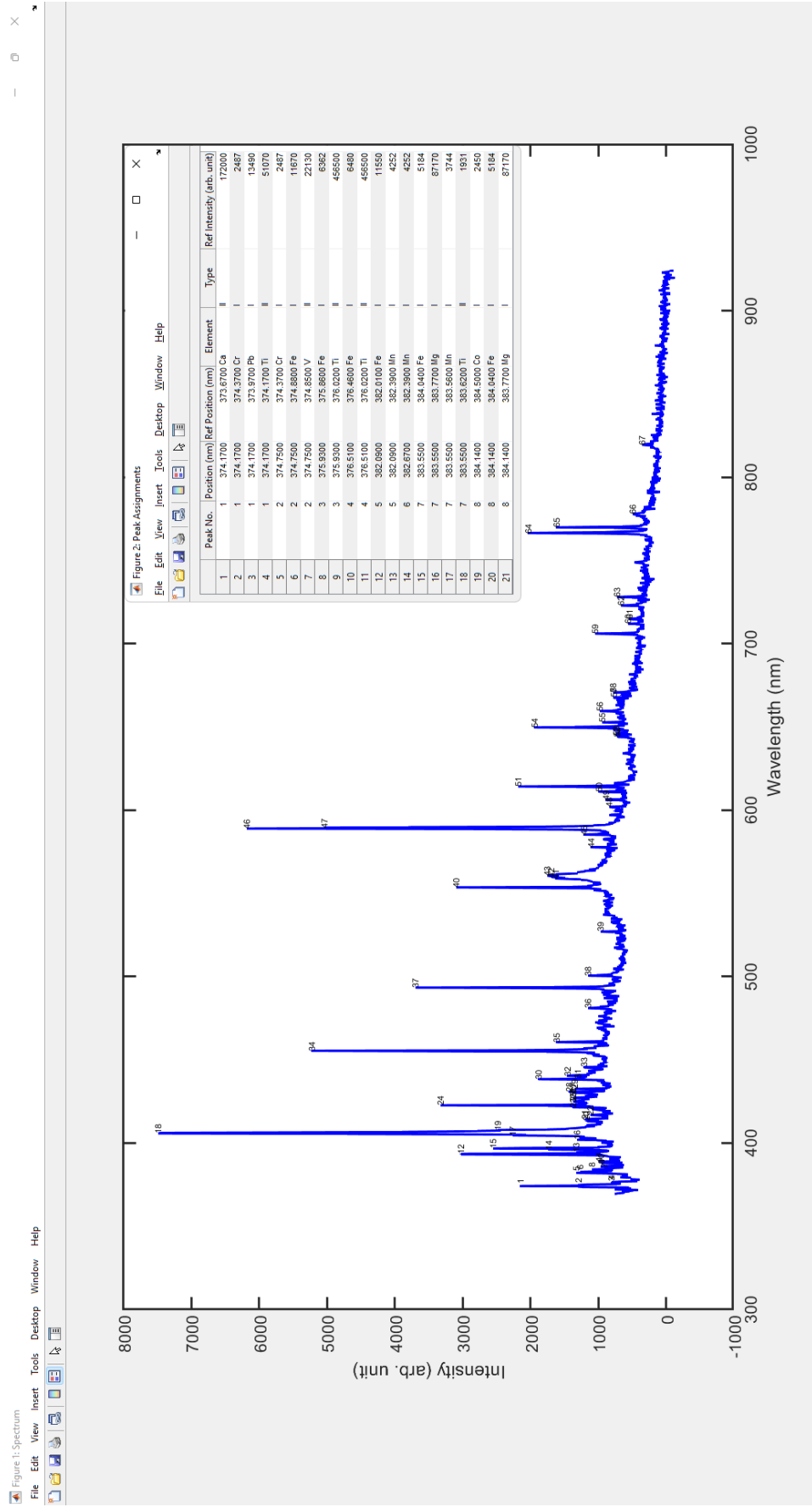
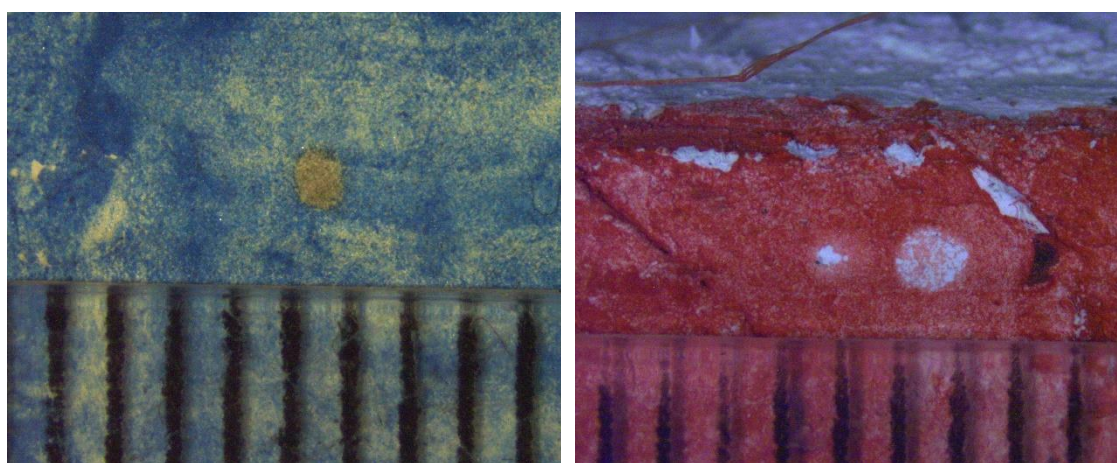


Figure 2.9. The automated LIBS line assignment program.

2.2.4. Pigment survey

Since LIBS is micro-destructive, the pigment survey was conducted on a limited collection of pigments. The selected pigment samples were reference paint samples in linseed oil, egg tempera or animal glue [117,118]. The pigment compositions were chemically analysed with the main composition confirmed by EDX, XRD and FTIR. To better preserve the pigment samples, the pulsed laser beam was focused on the corner of the painted area with a spot size of ~1 mm.

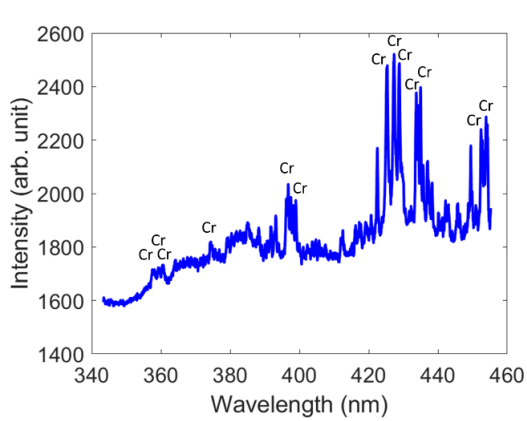


Azurite

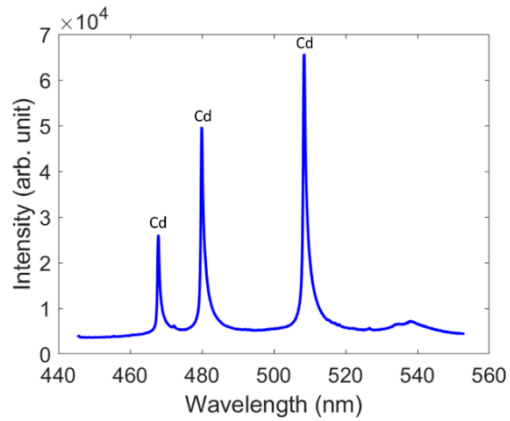
Vermilion

Figure 2.10. Size of the ablated spot caused by LIBS is ~1 mm.

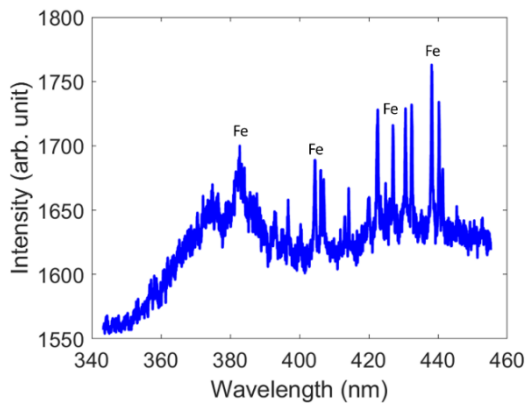
Pigments in various binding media were tested with our standoff LIBS system, which is capable of detecting characteristic emission lines of elements using a single 1064 nm laser pulse at >6 m. Here several representative LIBS spectra of the tested pigments are presented in Figure 2.11, with multiple peaks corresponding to the related elements identified and marked.



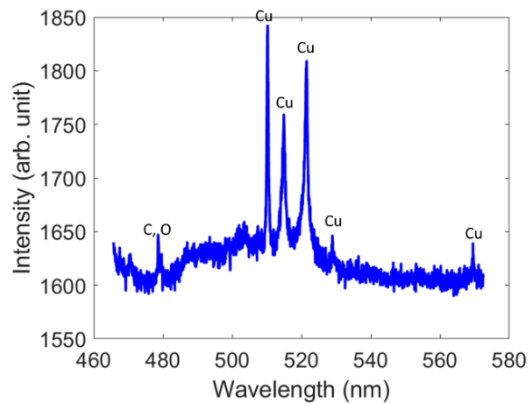
Viridian
hydrated chrome oxide, Cr_2O_3
Binder: oil
Substrate: chalk



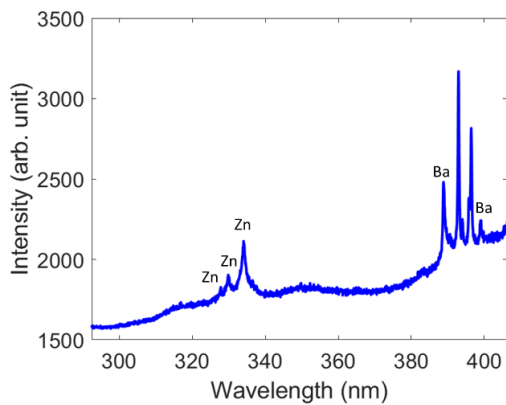
Cadmium red
cadmium selenosulfide, Cd_2SSe
Binder: egg tempera
Substrate: chalk



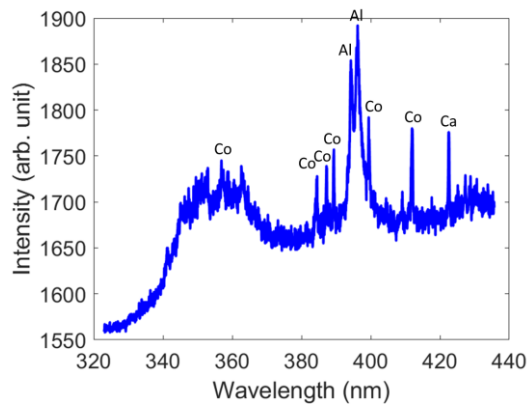
Prussian blue
iron-hexacyanoferrate, $C_{18}Fe_7N_{18}$
Binder: egg tempera
Substrate: chalk



Atacamite
copper(II) chloride hydroxide, $Cu_2Cl(OH)_3$
Binder: animal glue
Substrate: chalk



Lithopone
zinc sulfide and barium sulfate, $ZnS+BaSO_4$
Binder: animal glue
Substrate: glass slide



Cobalt blue
cobalt aluminate, $CoAl_2O_4$
Binder: oil
Substrate: chalk

Figure 2.11. Typical LIBS spectra of pigments.

2.2.5. Depth-profiling analysis

As a micro-destructive method, LIBS is normally utilised for material identification in heritage research only when other non-invasive techniques are unable to offer conclusive results. LIBS, on the other hand, can ablate the materials for depth profiling. When combined with Raman spectroscopy, depth-resolved molecular and elemental information can be acquired at the same spot simultaneously [65,66].

A depth-resolved analysis combining remote standoff LIBS and Raman spectroscopy is designed to evaluate the performance of the newly developed remote standoff LIBS system. A multilayer mock-up paint sample was made in the laboratory. Layers of pigments were applied successively on a plywood board with white gesso substrate. As seen in Figure 2.12a, the multilayer structure comprises of indigo, vermilion, and red lead layers that were painted one after the other in animal glue. The paint sample was mounted vertically at 5 m distance from the remote standoff Raman and LIBS systems set up in an oblique geometry. The laser beams of LIBS and Raman spectroscopy were focused on the same spot at the surface of the sample, which is ~1 mm in diameter. The experimental procedure involved cycles of alternating Raman and LIBS measurements. Each cycle began with a Raman measurement with 10 s integration time and 3 accumulations to remove cosmic rays, followed by a LIBS measurement using one single laser pulse.

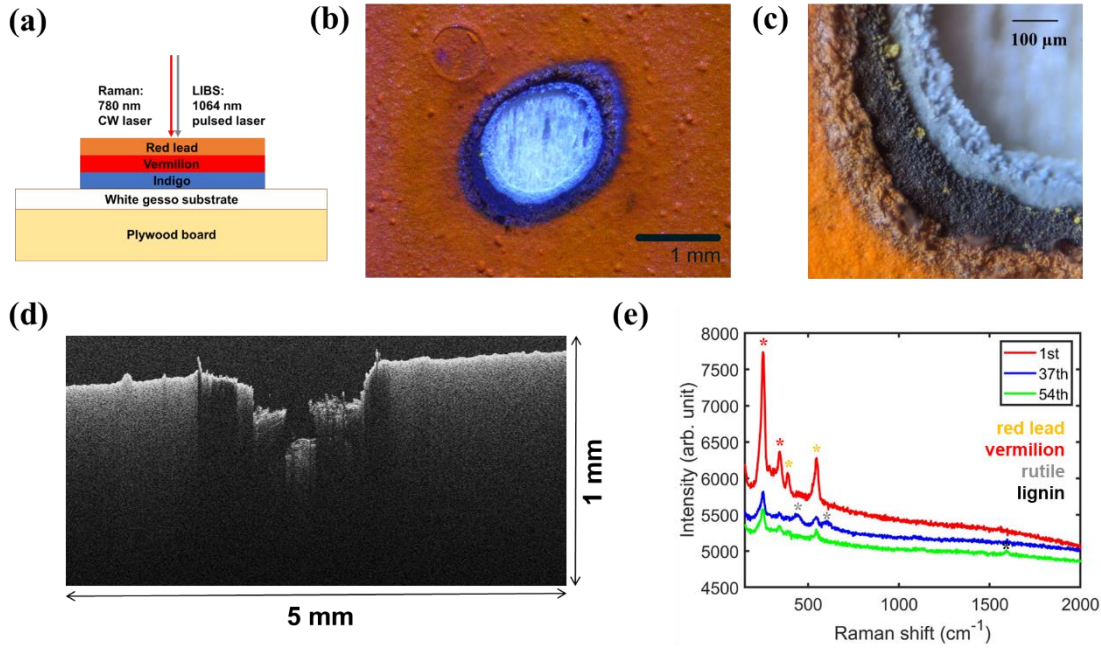


Figure 2.12. (a) A schematic of a multilayer paint sample prepared for the depth-resolved analysis; (b) the ablation crater formed after 70 shots of 50 mW laser pulses; (c) details of the edge of the ablation crater; (d) OCT image of the ablation crater after 70 shots; (e) Raman spectra before the 1st (red), 37th (blue) and 54th (green) 1064 nm shots; an offset of 150 was added to the blue curve for clarity; red lead peaks are marked as orange asterisks; vermilion peaks are marked as red asterisks; rutile peaks are marked as grey asterisks; lignin peaks are marked as black asterisks

70 successive spectra of LIBS and Raman respectively were collected. As presented in Figure 2.12bc, the wall of the ablation crater revealed successive paint layers. It is evident that the vermilion layer was burnt thus turned black (Figure 2.12c). An 810 nm ultra-high resolution optical coherence tomography (OCT) system [124] was utilised to assess the morphology and depth of the ablation crater. The virtual cross-section OCT image is shown in Figure 2.12d.

For Raman spectroscopy, the 780 nm CW laser used for excitation can penetrate the top layer and reveal material information underneath, which makes definitive distinction between layers difficult. Intense red lead (388 and 546 cm^{-1}) and vermilion (252 and 343

cm^{-1}) signals were observed during the 1st Raman measurement (Figure 2.12e). Red lead and vermilion signals were present throughout the 70 laser shots, which most likely came from the wall of the ablation crater. Two Raman peaks at 444 and 608 cm^{-1} corresponding to rutile (titanium dioxide, TiO_2) emerged during the 37th shot, suggesting the laser pulse reached the white substrate layer, given that rutile was identified in the white gesso substrate by another Raman measurement prior to this study. After the 42nd shot, a weak peak at 1592 cm^{-1} was detected, which could be attributed to lignin from the plywood board as the wood layer was exposed.

For LIBS, spectrum obtained at the 2nd shot presented higher intensity of Pb signals when compared to that from the 1st shot (Figure 2.13b). Usually, the 1st shot cleans the sample surface of dust and other contaminants. Pb signals consisting of a strong line at 405.9 nm, a quadlet at 357–373 nm and several weak peaks were detected. Figure 2.13a shows the evolution of intensities of representative emission lines for four elements identified, including Pb (405.9 nm) as in red lead (Pb_3O_4), Hg (546.1 nm) as in vermilion (HgS), Ca (393.3 nm) as in chalk (CaCO_3), and Ti (334.9 nm) in rutile (TiO_2). Until the 7th shot, the ablated material characterised by Pb came from the top red lead layer. Transitions from one layer to another can be observed as the ablation depth rose with successive shots. For example, Hg line intensities significantly increased between the 7th–14th shots when transitioning from the red lead to the vermilion layer (Figure 2.13c), and it remained essentially constant until the 28th shot, at which point it began to decline (Figure 2.13d). During the same period, the intensity of Ca lines increased as well (Figure 2.13e). Ti signals emerged at the 29th shot and culminated at the 38th shot. For comparison, a vertiginous drop was registered in the intensity of Hg lines after the 37th shot. Ca signals decreased sharply after the 41st shot. Although trace Ca and Ti signals were still detected

at the very end (Figure 2.13f), the intensities of all four elements declined to almost zero after the 47th shot.

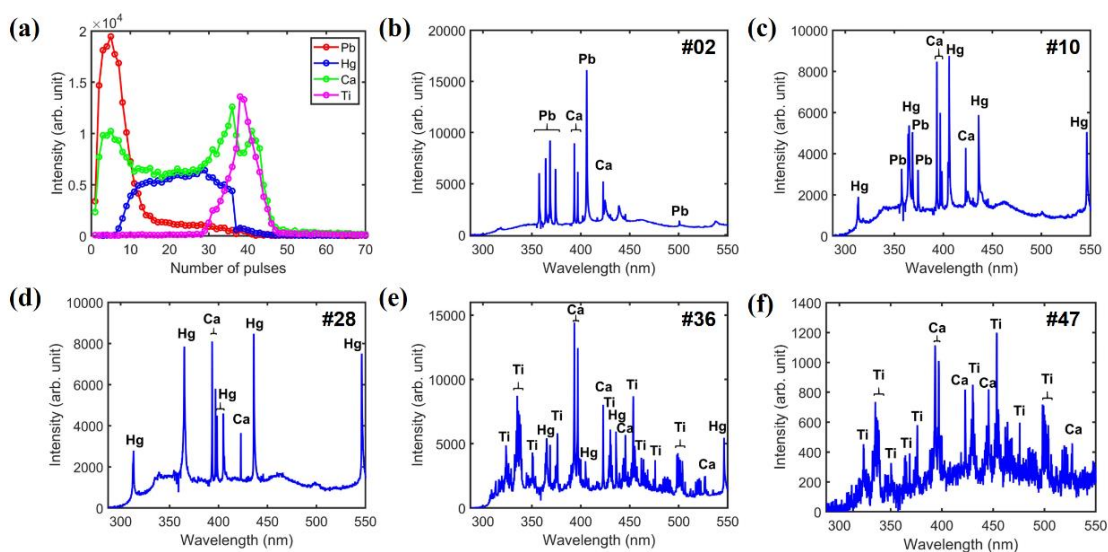


Figure 2.13. (a) The evolution of the line intensities for four elements identified: Pb (405.9 nm), Hg (546.1 nm), Ca (393.3 nm) and Ti (334.9 nm) with increasing shot sequence; (b) emission lines obtained at the 2nd shot; (c) emission lines obtained at the 10th shot; (d) emission lines obtained at the 28th shot; (e) emission lines obtained at the 36th shot; (f) emission lines obtained at the 47th shot.

Based on the results from Raman and LIBS, it can be found that there is a thin red lead layer on top of a thicker vermilion layer. The depth distribution of Ca, as shown in Figure 2.13a, is peculiar. Animal glue, which was utilised as the binding medium, is most likely the source of calcium in the paint layers. Ca was found to be present in indigo (~26.4 wt%) and dried animal glue powder (~2.3 wt%), but not in any other pigments, according to XRF spectroscopy. The first Ca peak in the evolution plot is consistent with the Pb peak, suggesting that Ca is from the binder (animal glue) of the red lead layer. Ca signals maintained at a stable level when the pulses were penetrating through the vermilion layer, as represented by the flat peak of Hg signals until the 28th shot in the evolution plot. After that, Ca intensity began to increase again along with Ti, as opposed to the simultaneous

decline of Hg, revealing the transition from the vermilion layer to the next one. The modest increase of Ca signals observed at the 31st shot may result from the high Ca content in the indigo layer. However, it was unfortunate that Raman spectroscopy did not detect indigo. It is likely that the indigo layer is so thin that it could have been ablated with a single shot. It is noteworthy that LIBS provided insight into the layer structure of the white gesso substrate which was previously unclear. Ti peaked at the 38th shot in the evolution plot, which came from rutile (TiO₂) in the white substrate. For comparison, two peaks of Ca emerged before and after that, at the 36th and 41st shots respectively. In addition, spectral reflectance data (350–2500 nm) recorded at the surface of the white substrate was in good agreement with features of calcite (chalk) and gypsum. It can be hypothesised that the white gesso substrate features a sandwich structure, which is comprised of a top layer of chalk and gypsum that are Ca rich, followed by a middle layer of rutile and then a bottom layer of chalk and gypsum.

2.3. LIF

2.3.1. Introduction

As a non-destructive analytical technique, LIF has been used as a tool in cultural heritage research, such as painted artwork diagnostics and monitoring of biodegradation of stone objects.

Many modern semiconductor pigments, as well as organic pigments and most aged binders, can fluoresce under laser irradiation of high intensity. Fluorescent pigments include natural organic pigments (e.g. lac, cochineal lake, and brazilwood), synthetic organic pigments (e.g. phthalocyanine), and synthetic inorganic pigments (e.g.

semiconductor pigments). Fluorescence of organic pigments (natural or synthetic) usually comes from the presence of delocalised electrons in molecules [69]. Semiconductor pigments fluoresce thanks to the small band gap, which contributes to the relatively narrow and short-lived emissions.

2.3.2. Experimental setup

At first, a prototype LIF setup was proposed to operate at close range (Figure 2.14). The laser source was the Continuum Minilite, the same one as used in our standoff LIBS system. It is a Nd:YAG pulsed laser which can provide 25 mJ pulse energy and 5 ns pulse duration, centred at the third harmonic (355 nm). The laser beam was incident on the sample perpendicularly, at a distance of 20 cm. Fluorescence was collected at 45° to the incident beam by a fibre and was sent to the spectrometer (Ocean Optics HR2000).

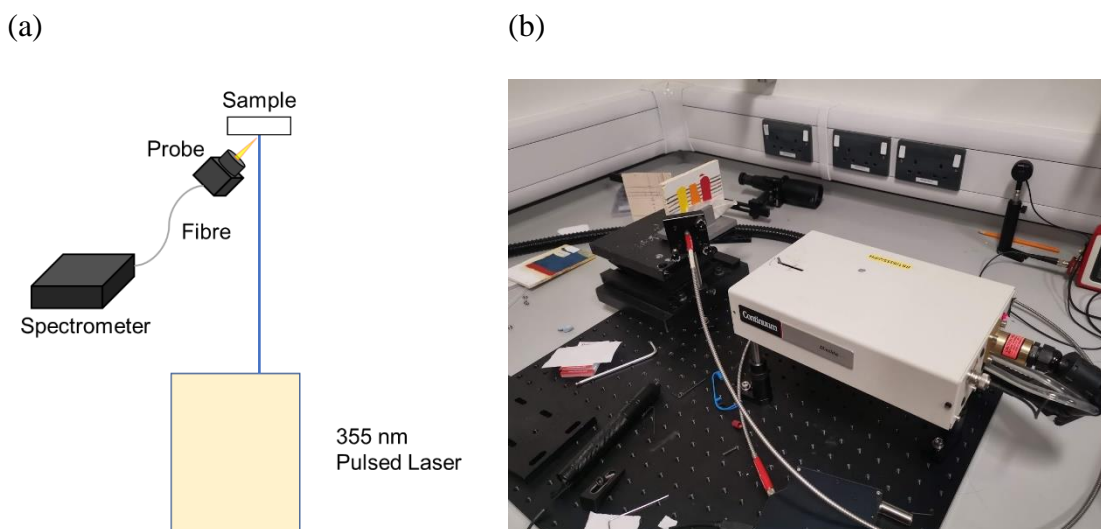


Figure 2.14. A prototype LIF setup operating at close range. (a) Schematics; (b) A photo showing the pigment tests using this LIF setup.

The collection of fluorescence emission was successful using the close-range setup, which led to the development of a standoff LIF system (Figure 2.15). A reflective Newtonian telescope (Meade LightBridge Mini) with 82 mm (3.2") aperture and 300 mm (f/3.7) focal length was used for remote fluorescence collection. Just like the standoff LIBS setup, the system utilised an oblique design where the laser and the telescope were set up abreast at 5.4 m from the sample.

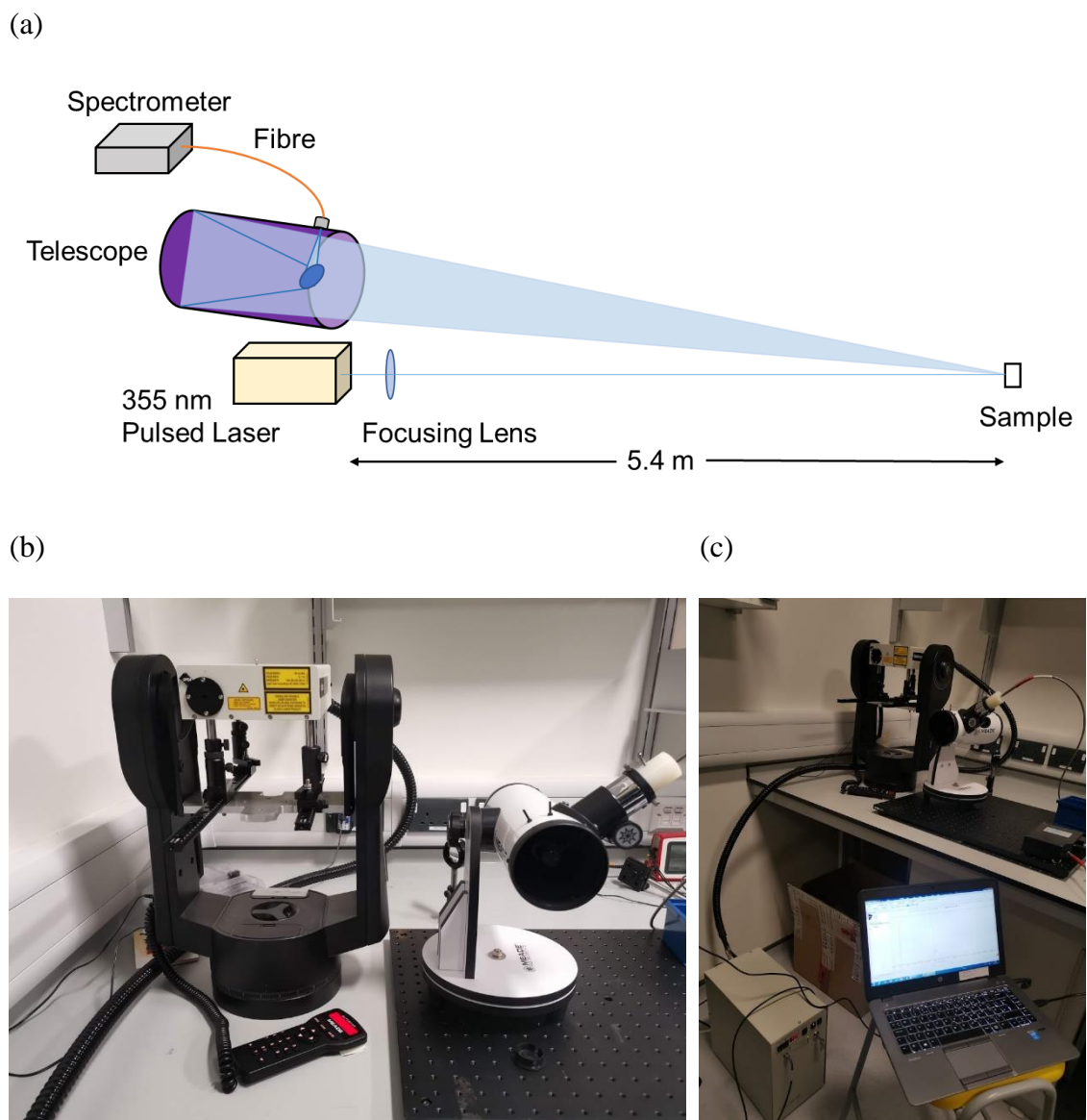


Figure 2.15. A standoff LIF setup operating at 5.4 m. (a) Schematics; (b) the laser and the telescope were set up abreast; (c) Photo of the whole system.

2.3.3. Pigment survey

Reference paint samples with semiconductor pigments such as cadmium-based ones and zinc oxide were selected for LIF tests. All the samples are oil based and had been naturally aged for more than 13 years at the time when the experiments were performed as they were painted during 2006-2007 on plywood boards with chalk substrate in rabbit skin glue [117]. The supplier of all studied pigments is L. Cornelissen & Son. Details of all the studied pigments are listed in Table 2.1.

Table 2.1. Pigment samples

Pigment	Main composition	Supplier	Binding medium
Cadmium yellow (light)	Cadmium sulphide (CdS) with a small amount of Zn, some barium sulphate	L. Cornelissen & Son	Oil
Cadmium yellow (deep)	Cadmium sulphide with a little selenium, Cd(S,Se) (consistent with orange colour), some barium sulphate	L. Cornelissen & Son	Oil
Cadmium red	Cadmium selenium sulphide, Cd(S,Se)	L. Cornelissen & Son	Oil
Zinc white	Zinc oxide, ZnO	L. Cornelissen & Son	Oil
Titanium white	Titanium dioxide, TiO ₂	L. Cornelissen & Son	Oil

Cadmium-based pigments can be classified as II-VI semiconductors. Figure 2.16 shows the fluorescence spectra of the three cadmium-based pigments, ranging from cadmium yellow (light), cadmium yellow (deep), to cadmium red. These synthetic pigments have been widely used since they were introduced in the early 19th century. The compositions range from CdS to CdS_xSe_{1-x} (0 < x < 1). With increasing selenium content, the band gap decreases (band gap energy values for CdS and CdSe are 2.4 and 1.8 eV, respectively, at

300 K [125]), which results in the red shifting of the colour of cadmium-based pigments. It was observed that fluorescence signals increased in wavelength as the pigment colour varies from light yellow to red (Figure 2.16). This pattern is consistent with findings in literature [70,71], but the peak positions were not precisely the same as what has been reported. It could result from differences between suppliers thus the main composition might not be exactly the same. In addition, impurities found in our pigment samples (small amount of Zn, some barium sulphate) could also make a contribution.

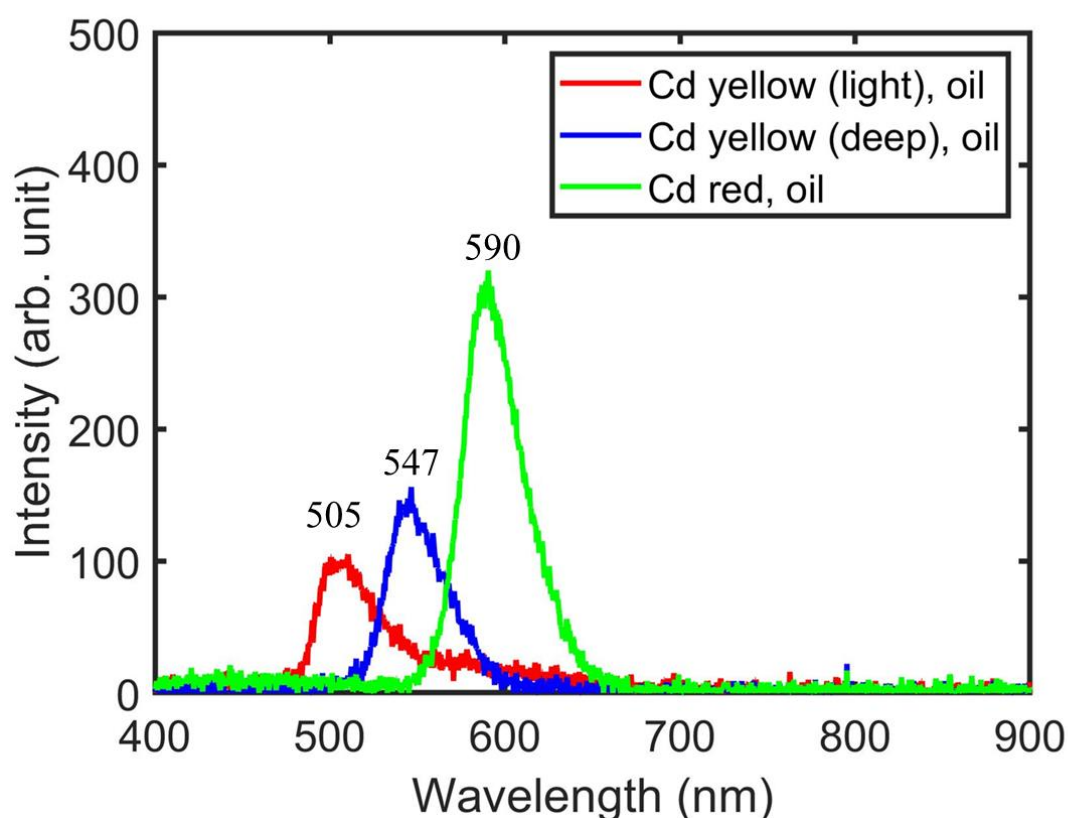


Figure 2.16. Fluorescence emission spectra of cadmium-based pigments in oil.

Comparison in fluorescence emission between two white pigments, zinc white and titanium white, were made (Figure 2.17). The peak position of fluorescence emission from zinc white at 384 nm is consistent with results in literature. A weak and broad peak

at 400–600 nm was detected, a feature also detected from the clean area of the chalk substrate.

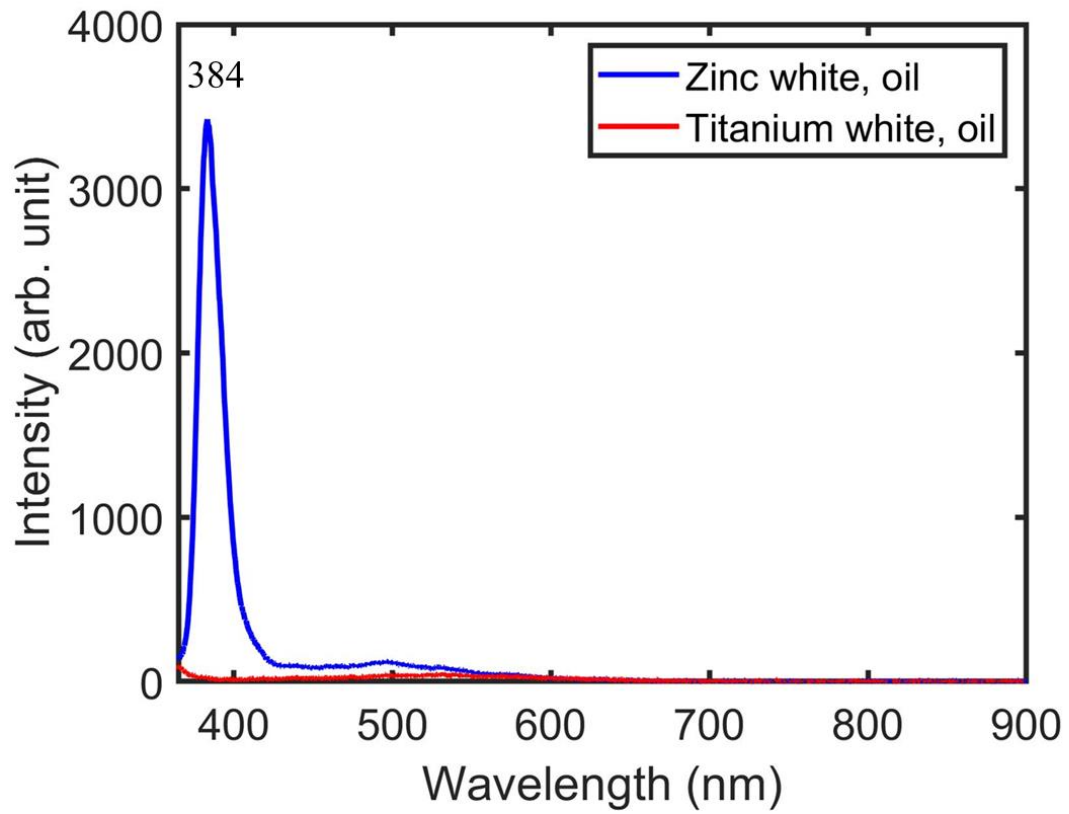


Figure 2.17. Fluorescence emission spectra of two white pigments in oil.

2.4. Conclusions

It is demonstrated that a remote standoff Raman spectroscopy system using a CW laser source at 780 nm can work from a distance of 3–15 m to identify most of common historical artist pigments. CW laser is used for excitation since it is more time efficient for the safe measurements of light-sensitive painting materials, compared with common ns-pulsed lasers. By modulating the laser source through on/off cycles, the 780 nm remote standoff Raman system can operate under the influence of daylight for indoor investigations by automated daylight background subtraction. This remote standoff Raman spectroscopy system can supplement our visible/near-infrared remote spectral imaging system PRISMS.

The developments of remote standoff LIBS and LIF systems at 3–15 m using a pulsed laser source at 1064 nm and 355 nm respectively, are also presented. The data processing is assisted by an in-house written program for automated LIBS line assignment. A depth-profiling analysis is demonstrated to showcase its ability to give elemental information while ablating the materials so that the multilayer structure of a mock-up paint sample is revealed. The application of the non-destructive LIF techniques in cultural heritage studies is briefly discussed. Several fluorescent semiconductor pigments were used to test the standoff LIF system. The results were in good agreement with findings in literature.

Chapter 3

Laser induced degradation of paints

3.1. Introduction

Laser beams can cause damages in materials, which is a particular concern in laser spectroscopy analysis often considered non-invasive in heritage science research, and is the principal concern in the actual deployment of laser based analysis *in situ*.

Raman spectroscopy is a widely used laser technique for the identification of painting materials, given the advantages that it requires no sample preparation and is considered non-destructive [107,119]. As a matter of fact, the above statement of Raman spectroscopy being non-destructive is not entirely true to those familiar with this technique, as they know that with a spot size of a few microns for common commercial benchtop micro Raman systems, the laser intensity could be high enough to degrade, damage or burn the samples even with a relatively low laser power of 0.01–1 mW [20,126]. Heritage studies must be especially careful to ensure that conservation ethics are taken into account when studying the effects of laser-induced degradation.

For cultural heritage materials like pigments and paints, only a small number of systematic studies on laser induced degradation effects have been conducted [20,127]. In literature involving Raman analysis on paintings or pigments, there is often a lack of crucial experimental information such as laser spot size, integration time, which precludes the knowledge of intensity or fluence. Raman spectroscopy in cultural heritage research typically depends more on the operator's experience than it does on set of rules for safety. Finally, if the damage results in changes in the molecular structure and consequently

changes in Raman signals, the worry extends beyond the laser safety of the materials to the precise identification of the original materials.

Attempts have been made to qualitatively and quantitatively evaluate laser induced degradation effects. In Raman microscopy studies, visual observation is often used to verify whether any damage is caused [126,128,129]. However, degradation can be too subtle to be visually perceived under a microscope [130]. Sometimes Raman spectra themselves can be used to confirm degradation products by the emergence of new Raman signals and shifting, broadening or the disappearance of existing signals because of molecular structure changes or the formation of new phases [126,131–133]. However, the sensitivity for Raman spectroscopy as a tool to interrogate degradation changes remains questionable since the degradation can be minute. The amount of materials altered, if any, may be below the Raman system's detection limit. The efficiency of diffuse scattering as measured by reflectance spectroscopy is orders of magnitude higher than that of Raman scattering. Evaluating laser induced degradation in Raman spectroscopy will require a thorough examination utilising methods more responsive to material changes. Previously reflectance spectroscopy is used in our group to examine the degradation of pigments caused by a Nd:YAG ns-pulsed laser at 1064 nm and proved to be highly sensitive [134]. Therefore, a combined system of Raman spectroscopy and reflectance spectroscopy is set up to verify the safety of Raman laser and the sensitivity of Raman as a tool for identification of laser induced degradation effects on pigment samples.

3.2. Intensity and fluence comparison of common laser techniques

Table 3.1 compares the intensity and fluence of typical laser sources used in optical coherence tomography (OCT), non-linear microscopy (NLM), micro-Raman as well as the Xenon light source used in the accelerated light ageing technique microfade [130,134,135]. The laser intensity of the 780 nm remote Raman system is 3 to 5 orders of magnitude lower compared to benchtop micro-Raman instruments.

Table 3.1. Light intensity and fluence comparison.

	P_{av} (mW)	P_{max} (W)	Spot size (μm)	Dwell time (s)	I_{av} (W/cm^2)	I_{max} (W/cm^2)	Fluence (J/cm^2)
Microfade	2		500	600	1		600
OCT	1		10	10^{-5}	1.3×10^3		0.013
NLM	25	2500	1.5	4×10^{-6}	1.3×10^6	1.3×10^{11}	5.2
ns-pulsed laser		2×10^4 to 1×10^7	3000	5×10^{-9}		2.8×10^5 to 1.4×10^8	0.0014 to 0.7
Micro Raman	0.01 to 1		1	1	1.3×10^3 to 1.3×10^5		1.3×10^3 to 1.3×10^5
532 nm CW	33		4000	10 to 1800	0.26		2.6 to 473
Remote Raman 1 (780 nm CW)	45		4000	10 to 1800	0.36		3.6 to 644
Remote Raman 2 (780 nm CW)	43		1000	10 to 1800	5.47		54.7 to 9846

3.3. Selection of pigment samples

A range of historic artist's oil paint samples were examined for laser-induced degradation risks by taking reflectance spectroscopy measurements before and after Raman measurements. In total, 12 pigments are included in the collection, consisting of inorganic and organic pigments, such as cochineal lake. These pigments vary in absorption at the laser excitation wavelength. The basic information for selected pigments is shown in Table 3.2. All of the samples are oil based and have been naturally aged for more than 12 years since they were painted during 2006–2007 on plywood boards with chalk substrate in rabbit skin glue [117].

Table 3.2. Pigment samples.

Pigment	Main composition	Supplier
Red lead	Pb_3O_4	Kremer Pigmente
Vermilion	HgS	Beijing Jinbizhai Pigment Plant
Vermilion light	HgS	Kremer Pigmente
Cochineal lake	Mexican cochineal dyestuff on an alumina substrate	National Gallery laboratory
Realgar (grade 3)	AsS	Beijing Jinbizhai Pigment Plant
Chrome yellow (medium)	$PbCrO_4$	Kremer Pigmente
Lead white	$PbCO_3Pb(OH)_2$	Kremer Pigmente

Ultramarine (synthetic)	$\text{Na}_{6-10}\text{Al}_6\text{Si}_6\text{O}_{24}\text{S}_{2-4}$	Kremer Pigmente
Indigo	$\text{C}_{16}\text{H}_{10}\text{N}_2\text{O}_2$ Indigo and siliceous extender	Kremer Pigmente
Prussian blue	$\text{Fe}_4[\text{Fe}(\text{CN})_6]_3 \cdot n\text{H}_2\text{O}$ (n =14–16) Hydrated iron hexacyanoferrate complex	Beijing Jinbizhai Pigment Plant
Azurite (grade 3)	$2\text{CuCO}_3 \cdot \text{Cu}(\text{OH})_2$ Copper (II)-carbonate	Kremer Pigmente
Verdigris (synthetic)	Copper-(II)-acetate	Kremer Pigmente
Malachite	$\text{CuCO}_3 \cdot \text{Cu}(\text{OH})_2$	Kremer Pigmente

3.4. Experimental setup and procedure

The in-house developed mobile long-range remote standoff Raman spectroscopy system is used for this research. The original setup of the remote Raman system working at 3–15 m has been described in the previous chapter. The output beam is considered as collimated at the aperture with a slight divergence which results in a spot size on the target of ~4 mm at 4 m. The maximum laser power at sample is 45 mW, corresponding to an irradiance of 0.36 W/cm². To achieve higher spatial resolution, the mobile remote Raman system has then been upgraded to fit to focus the beam at different distances. The spot diameter of the focused beam at sample is ~1 mm. The maximum laser power at sample is 43 mW, corresponding to an irradiance of 5.5 W/cm².

Three lasers were used as irradiation source for laser induced degradation tests: a 780 nm CW, a 532 nm CW and a 532 nm pulsed to compare the degradation capability of CW lasers at different wavelengths and pulsed versus CW lasers on painting materials. Apart from the 780 nm CW source for Raman excitation, the other two laser sources were set up in similar arrangements. The 532 nm one is a diode-pumped solid-state (DPSS) laser (Thorlabs DJ532-40), with a maximum output of 40 mW. The beam is collimated at the aperture using a focusing lens which results in a spot size on the target of ~4 mm at 4 m. The maximum laser power at sample is 33 mW, corresponding to an irradiance of 0.26 W/cm². A 532 nm pulsed laser was generated by the secondary harmonic of a 1064 nm Q-switched Nd:YAG source (Continuum Minilite ML II). The maximum pulse energy is 25 mJ. The beam was defocused to a larger spot (8 mm in diameter) so that low intensity was achievable. The tests always begin with a low pulse energy. If no degradation is observed, the energy would be increased. Regardless of the actual size of the laser beam, laser irradiation was always limited to roughly 1 mm² on the sample, and thus allowing

for adjustment of intensity of the incident laser by modifying the beam size without changing the size of the illuminated area.

A combined setup of the remote Raman spectroscopy system and a fibre optic reflectance spectroscopy (FORS) system as shown in Figure 3.1 was used to investigate the laser degradation effects. The laser beam perpendicularly irradiates the vertically placed sample, while a probe is aligned at 45° angle to the laser beam to collect reflectance spectra before and after the laser irradiation within the irradiated area of the sample. A low power tungsten halogen light (Mikropack DH-2000) is used as the illumination source for FORS. A retroreflective probe is used with the FORS, which gives a focused elliptical spot of 0.45 mm by 0.75 mm at sample level. Reflectance spectra are collected by a spectrometer (Ocean Optics HR2000) with an integration time of 200 ms, averaged for 10 times, amounting to 2 s for each measurement. The reflectance calibration was performed using a Labsphere Spectralon white standard.

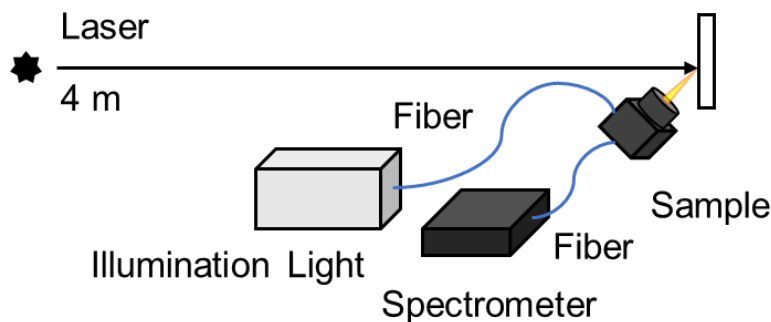


Figure 3.1. Experimental setup for measuring laser induced degradation effect in the paint samples.

In order to have stable light output, the tungsten halogen light (Mikropack DH-2000) has been warmed up for 30 min before taking measurements. For reflectance mode measurements, the dark background is subtracted before the experiments. The stability of the illumination source was tested prior to the experiments by continuously monitoring

the reflectance changes of the white standard sample for 30 min (collecting spectra every 10 s for 30 min).

Before the laser irradiation, 3 reflectance spectra were recorded successively for each sample. Laser irradiation time was chosen according to the typical time required for Raman measurements. A series of Raman spectra were then acquired when the 780 nm laser was used. Right after laser irradiation, a series of reflectance spectra were collected over a period of 6 s to 5 min (depending on the sample). To make sure that no other factors interfered with the degradation tests, another set of measurements were taken as the control beforehand using an identical procedure but without the laser irradiation.

Difference in reflectance (ΔR) was plotted in visible range (400–900 nm) for all the samples, by subtracting the reflectance spectrum before the laser irradiation from the spectra collected after the irradiation. The original reflectance was shown in the same plot (double Y-axis) as a red curve. When a change was detected, evolution of the spectral reflectance change could be extracted from each spectrum and demonstrated in a scatter plot. For Raman spectra, similar processing was adopted. The net counts (background subtracted) and positions of Raman signals representing the pigment material were calculated and then plotted so that the time evolution was visualised.

3.5. A comparison of degradation induced by three laser sources

The aims of the first set of laser-induced degradation tests are:

- 1) Since the powers of the two CW sources (532 nm and 780 nm) are at the same order of magnitude, which wavelength is more harmful to painting materials in terms of laser induced degradation needs to be investigated.
- 2) To check the damage threshold in intensity for pulsed and CW lasers to establish whether CW laser is indeed more efficient for Raman measurements.

Only 4 pigments were used for this research: azurite (oil), realgar grade 3 (oil), red lead grade 3 (oil), vermilion Chinese grade 3 (oil). Right after laser irradiation, 3 reflectance spectra were collected consecutively, amounting to a monitor time of 6 s.

For azurite, no damage was detected with all three lasers. It is known that azurite has low reflectance throughout the visible spectral range. For 532 nm pulsed laser, pulse energy applied on the sample increased from 0.9 mJ all the way up to 11.5 mJ, reaching a maximum power of 2.3×10^6 W and a maximum intensity of 4.6×10^6 W/cm² for a single pulse. No permanent alteration was observed in terms of spectral reflectance (Figure 3.2). Similarly, both intensity and fluence of 30 min irradiation using the two CW lasers did not reach the degradation threshold. This is the scenario where pulsed lasers are more time efficient than CW in Raman analysis of pigments that are not light-sensitive. In this case, given a measurement time of 1800 s (equal to the irradiation time of CW laser), pulsed lasers with a typical repetition rate of 15 Hz and 11.5 mJ energy per pulse could deliver 5–6 times the energy and hence the Raman signal strength when compared with the CW laser. In real *in situ* Raman measurements with the daylight subtraction

considered, that advantage can be doubled. It is worth noting that the calculations are based on the assumption that if one pulse does not cause damage then multiple pulses would not cause damage either, which requires further examination.

Table 3.3. Laser induced degradation results of azurite.

Azurite:	Power¹ (W)	Spot size² (μm)	Dwell time (s)	Intensity³ (W/cm^2)	Energy (mJ)	Fluence (J/cm^2)
532 nm pulsed: not degraded	1.80E+05	8000	5.00E-09	3.58E+05	0.9	1.79E-03
532 nm pulsed: not degraded	8.00E+05	8000	5.00E-09	1.59E+06	4	7.96E-03
532 nm pulsed: not degraded	1.60E+06	8000	5.00E-09	3.18E+06	8	1.59E-02
532 nm pulsed: not degraded	2.30E+06	8000	5.00E-09	4.58E+06	11.5	2.29E-02
532 nm CW: not degraded	0.033	4000	1800	0.26	5.94E+04	472.93
780 nm CW: not degraded	0.045	4000	1800	0.36	8.10E+04	644.90

¹ Power for pulsed and CW lasers are presented in a single column where the power in a single pulse duration for pulsed laser is presented

² Laser irradiation was always limited to around $\sim 1 \text{ mm}^2$ on the sample irrespective of the actual size of the laser beam and thus allowing for adjustment of the incident laser intensity through varying the beam size without changing the size of the illuminated area.

³ Intensity for pulsed and CW lasers are presented in a single column where the intensity for a single pulse is presented

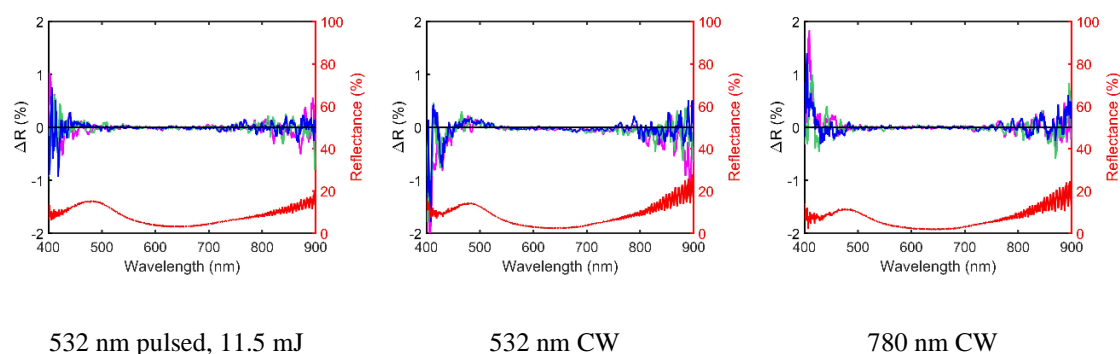


Figure 3.2. Degradation results of azurite: the original reflectance (red curve) and 3 reflectance difference spectra immediately after laser irradiation in 2 s interval (in order of time: magenta, green, and blue).

For red lead, 780 nm CW laser irradiation did not induce any change at the maximum 45 mW power, while for 532 nm CW laser, alteration was detected (Figure 3.3). However, the change caused by 532 nm CW irradiation seems to revert rapidly to the original reflectance spectrum. The first spectrum collected after the irradiation registered a significant dip at around 577 nm, close to the inflection point of the original reflectance spectrum. In the 2nd and 3rd spectrum, this feature became weaker thus a tendency of reversion in reflectance was observed. In such a short period of 6 s, a quick reversion process was captured, suggesting a temporary rather than permanent change. As to the 532 nm pulsed laser, alteration was not seen when using low pulse energy of 0.9 mJ and 2 mJ. At 4 mJ, subtle change in the same wavelength region around 577 nm was noticed. When the pulse energy increased to 8 mJ, a significant dip in the same wavelength region was identified. All 3 spectra taken after the irradiation are almost identical. Whether the change is permanent remains inconclusive, as 6 s might not be sufficient to record the reversion. It seems that here the pulsed laser wins in terms of Raman efficiency by a small margin. Given a measurement time of 10 s (equal to the irradiation time of CW), pulsed lasers with a typical repetition rate of 15 Hz and 2 mJ energy per pulse (the highest value with no degradation observed) could deliver 150 pulses with a total energy of 300 mJ, while during the same time period 532nm CW delivered 330 mJ energy and significant degradation was found.

Table 3.4. Laser induced degradation results of red lead.

Red lead:	Power ¹ (W)	Spot size ² (μm)	Dwell time (s)	Intensity ³ (W/cm^2)	Energy (mJ)	Fluence (J/cm^2)
532 nm pulsed: not degraded	1.80E+05	8000	5.00E-09	3.58E+05	0.9	1.79E-03
532 nm pulsed: not degraded	4.00E+05	8000	5.00E-09	7.96E+05	2	3.98E-03
532 nm pulsed: degraded	8.00E+05	8000	5.00E-09	1.59E+06	4	7.96E-03
532 nm pulsed: degraded	1.60E+06	8000	5.00E-09	3.18E+06	8	1.59E-02
532 nm CW: degraded then reverted	0.033	4000	10	0.26	330	2.63
780 nm CW: not degraded	0.045	4000	10	0.36	450	3.58

¹ Power for pulsed and CW lasers are presented in a single column where the power in a single pulse duration for pulsed laser is presented

² Laser irradiation was always limited to around $\sim 1 \text{ mm}^2$ on the sample irrespective of the actual size of the laser beam and thus allowing for adjustment of the incident laser intensity through varying the beam size without changing the size of the illuminated area.

³ Intensity for pulsed and CW lasers are presented in a single column where the intensity for a single pulse is presented

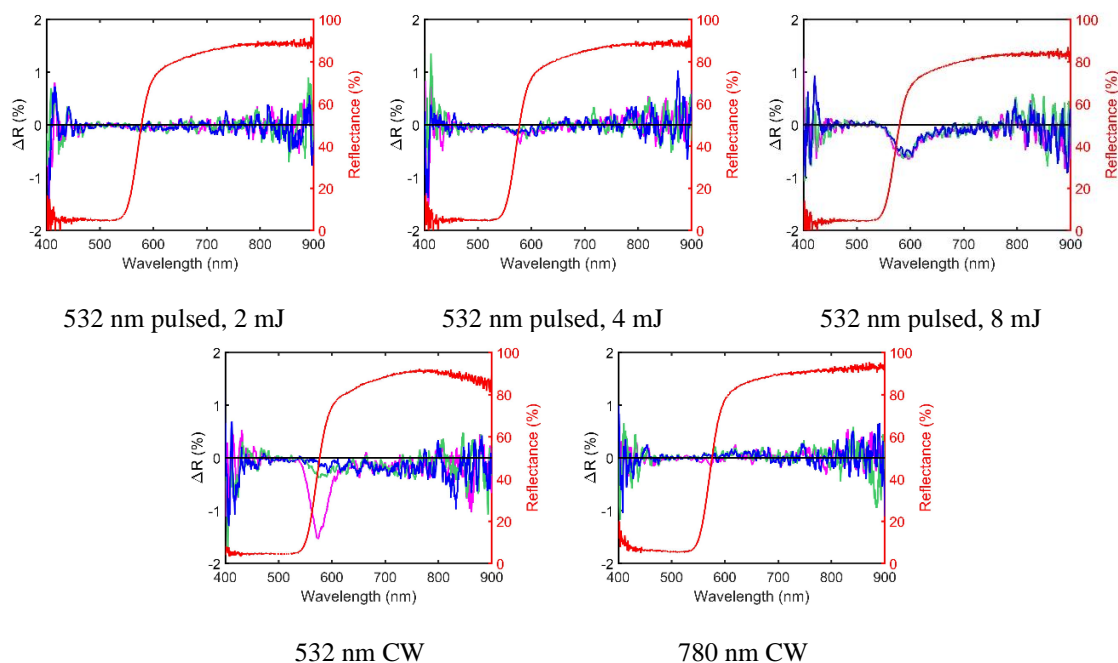


Figure 3.3. Degradation results of red lead: the original reflectance (red curve) and 3 reflectance difference spectra immediately after laser irradiation in 2 s interval (in order of time: magenta, green, and blue).

Realgar is known to be light-sensitive. As tested, the damage threshold in intensity for 532 nm pulsed laser was much lower for realgar than red lead. When the 532 nm pulsed

laser was applied, Figure 3.4 shows that alteration was detected when the pulse energy reached 0.9 mJ, while at a lower level of 0.01–0.1 mJ no change was observed. When applying 532 nm CW laser (33 mW), significant changes in reflectance after 10 s irradiation were detected (Figure 3.4). It is difficult to know if this is a permanent degradation, as the overall 6 s of the 3 consecutive reflectance spectra collected right after the irradiation might not be long enough for monitoring the whole reversion process. In contrast, only subtle signs of changes in reflectance were detected when using higher power (45 mW) at 780 nm, which might be explained by the lower absorption at 780 nm compared with 532 nm. A tiny dip was noticed at 550–600 nm region, similar in wavelength range to the change observed under 532 nm pulsed irradiation. However, the change was quickly reverted in 2 s, as the 2nd curve almost returned to the baseline in ΔR plot, indicating a temporary rather than permanent alteration.

Table 3.5. Laser induced degradation results of realgar.

Realgar:	Power ¹ (W)	Spot size ² (μm)	Dwell time (s)	Intensity ³ (W/cm²)	Energy (mJ)	Fluence (J/cm²)
532 nm pulsed: not degraded	2.00E+03	8000	5.00E-09	3.98E+03	0.01	1.99E-05
532 nm pulsed: not degraded	2.00E+04	8000	5.00E-09	3.98E+04	0.1	1.99E-04
532 nm pulsed: degraded	1.80E+05	8000	5.00E-09	3.58E+05	0.9	1.79E-03
532 nm CW: degraded	0.033	4000	10	0.26	330	2.63
780 nm CW: degraded then reverted	0.045	4000	10	0.36	450	3.58

¹ Power for pulsed and CW lasers are presented in a single column where the power in a single pulse duration for pulsed laser is presented

² Laser irradiation was always limited to around $\sim 1 \text{ mm}^2$ on the sample irrespective of the actual size of the laser beam and thus allowing for adjustment of the incident laser intensity through varying the beam size without changing the size of the illuminated area.

³ Intensity for pulsed and CW lasers are presented in a single column where the intensity for a single pulse is presented

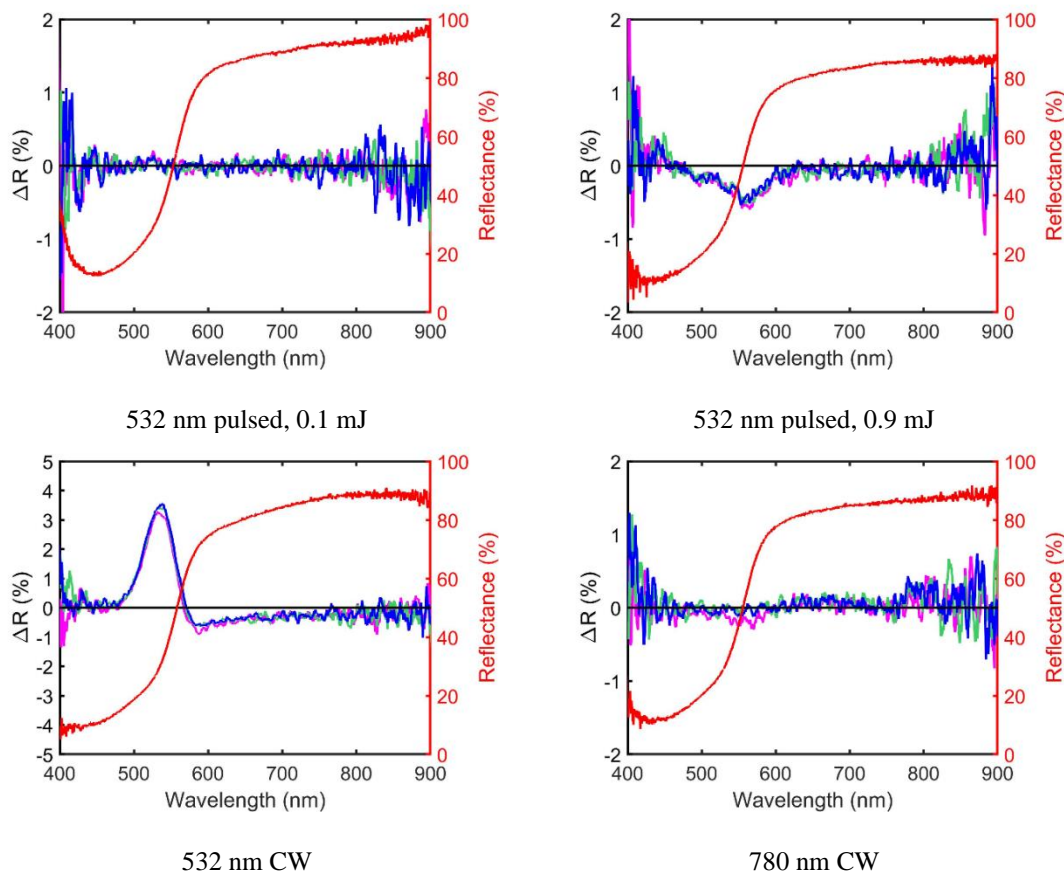


Figure 3.4. Degradation results of realgar: the original reflectance (red curve) and 3 reflectance difference spectra immediately after laser irradiation in 2 s interval (in order of time: magenta, green, and blue).

Another light-sensitive pigment sample examined was vermilion. In the case of 532 nm pulsed irradiation, it seems that vermilion is easier to be degraded than realgar, since 0.3 mJ pulse energy was sufficient to induce the damage compared to 0.9 mJ required for realgar. Degradation and reversion phenomenon related to 532 nm CW irradiation was observed for vermilion. A dip in reflectance difference (ΔR) at ~ 600 nm was detected (Figure 3.5), which almost disappeared after 6 s. There is also a general decrease in reflectance at > 600 nm, similar to the degradation pattern induced by 532 nm pulsed laser which did not revert back. Tiny signs of changes in reflectance at ~ 600 nm, was observed when irradiated by 780 nm CW laser at 45 mW power, which quickly reverted to the initial state in 6 s, suggesting a temporary alteration.

Table 3.6. Laser induced degradation results of vermilion.

Vermilion:	Power ¹ (W)	Spot size ² (μm)	Dwell time (s)	Intensity ³ (W/cm^2)	Energy (mJ)	Fluence (J/cm^2)
532 nm pulsed: not degraded	2.00E+04	8000	5.00E-09	3.98E+04	0.1	1.99E-04
532 nm pulsed: degraded	6.00E+04	8000	5.00E-09	1.19E+05	0.3	5.97E-04
532 nm pulsed: degraded	1.00E+05	8000	5.00E-09	1.99E+05	0.5	9.95E-04
532 nm pulsed: degraded	1.80E+05	8000	5.00E-09	3.58E+05	0.9	1.79E-03
532 nm pulsed: degraded	8.00E+05	8000	5.00E-09	1.59E+06	4	7.96E-03
532 nm CW: degraded then reverted	0.033	4000	10	0.26	330	2.63
780 nm CW: degraded then reverted	0.045	4000	10	0.36	450	3.58

¹ Power for pulsed and CW lasers are presented in a single column where the power in a single pulse duration for pulsed laser is presented

² Laser irradiation was always limited to around $\sim 1 \text{ mm}^2$ on the sample irrespective of the actual size of the laser beam and thus allowing for adjustment of the incident laser intensity through varying the beam size without changing the size of the illuminated area.

³ Intensity for pulsed and CW lasers are presented in a single column where the intensity for a single pulse is presented

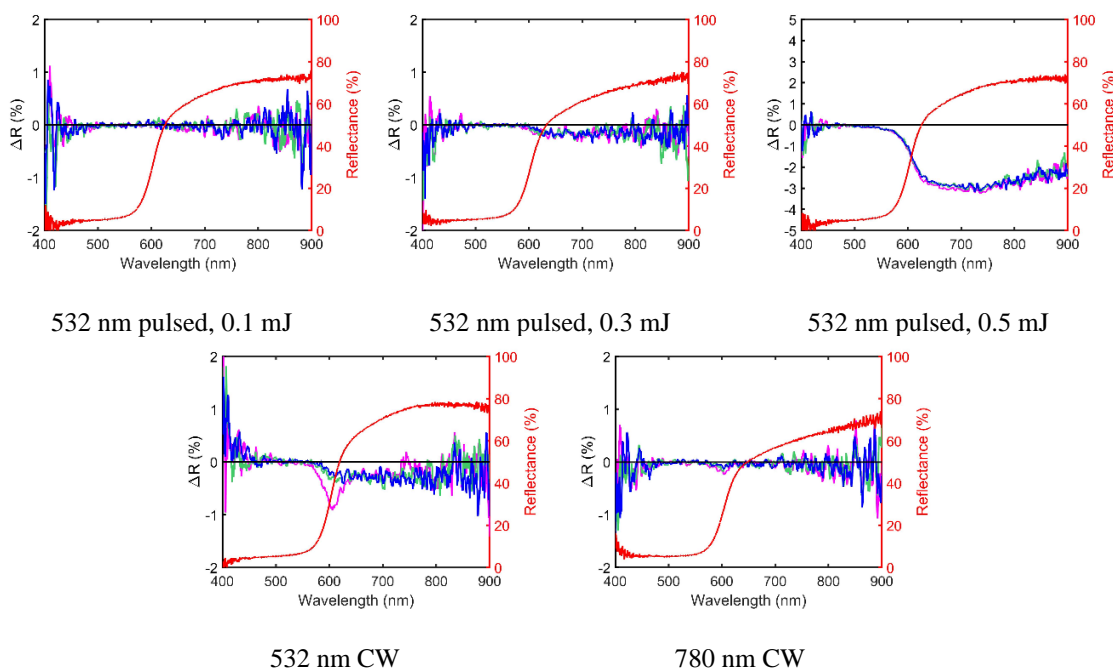


Figure 3.5. Degradation results of vermilion: the original reflectance (red curve) and 3 reflectance difference spectra immediately after laser irradiation in 2 s interval (in order of time: magenta, green, and blue).

3.5.1. CW versus pulse laser at 532 nm

As stated in the previous chapter, there is a trade-off between safe and efficient Raman measurements, which is a critical factor in determining whether to use a pulsed or CW laser as the excitation source for safe and efficient remote standoff Raman measurements.

532 nm was selected for this comparison since it is a wavelength where both CW and pulsed lasers are available in our laboratory. In this analysis, the ns-pulsed laser with a pulse width of 5 ns gives at most 7 orders of magnitude higher intensity in a single pulse than the CW laser, while the CW laser delivers 2–4 orders of magnitude more energy in a time period of 10–1800 s than a single ns-pulse. When compared to a conventional ns-pulsed laser operating at a repetition rate of 1–100 Hz and pulse duration of 5 ns, CW lasers can have a measurement advantage in efficiency of 6–8 orders of magnitude for safe operation below the degradation threshold, if the degradation threshold in laser intensity (power per unit area) are at the comparable level for both types of lasers. However, this assumption proved not true, as shown in Table 3.4 and 3.6, where the degradation threshold in intensity for pulsed lasers is 6–8 orders of magnitude higher than for CW lasers. The most likely explanation is that the heat produced by a pulse can be dissipated between pulses.

In the cases of two light-sensitive pigments, realgar and vermilion, when comparing the CW and pulsed irradiation at 532 nm, it was found that although a single pulse with 5 ns duration delivered significantly lower energy than that from the CW laser with 10 s irradiation time, damage was inflicted due to the considerably higher intensity. To avoid laser-induced degradation, the pulsed laser has to be operated with reduced pulse energy below the damage threshold. Made worse by the low duty cycle, the pulsed laser delivers much less total energy and hence Raman signal, in a given time period as what is required for typical Raman analysis of the three pigments, when compared to its CW counterpart.

In such a scenario, CW wins in terms of Raman efficiency. Take the pulse energy of 0.1 mJ (the highest value with no degradation observed for both pigment samples) for example, given a dwell time of 10 s (equal to the irradiation time of CW), pulsed lasers (assuming 15 Hz) could merely deliver 4.5% the energy and hence the Raman signal when compared with the CW laser. Regarding red lead, the efficiency of the CW laser is comparable to the pulsed laser at 10 Hz repetition rate, where the damage threshold is on the order of 15 mJ/cm² in one pulse and 0.1 W/cm² for the CW laser at 10 s irradiation duration. The pulsed laser is more efficient at 10 Hz repetition rate for pigments that are more resistant to laser induced degradation, such as azurite. However, all the calculations are based on the assumption that accumulation of laser heating for pulsed laser is neglected so that if one pulse does not cause damage then multiple pulses would not cause damage either.

The experimental results supported our previous decision to choose a CW laser for the remote standoff Raman spectroscopy system if it is to be used for all types of pigments including those that are sensitive to laser irradiation.

3.5.2. CW lasers at 532 nm versus 780 nm

The difference in laser induced damage between 532 and 780 nm CW lasers can be summarised. Azurite, red lead, realgar, and vermilion were tested. Except for azurite, the degradation threshold for 780 nm is greater than that for 532 nm. When utilising the 780 nm laser at the same or higher intensity and fluence as the 532 nm laser, either no change or less change (e.g., reversible rather than permanent alteration) was found. This is perhaps unsurprising for red lead, realgar, and vermilion, which all present the 'S' shaped

spectra with point of inflection at >532 nm, implying high light absorption at 532 nm and low light absorption at 780 nm.

3.6. 780 nm CW laser induced degradation effects on a range of common pigments

The upgraded remote standoff Raman system achieved a focused beam with a spot size of around 1 mm at the sample for all operable distances, reaching a maximum intensity of 5.5 W/cm^2 . To confirm the safety of the heritage objects during measurements using the upgraded remote standoff Raman system, a range of 12 historical artist's oil paint samples were chosen, comprising organic and inorganic pigments with varied colours and spectral shapes (Table 3.7). While maintaining the same size of the irradiated area, degradation effects using incident laser intensities of 0.3 W/cm^2 for the previous system and 5.5 W/cm^2 for the upgraded system were compared (Figure 3.6). For pigments with low Raman scattering efficiency, longer irradiation periods were also adopted.

Table 3.7. Laser induced alterations on oil paints

Pigment	Alteration¹	Dwell time (s)	Intensity² (W/cm²)	Fluence (J/cm²)	Monitor time³ (s)
Azurite	<i>N</i>	1800	5.5	1×10^4	180
Red lead	<i>N</i>	10	0.3	3	60
	<i>R</i>	10	5.5	55	60
	<i>R</i>	360	5.5	2×10^3	60
Realgar	<i>R</i>	10	0.3	3	60
	<i>R</i>	10	5.5	55	60
	<i>R/Y</i>	360	5.5	2×10^3	240
Vermilion light	<i>R</i>	10	0.3	3	60
	<i>R</i>	10	5.5	55	60
	<i>R</i>	360	5.5	2×10^3	240
Verdigris	<i>R</i>	1800	0.3	6×10^2	60
	<i>N</i>	60	5.5	3×10^2	300
	<i>Y</i>	1800	5.5	1×10^4	120
Chrome yellow	<i>N</i>	10	0.3	55	60
	<i>R</i>	10	5.5	55	60
	<i>R</i>	60	5.5	3×10^2	300
	<i>R</i>	360	5.5	2×10^3	240
Prussian blue	<i>N</i>	300	5.5	2×10^3	60
Cochineal	<i>N</i>	60	5.5	3×10^2	300
	<i>Y</i>	360	5.5	2×10^3	60
Lead white	<i>N</i>	60	5.5	3×10^2	300
Ultramarine	<i>N</i>	60	5.5	3×10^2	300
Indigo	<i>R</i>	60	5.5	3×10^2	300
Malachite	<i>N</i>	60	5.5	3×10^2	300

In all cases, $\sim 1 \text{ mm}^2$ of the sample was illuminated regardless of the laser spot size

¹ *N* – no alteration; *R* – reversible alteration; *Y* – alteration without reversion

² In case of pulsed laser, the intensity of a single pulse is given

³ Full monitoring duration after laser irradiation

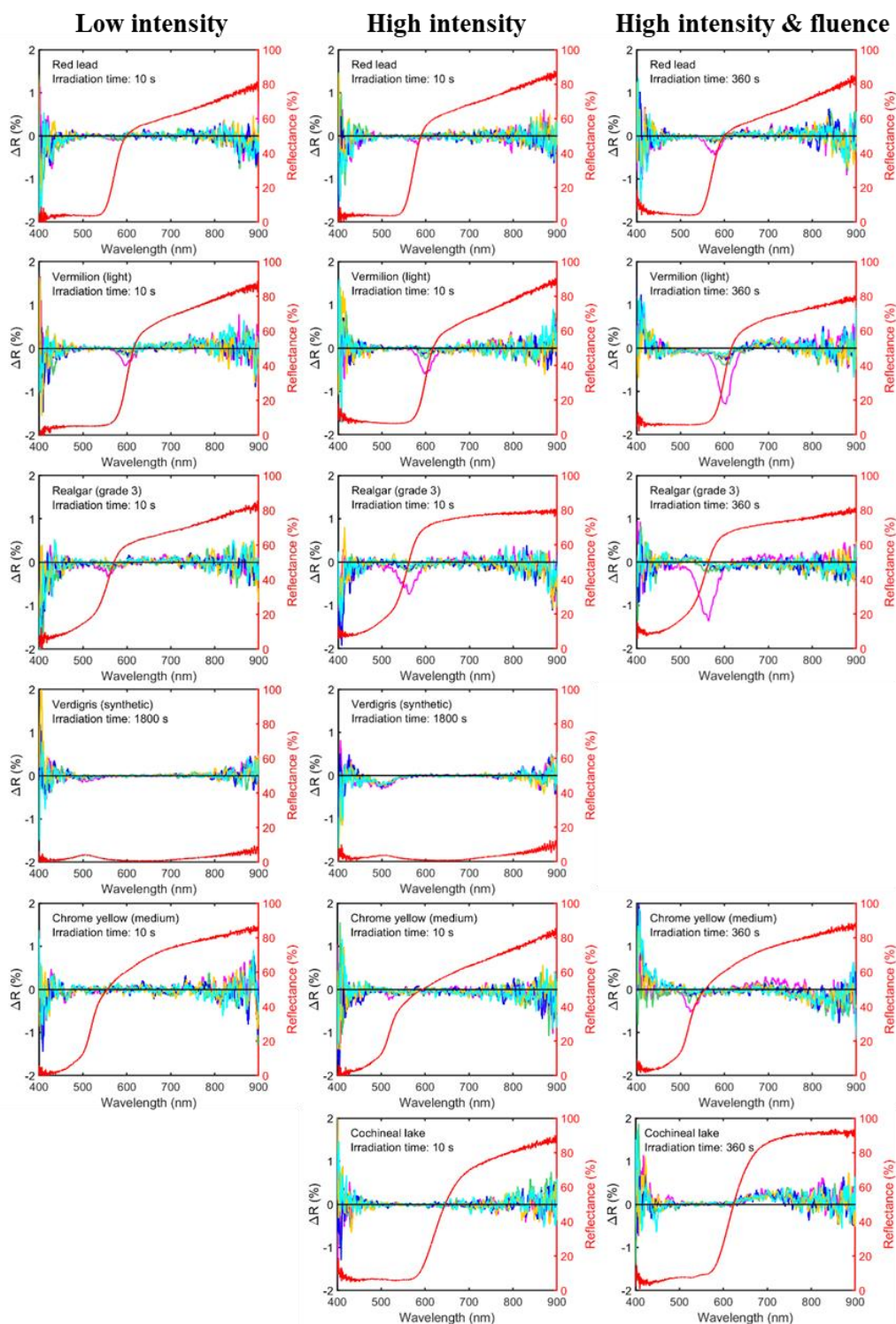


Figure 3.6. Laser irradiation results of oil paint samples with 780 nm CW laser when using a collimated beam at 0.3 W/cm^2 (first column), a focused beam at 5.5 W/cm^2 at the same irradiation time (second column), and a focused beam at 5.5 W/cm^2 at a longer irradiation time (third column): the original reflectance (red curve) and 5 reflectance difference plots immediately after laser irradiation in equally divided time intervals (e.g. every 12 s for 60 s monitoring, or every 48 s for 240 s monitoring) in order of time: magenta, green, blue, yellow, and cyan (monitoring times are given in Table 3.7).

No degradation was observed for Prussian blue, azurite, or cochineal at the intensity of 5.5 W/cm^2 . A more significant alteration was registered in all other pigments, when irradiated by the higher intensity of 5.5 W/cm^2 than the low intensity of 0.3 W/cm^2 . Red lead, realgar, vermilion light, and chrome yellow all showed reversible change with an irradiation duration of 10 s or a fluence of 55 J/cm^2 ; the alteration remained reversible at longer irradiation time of 360 s (Figure 3.6). It took longer for ΔR to fully revert after a 360 s irradiation compared to a 10 s irradiation, which might be related to heat accumulation caused by increased laser fluence. In addition, compared to those irradiated by 10 s, the magnitude of the dip in ΔR was noticeably larger for pigment samples irradiated by 360 s.

It is important to note that with laser intensity of 5.5 W/cm^2 and fluence between 55 and $2.0 \times 10^3 \text{ J/cm}^2$, the samples with high Raman scattering efficiency (red lead, realgar, vermilion, and chrome yellow) only undergo reversible change. Verdigris and azurite, which have low Raman scattering efficiency, exhibit a different behaviour. Even after 1800 s exposure with the stronger laser intensity of 5.5 W/cm^2 , which produced a fluence of 10^4 J/cm^2 , there was no change detected in azurite. Only after lengthier irradiation of 1800 s and 360 s, respectively, were changes of a more lasting character observed in verdigris and cochineal. Whether the degradation was permanent for both pigments requires further investigation, since the monitoring period post irradiation might not have been long enough to capture a potential slow reversion process. In conclusion, none of the pigments examined in Table 3.7 altered permanently after a total of 60 s exposure to the 780 nm laser with an intensity of 5.5 W/cm^2 .

3.7. Sensitivity of Raman spectroscopy for monitoring laser-induced degradation effects

Whether Raman spectroscopy is an effective method for monitoring laser induced changes is examined, since Raman spectra have been used in the past to monitor possible deterioration caused by the Raman laser. This method is still up for debate because there have been few analyses on the relationship between laser intensity, fluence, and changes in Raman spectral characteristics. Burgio et al. [20] detected new peak formation, peak shift, and declined peak intensity during Raman analysis of lead-containing pigments over an intensity threshold, clearly identifying degradation products generated by CW lasers. When darkening occurred on vermilion pigment powder without a binder, Philippidis et al [133] observed an abrupt drop in Raman signals. However, Raman spectroscopy failed to identify laser-induced degradation in other experiments, such as De Santis et al [4] reported on indigo, though damage was clearly visible in microscopic images. This is not surprising given that the efficiency of Raman scattering is only 1 in $\sim 10^6$ – 10^8 . Reflectance spectroscopy is many orders of magnitude more sensitive than Raman spectroscopy, as we previously used it to investigate pigment degradation induced by a Nd:YAG ns-pulsed laser at 1064 nm, which was found to be highly effective [134]. Our combined Raman and reflectance spectroscopy setup (Figure 3.1) allows us to investigate degradation effects in the same area at the same time to see how well Raman spectroscopy can monitor laser-induced degradation.

Raman measurements were performed for red lead, vermilion (light), realgar, chrome yellow and indigo, during 60–360 s of laser irradiation (Table 3.7 and Figure 3.7). The Raman data was acquired as either 36 successive spectra with 10 s integration time each (36×10 s) or 10 spectra with 6 s integration time each (10×6 s). The evolution of Raman

signal intensity, as measured by net peak counts per second above the continuum spectrum, can be visualised to track any small changes over time (Figure 3.7d). Similarly, no alterations in the evolution of the Raman peak position were discovered (Figure 3.7e). However, the change was temporary, as they all returned to their original spectrum over the 60 to 360 s monitoring period after irradiation. Our recent conference paper [136] was the first to report a transient shift in reflectance spectra followed by a reversion. By observing the largest dip in the ΔR spectra, evolution of reversions in reflectance spectra were established (Figure 3.7b). Reflectance spectroscopy detected the alteration but not Raman spectroscopy, which shows that either Raman spectroscopy lacked the sensitivity to detect tiny changes, or the temporal variations in reflectance did not correlate to changes in the pigment's crystalline structure. It is also noteworthy that there were no visual changes. Colour changes ΔE_{00} can be estimated from reflectance spectra before and after laser irradiation [137], using CIE standard D65 illumination and the 1931 standard 2 degrees observer [138]. In virtually all cases, ΔE_{00} was found to be well below 1 and hence undetectable even under a microscope.

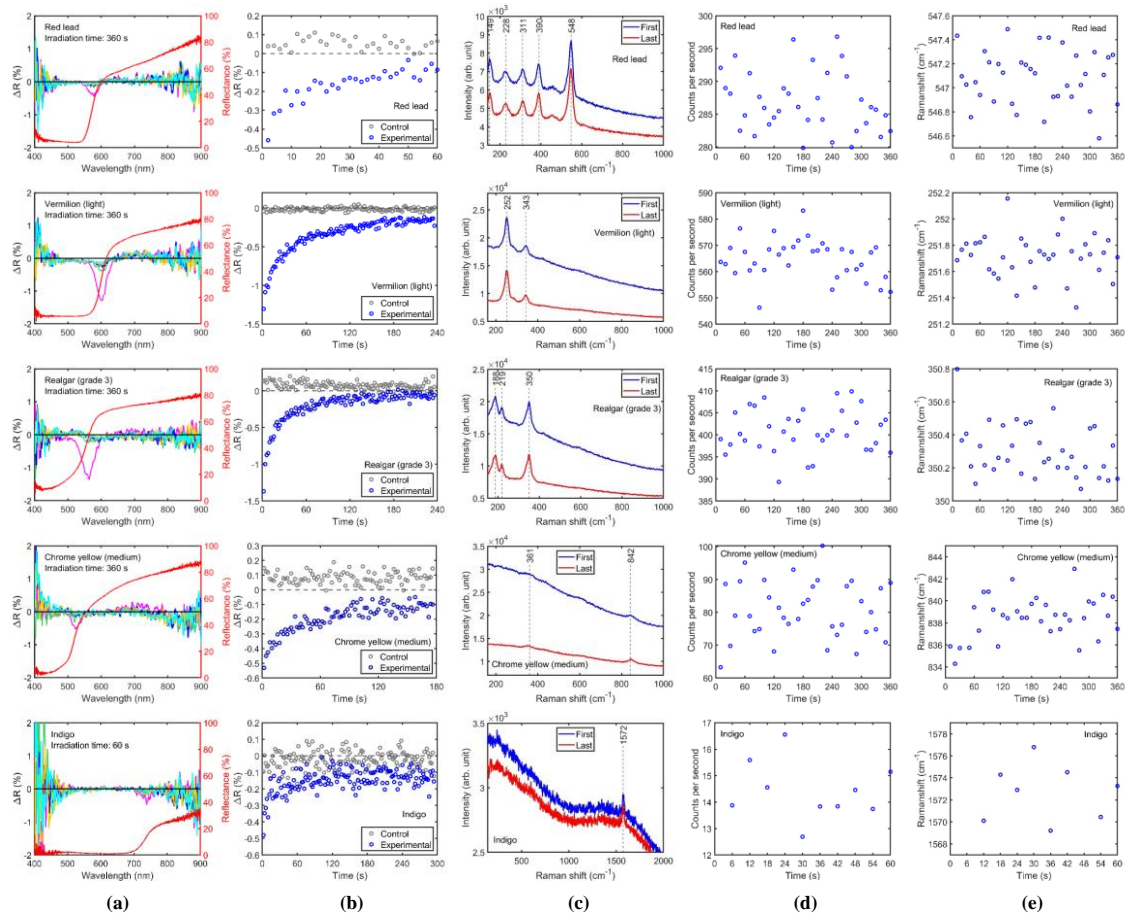


Figure 3.7. Reflectance and Raman evolution of laser irradiation on oil paint samples using focused 780 nm CW laser beam (1 mm diameter). (a) Reflectance difference (ΔR) spectra and the original reflectance of the paints (red curve), five ΔR spectra are plotted at 72 s (for red lead, vermilion light, realgar, and chrome yellow) and 12 s (for indigo) intervals in order of time as follows: magenta, green, blue, yellow, and cyan. (b) Time evolution of the dip in ΔR after laser irradiation (blue data points) compared with control measurement without laser irradiation (grey data points). (c) Raman spectra comparing the first and last spectra during the irradiation. (d) Time evolution during Raman measurements of the net peak power of the strongest Raman peak for each pigment (548 cm^{-1} for red lead, 252 cm^{-1} for vermilion light, 350 cm^{-1} for realgar, 842 cm^{-1} for chrome yellow, and 1572 cm^{-1} for indigo). (e) Time evolution during Raman measurements of the positions of the strongest Raman peak for each pigment, determined by Gaussian fitting of the peaks.

3.8. Conclusions

The upgraded 780 nm remote standoff Raman spectroscopy setup with a focused beam of 1 mm at target and maximum intensity of 5.5 W/cm^2 is shown to be safe under 60 s of continuous laser irradiation without permanent alteration for all 13 common historic artists' paints investigated. Of these, no alteration was detected in azurite, verdigris, Prussian blue, cochineal, lead white, and ultramarine, while reversible alteration was detected in red lead, realgar, vermilion, chrome yellow and indigo. This latter group have relatively high Raman scattering efficiency and typical integration time needed in Raman spectroscopy is much less than 60 s.

Raman spectroscopy did not detect laser-induced alteration that are easily detectable by reflectance spectroscopy. Either these subtle alterations are not the result of changes in crystalline structure of the material, or Raman spectroscopy, as a technique that is orders of magnitude less sensitive than reflectance spectroscopy, was not able to detect the changes. Future work will explore the nature of the laser induced transient and permanent alterations observed in this study.

The choice of a CW laser for remote standoff Raman spectroscopy in paints was justified based on experimental determination of alteration thresholds of each material using a CW laser and a nanosecond pulsed laser at the same wavelength of 532 nm. Raman measurements using CW laser is more efficient in most cases examined, that is shorter measurement time required for the same Raman signal collected, under safe operational limits. The alteration threshold in intensity was found to be higher or similar at 780 nm compared with 532 nm CW laser for all materials tested, which combined with the reduction of fluorescence at 780 nm favoured the use of the 780 nm laser in the remote standoff Raman system.

The upgraded remote standoff Raman spectroscopy system has been adopted as part of the mobile lab research infrastructure for heritage science on offer to the European cultural heritage science research community and beyond through IPERION HS project. This study informed the upgrade decisions and guides the safe operation of the system for heritage materials.

Chapter 4

Applications of remote standoff Raman spectroscopy

4.1. Standoff *in situ* analysis of painting materials at the St Barnabas Cathedral, Nottingham

A beautiful example of Gothic Revival architecture in England is the Cathedral Church of St. Barnabas in Nottingham. In 1844, it was consecrated as a church, and in 1852, as a cathedral. The building's architect was Augustus Welby Pugin (1812–1852), who was also responsible for the interior decoration of Houses of Parliament in London. The Blessed Sacrament Chapel in the Cathedral has been praised as a "prayer book in stone." The Blessed Sacrament Chapel was documented to have undergone restoration in 1933 and 1974 [139]. It is unknown, nevertheless, how much work is attributed to the original decoration or the subsequent restoration.



The Cathedral Church of St. Barnabas in Nottingham



The Blessed Sacrament Chapel

Figure 4.1. The St Barnabas Cathedral, Nottingham and the Blessed Sacrament Chapel.

4.1.1. Complementary methods

The initial imaging of the murals was done using PRISMS [11], an in-house developed remote standoff spectral imaging system for automated scanning of wall paintings and architectural interiors, which can provide spectral reflectance at VIS-NIR region per pixel. Image from 400 to 880 nm were captured using a Jenoptik MF^{cool} CCD camera, a Meade ETX90 telescope, and a PC-controlled filter wheel with 10 filters. Among them, 9 filters are centered every 50 nm from 400 to 800 nm and have a bandwidth of 40 nm each. The last one is centered at 880 nm with a bandwidth of 70 nm. The system is mounted on a PC-controlled alt-az telescope mount. Automation is implemented for both focusing and scanning. For remote illumination, a Tungsten lamp with uniform projected illumination was employed.

High spectral resolution fibre optic reflectance spectroscopic (FORS) measurements of the reference materials were performed using an ASD LabSpec spectrometer (350–2500 nm). *In situ* measurements were carried out in the chapel at reachable heights to supplement the remote results. In the UV/VIS region, the spectral resolution is 3 nm, and in the SWIR, it is 10 nm.

For elemental analysis of the materials, a handheld Niton XL3t X-ray fluorescence spectroscopy (XRF) Analyzer was employed for *in situ* measurements in the chapel at reachable heights to supplement the remote standoff reflectance spectroscopy (by PRISMS) and Raman measurements. It comprises of an Au anode, operating with a maximum voltage of 50 kV and a current of 200 μ A, respectively. Without helium purging, it can detect elements with atomic number $Z > 14$.

4.1.2. Analysis of painting materials

The characteristic lines at 2303 nm and 2346 nm in the SWIR reflectance spectra of several parts of the mural at reachable heights demonstrated that the binding medium is consistent with oil [140].

The standoff Raman system was used to study multiple mural areas at varying distances from the same location on the ground (Figure 4.2). Our research focused on the pigments since it was possible that they would provide details about the historical context of the paintings.

The information gathered from the mural's red section is presented in Figure 4.3. The spectral reflectance features of the red region are similar to either vermilion or cadmium red, according to reflectance spectra that were recorded using the PRISMS remote spectral imaging system (Figure 4.3b). Until the turn of the 20th century, vermilion was one of the most widely used red pigments, when cadmium red, a less hazardous synthetic pigment, first became commercially available in 1919 [141]. It is hard to differentiate between the two pigments by reflectance spectroscopy alone since both pigments exhibit similar spectral reflectance features that are within the range of natural fluctuations brought on by variances in particle sizes and trace impurities. Raman signals characteristic of vermilion were identified in red regions all over the chapel, including the wall near the window (3.6 m), the wall behind the altar (11 m), and the central beam across the chapel (9.2 m). Along with laser induced fluorescence, two significant peaks were found at 252 cm^{-1} and 343 cm^{-1} (Figure 4.3d), which were ascribed to Hg–S stretching vibrational modes [17]. When measuring the red area adjacent to the stained-glass window (Figure 4.3c), multiple absorption lines in the solar spectrum were recorded. They were completely removed by the automated ambient background subtraction. This

is a good example of the standoff Raman system's capability of detecting and analysing pigments remotely under the influence of daylight.

(a)



(b)



(c)



(d)

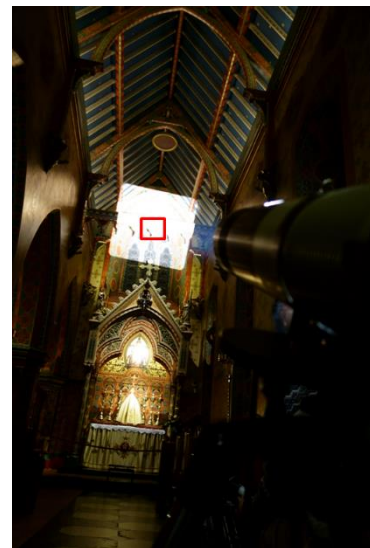


Figure 4.2: *In situ* remote standoff Raman investigation of painting materials in St Barnabas Cathedral's Blessed Sacrament Chapel, Nottingham. (a) Deployment of the remote standoff Raman setup. (b) Remote standoff Raman analysis at a distance of 11 m. (c) Areas on the wall behind the altar (11 m). (d) Areas on the central beam across the chapel (9.2 m).

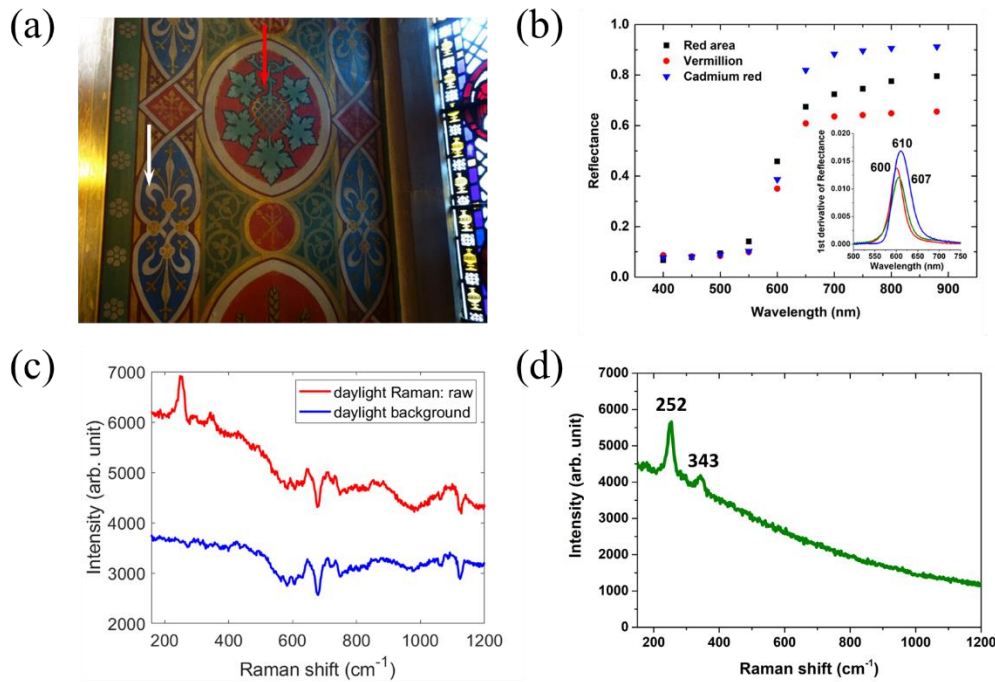


Figure 4.3. Investigation of a red area in the chapel from a distance: (a) colour image of part of a wall painting near a stained-glass window (b) reflectance spectra collected with the remote spectral imaging system PRISMS of the red area (black filled squares) indicated by the red arrow in (a) compared with PRISMS spectra of reference samples of vermilion (red dots) and cadmium red (blue triangle) oil paints; the inset shows the first derivative of the reflectance spectra of cadmium red (peak at 610 nm), and two vermilion oil samples from two different sources (peaks at 600 nm and 607 nm); (c) the raw remote standoff Raman spectrum of the same red area (red), and the background spectrum collected over the same integration time with the laser off (blue) presenting several absorption bands of the solar spectrum (the band around 675 cm^{-1} corresponds to H_2O absorption line at $\sim 823\text{ nm}$ from the atmosphere; the lines around 1056 and 1117 cm^{-1} corresponds to Ca II lines at ~ 850 and $\sim 854\text{ nm}$ from the solar spectrum) ; (d) the processed spectrum after daylight subtraction. Adapted with permission from [112] © Optica Publishing Group.

No cadmium was found in portable XRF measurements of various regions at accessible heights, therefore there is no evidence for cadmium red, thus no evidence for post-1919 material on the mural.

A white area at 4 m distance from the standoff Raman system was analysed right next to one of the red areas neighbouring the window (as indicated by the white arrow in Figure 4.3a). Reflectance spectroscopy, again, is unable to identify the white pigments. In the white area, the remote standoff Raman system recorded a modest peak at $991\pm 0.5\text{ cm}^{-1}$ (Figure 4.4a), which could correspond to the symmetric stretching mode (ν_1) of the S–O bond in BaSO_4 [142]. The possible pigment candidate could be *constant white* (barium sulfate, BaSO_4) or *lithopone* (a mixture of barium sulfate and zinc sulfide, BaSO_4 and ZnS). Zinc sulfide is difficult to detect with Raman spectroscopy because of its low Raman efficiency [143]. The major signal of ZnS at 348 cm^{-1} was not detected in the lithopone reference sample. Ba, Zn, and trace Pb were identified in XRF measurements of several white regions at accessible heights (Figure 4.4b), supporting the identification with lithopone. However, BaSO_4 is frequently used as a paint extender for zinc white (ZnO), which is a common white pigment that has been used since the 19th century. Its main Raman signal at 438 cm^{-1} is easily detectable, but it was not observed here. If there was ZnO , we should be able to detect it. As a result, lithopone is the most plausible identification of the white pigment.

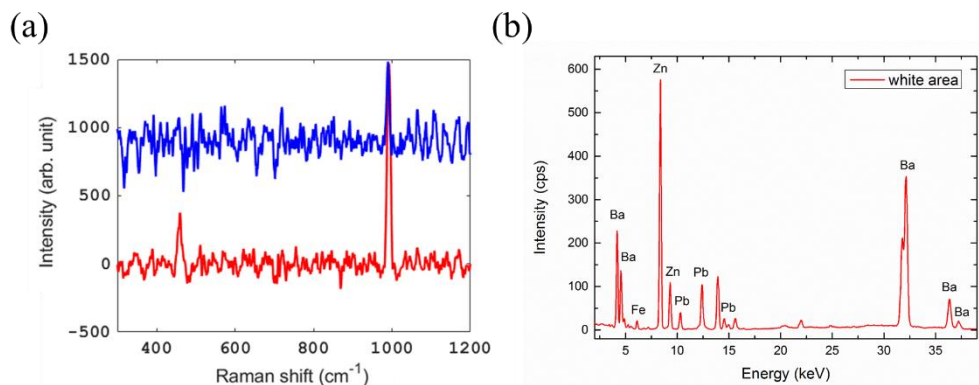


Figure 4.4. Standoff inspection of a white area in the chapel (indicated in Figure 4.3a by the white arrow): (a) Standoff Raman measurement of a white area (blue) at a distance of 4 m compared with a sample of lithopone powder measured from the same distance in the laboratory (red); the baseline subtracted spectra are smoothed using a moving median filter of 6 cm⁻¹. (b) An XRF measurement of a similar white area at an accessible height. Adapted with permission from [112] © Optica Publishing Group.

Lithopone was first patented (in England) and commercially produced in 1874, which was superseded by titanium white by the 1930s [144]. The identification of lithopone suggests that the current painting scheme in the chapel dates to a time period that is after the church's 1844 consecration but before the 1933 reconstruction. There were documents of renovations to the cathedral's main components in the early 20th century. It is however unclear whether this included any alterations to the Blessed Sacrament Chapel.

4.2. Standoff *in situ* investigation of wall paintings at the Convent of Mercy, Nottingham

Remote Standoff *in situ* Raman analysis of wall paintings had been performed in a 2020 field campaign in the chapel of the Convent of Mercy (Figure 4.5a), which was historically affiliated to the Cathedral Church of St. Barnabas in Nottingham. Same with the cathedral, the Convent of Mercy was designed by Augustus Welby Pugin and built in 1846 [145] [139].

Different areas of the mural were studied using the remote standoff Raman system from the same location on the ground (Figure 4.5b). There was no curtain in the chapel so that the Raman measurements were acquired using an automated daylight subtraction process using laser modulation, which enabled the analysis to be conducted during daytime. The experimental setup was the upgraded system with a focused beam of ~1 mm spot. Details of the setup are described in Section 2.1.6.

The remote standoff Raman system was positioned over 6 m away from the wall paintings. The investigation was conducted in a square-shaped cleaning test area (at a height of 4 m), where the surface overpaint layers have been removed, revealing the previous decoration underneath. The red pigment was identified as vermilion, a common red pigment used until the early 20th century (Figure 4.5c). The finding is in line with our prior analysis in the Blessed Sacrament Chapel of the neighbouring Cathedral Church of St. Barnabas, where vermilion was the primary red pigment applied [112].

The surface white paint exhibited Raman signals at 448 and 609 cm^{-1} as presented in Figure 4.5e, which correspond to rutile (titanium dioxide, TiO_2). The earliest manufacture of synthetic rutile in England was reported in 1948 [146]. In the blue pattern on the surface

paint layer (Figure 4.5d,f), another modern synthetic pigment, phthalocyanine blue (PB15), was detected [17,119,147]. Copper phthalocyanine (CuPc) was synthesised for the first time in 1927 [148]. Further investigation reveals that the positions of identified Raman peaks, as well as the intensity ratios of the peaks, are consistent with PB15:3, the β -form of CuPc [147]. In 1949, the manufacture of β -CuPc was patented in the United States. It was first produced in Europe in 1953 [149].

In conclusion, based on the pigments identified on the surface, the overpaint layer was most likely applied after the 1950s, while the underneath decoration layer was most likely painted before the early 20th century.

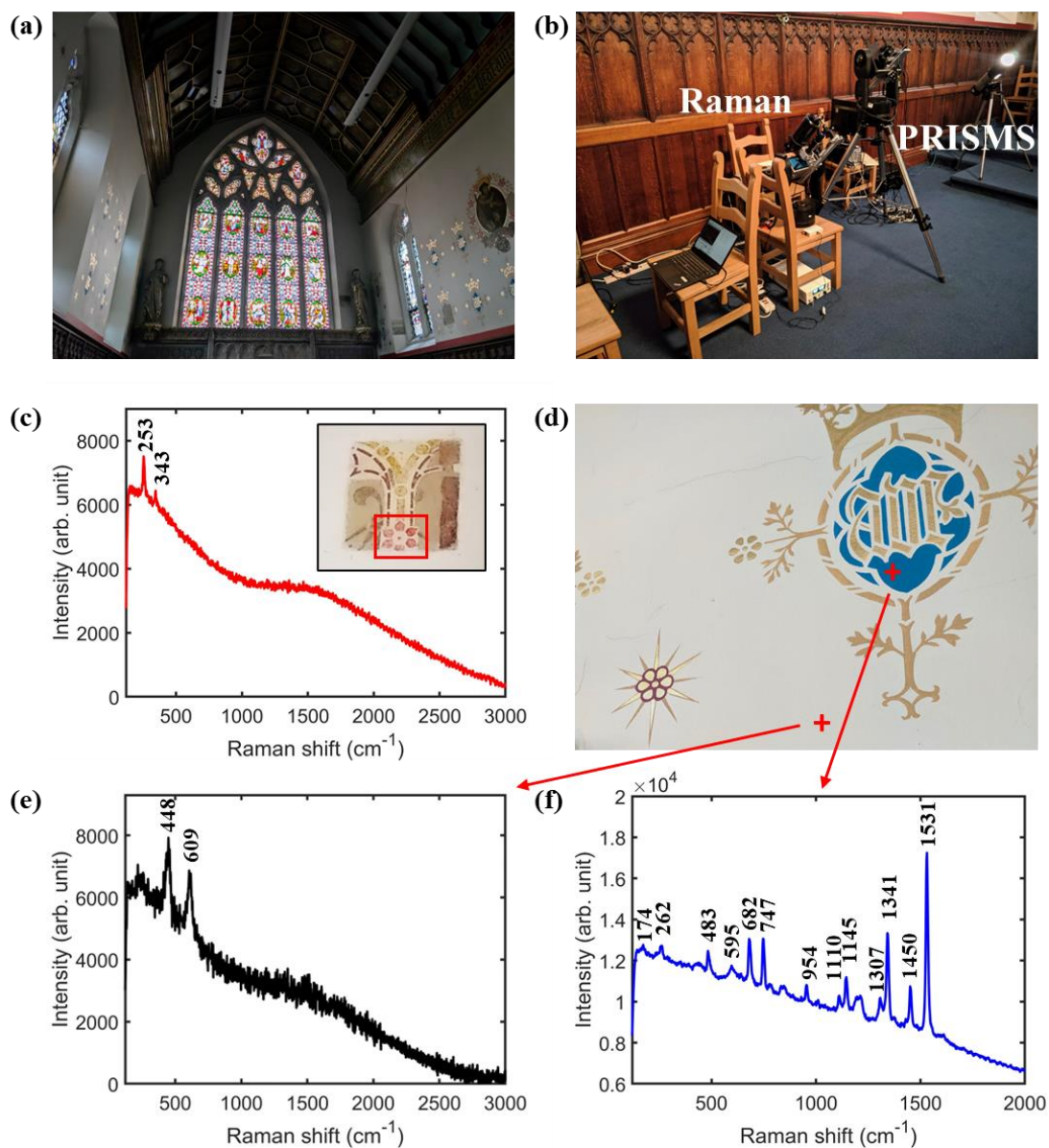


Figure 4.5. Standoff investigation of wall paintings in a chapel of the Convent of Mercy in Nottingham, UK: (a) the full view of the chapel; (b) the mobile Raman system deployed *in situ* next to our remote spectral imaging system PRISMS; (c) Raman spectrum collected on the red petal patterns (see picture in the inset) revealed in the conservation test area where the surface paint had been removed; (d) the surface paint layer where the examined spots in white and blue areas are marked as +; (e) Raman spectrum collected on the white surface paint area; (f) Raman spectrum collected on the blue surface paint area.

4.3. Remote standoff macro-Raman mapping

Raman spectroscopy is a powerful laser technique for the identification of painting materials [107,119]. However, traditional single point analysis cannot meet certain demands in heritage studies, such as investigating large areas of wall paintings. Micro-scale Raman spectral imaging or mapping is widely adopted in other fields such as in biochemistry for the analysis of tissues and cells [150–152]. However, Raman instruments capable of macro mapping are few [39,153,154]. Mounted on a computer-controlled programmable telescope mount, our remote Raman system has the potential of mapping a large area at standoff distances.

Macro Raman mapping is comparable to micro Raman mapping, but with a larger field of view and lower spatial resolution. *In situ* macro mapping is made possible with remote standoff Raman systems. Mapping an area of a wall painting could provide information such as the spatial distribution of different pigments and degradation products, as well as the degree of degradation risks on a macroscopic scale.

4.3.1. Hardware control for scanning

Traditional Raman mapping normally requires a scanning probe or fixed instruments with samples mounted on a motorised stage. For remote Raman mapping on wall paintings, neither is an ideal solution. The whole remote Raman system is mounted on rails atop a computerised alt-azimuth mount and a sturdy tripod. Therefore, to perform Raman mapping, automated moving of the telescope mount is required. The telescope mount is supplied with an AutoStar handset controller, which is used as a data port. Data communication can be established between the computer and the handset using a USB to

RS-232 serial cable. The official Meade telescope software is not suitable for our mission as it mainly focuses on astronomical applications (with a celestial coordinate database embedded) thus cannot work for terrestrial projects like remote Raman mapping. Fortunately, Meade provides a manual of serial commands which makes it possible to write in-house programs for automated scanning [155]. The implementation of remote Raman mapping is controlled by an in-house written program developed within the LabVIEW software package (Figure 4.6). The control program has been developed on the basis of a code library by a former member of our group, Alex Hogg. Thanks to his work, all the serial commands can be used as modules in the LabVIEW diagram.

The slew rate is set to the slowest speed (guiding rate) for accurate movement. The altitude and azimuth coordinates (in the unit of second (of arc)) for each step can be calculated from

$$l_{step} \approx s_{arc} = 2\pi r \cdot \frac{\theta}{360} \quad (4.1)$$

where r is the radius, i.e. the distance between the instrument and the target, which can be acquired by using a laser distance meter for *in situ* analysis.

Therefore the angle for each step is

$$\theta \approx \frac{180}{\pi r} \cdot l_{step} \quad (4.2)$$

Sufficient delay times are given to guarantee that the telescope can slowly and accurately move to target position. Once the target position is reached, the program saves both the calculated and actual position coordinates in log files. Then, the recording of the Raman spectrum with a given acquisition time is triggered. Loops are used to repeat the above

process to achieve Raman mapping. The scanning process starts from the bottom left corner, and moves horizontally towards the bottom right corner (Figure 4.7). When the bottom right corner is reached, the telescope travels back to the starting point at the same azimuth, and then points upwards to the set altitude.

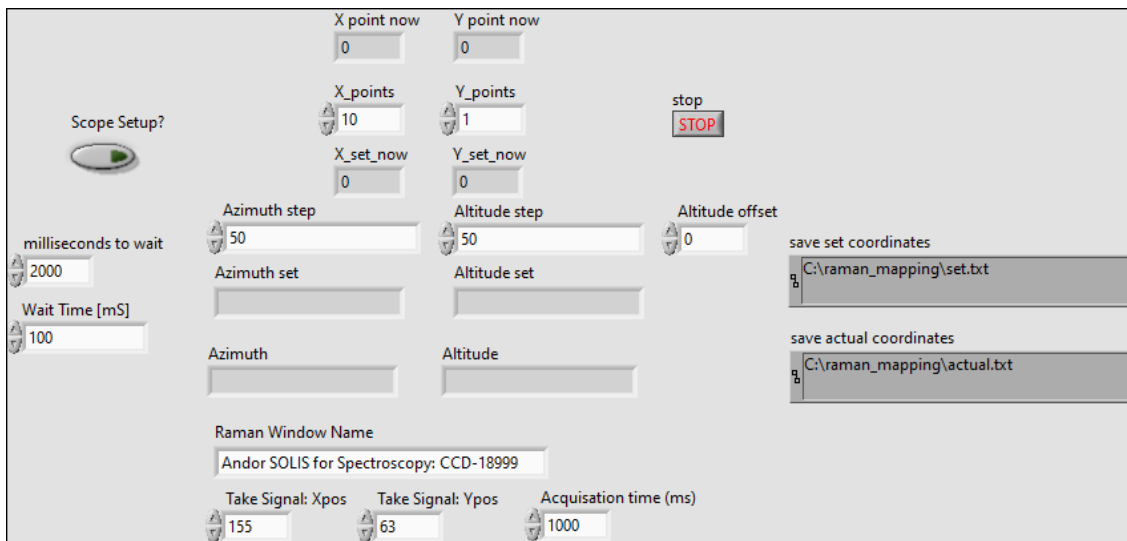


Figure 4.6. Interface of the control program for remote Raman mapping.

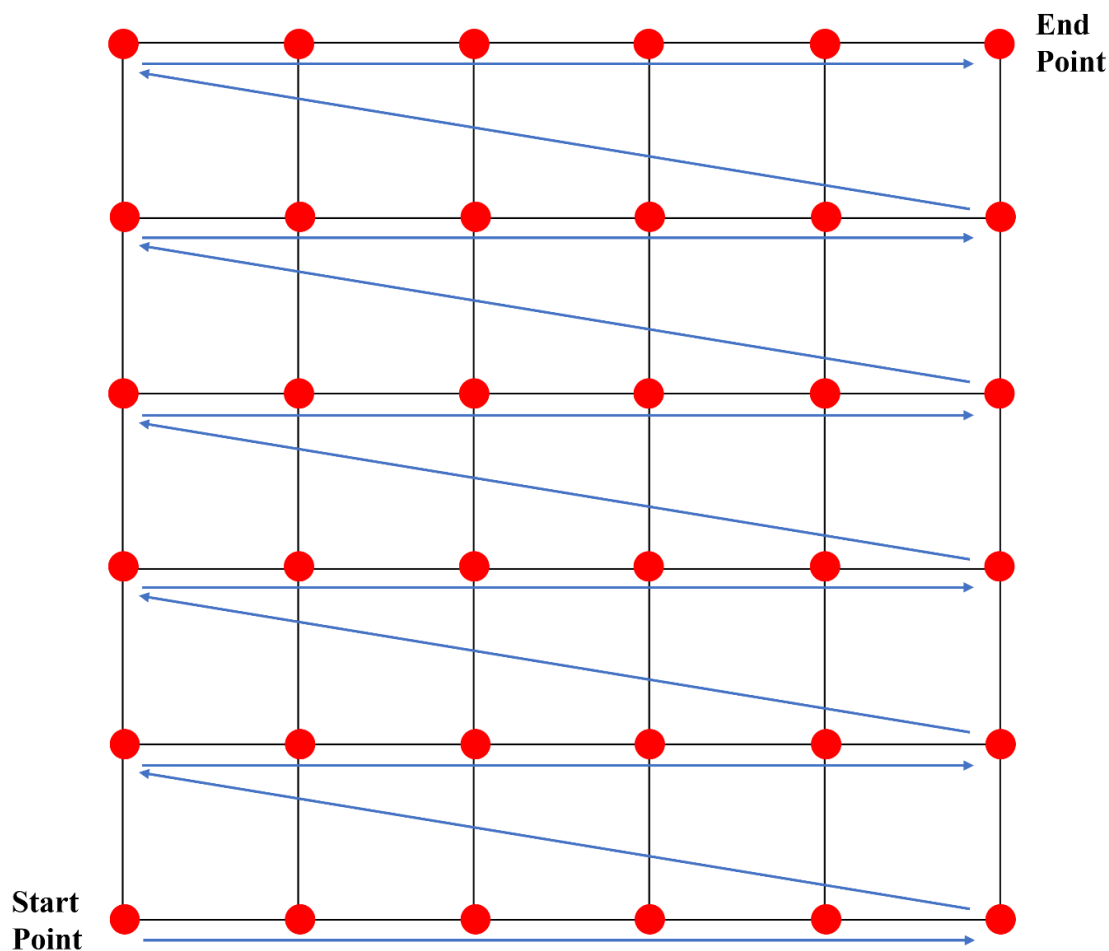


Figure 4.7. Scanning direction of the remote Raman mapping.

4.3.2. Macro-Raman mapping: Wall paintings at the Brighton pavilion

As part of a field campaign in 2019, remote standoff *in situ* macro-Raman mapping was carried out in the Music Room of the Royal Pavilion in Brighton, utilising a suite of non-invasive imaging and spectroscopic techniques provided by the ISAAC mobile lab. King George IV commissioned the construction of the Royal Pavilion. Work on the structure began in 1787, and it was finished in 1815 by the architect John Nash. The music room was designed in the chinoiserie style by Frederick Crace, George IV's chief decorator [156]. The area is covered in murals depicting Chinese landscapes from floor to ceiling. The oil-on-canvas paintings, which were initially stretched and tacked onto the lathe and

plaster walls, were completed in 1820. According to historical records, humidity on the walls caused problems in 1821, and parts of the murals were removed and repaired. The murals were re-hung when the plaster walls were renovated. The murals were packed up by orders from Queen Victoria and sent to London in 1850, which were later returned in 1864, and were directly attached to the plaster walls. The murals in the music room require continual maintenance and restoration. A better understanding of the materials, painting techniques, and treatments would allow for more informed conservation decisions in the future. The chamber has a ceiling height of over 12 m and was traditionally only accessible for examination by scaffolding.

The instrumental setup used *in situ* in the Music Room of the Royal Pavilion in Brighton was the original design which utilised a collimated beam. Section 2.1.2 gives the detailed specifications of the setup. The entire system is mounted on a motorised telescope mount that is controlled by in-house developed software which synchronises the laser beam's motions with the spectral collection. The output beam is collimated with a small divergence, resulting in a spot size of ~ 4 mm on the target at 4 m distance. The maximum laser power at sample is 48 mW, corresponding to an irradiance of 0.38 W/cm^2 .



Figure 4.8. Deployment of the remote standoff Raman system in the Music Room, Royal Pavilion, Brighton.

A small area of 1.2 by 1.2 cm (Figure 4.9a) was chosen for remote standoff macro-Raman mapping at a distance of 4 m. Oil is identified as the binding medium in the mapped area by shortwave infrared (SWIR) (1000–2500 nm) reflectance spectroscopy. Figure 4.9b-f illustrate the Raman maps acquired in this region, as well as representative Raman spectra in spots of three colours. Given that the spot size was roughly 4 mm, the mapping comprised of 25 spectra (5 by 5) throughout the area, ensuring that neighbouring points overlapping with a step size of 2.5 mm. The Raman spectra was acquired at each spot using a 180 s integration time and 2 accumulations to remove cosmic rays. Vermilion was detected by Raman peaks at 252 and 343 cm^{-1} in all red, orange, and yellow areas, despite the presence of fluorescence in the spectral background due to the oil binder. Chrome yellow was found in both yellow and orange zones, with a characteristic Raman band at 841 cm^{-1} . There were no other orange pigments identified. As a result, a mixture of vermilion and chrome yellow is most likely to be the paint for the orange region.

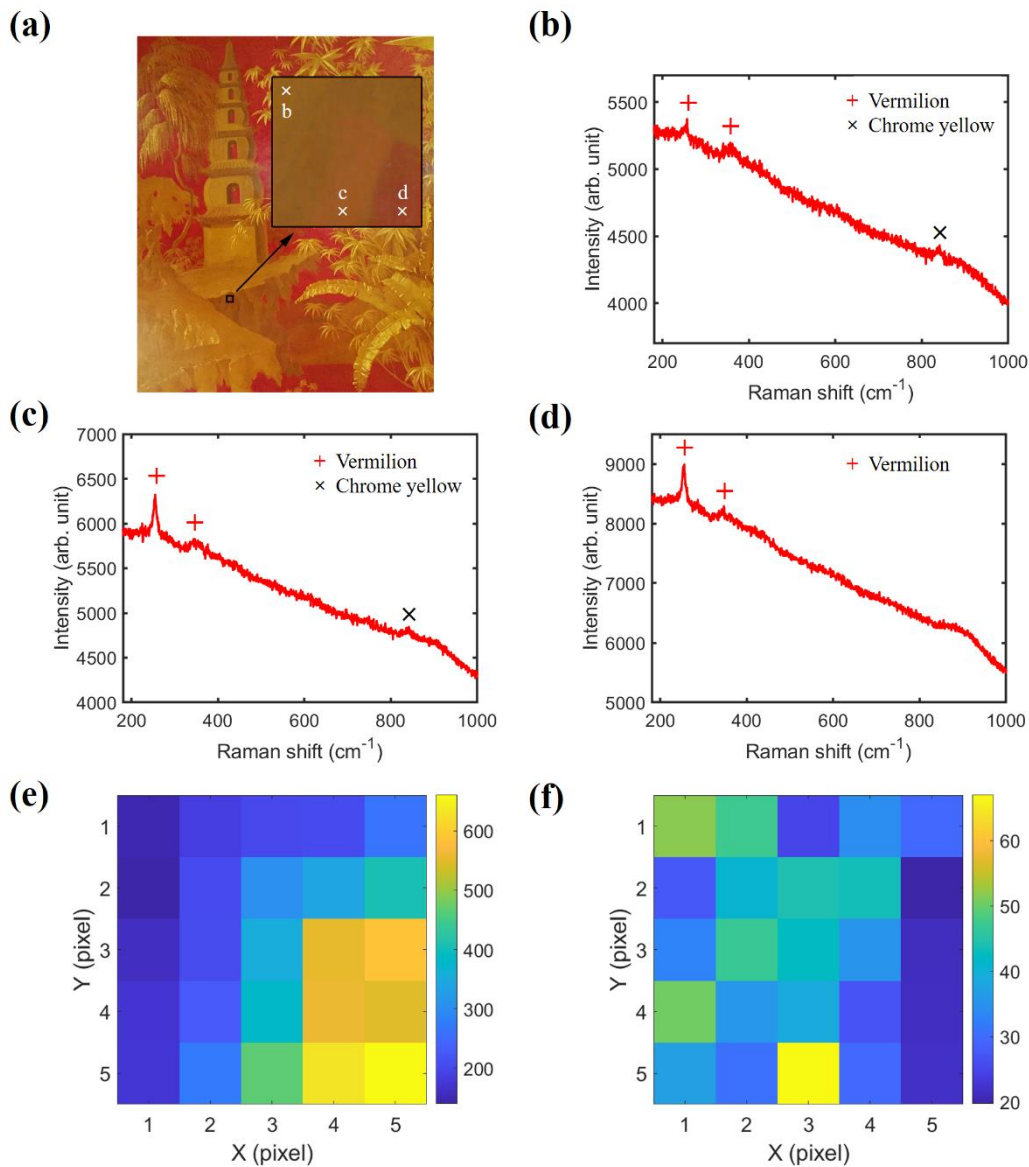


Figure 4.9. (a) A colour image showing the area chosen for remote standoff macro Raman mapping; (b) a typical Raman spectrum representing the yellow area (see position 'b' marked on (a)); (c) a typical Raman spectrum representing the orange area (see position 'c' marked on (a)); (d) a typical Raman spectrum representing the red area (see position 'd' marked on (a)); vermilion peaks are denoted by a +, while signals in chrome yellow are denoted by a x; (e) map for vermilion distribution in the area; (f) map for chrome yellow distribution in the area.

4.4. Standoff *in situ* investigation of salt damage at Fort

Brockhurst

Fort Brockhurst in Gosport, Hampshire, is one of several forts constructed between 1858 and 1862 to safeguard Portsmouth, a crucial operating base for the Royal Navy, from a French invasion. It was designed by Sir William Crossman, an officer in the Royal Engineers. It was decommissioned in 1957 and turned over to civilian use into an English Heritage site, serving as a storage for English Heritage's reserve collections. Its structure remains largely unchanged as the parade ground, gun ramps, moated keep, washrooms, and armoury can all be seen in their original state. Being semi-underground and on the coast, Fort Brockhurst has suffered severe salt damage. The salts in the Fort Brockhurst are present as white, fluffy substance, or yellowish condensed crystals. Figure 4.10 demonstrates different types of salts formed on the walls.

(a)



(b)



(c)



(d)



Figure 4.10. (a) Entrance of the Fort Brockhurst in Gosport, Hampshire. (b-d) Different types of salts formed on the walls of the Fort Brockhurst.

4.4.1. Mock-up experiments in laboratory environment

Before deploying the remote Raman system to Fort Brockhurst, mock up experiments were designed and conducted in the laboratory to verify its sensitivity in discriminating different hydrated forms of salts.

This study focuses on a common type of salts, i.e. the sodium sulfate (Na_2SO_4), which is one of the most dangerous types because of the significant volume expansion between the different states of hydration [157]. Sodium sulfate can be present as anhydrous

Na_2SO_4 and several related hydrates. Thenardite (Na_2SO_4) is the anhydrous and stable phase of sodium sulfate. Mirabilite ($\text{Na}_2\text{SO}_4 \cdot 10\text{H}_2\text{O}$) is the decahydrate of sodium sulfate, also known as Glauber's salt, named after the Dutch/German chemist and apothecary Johann Rudolf Glauber. Mirabilite is unstable and can quickly dehydrate in dry air, the prismatic crystals turning into white powdery thenardite. The process is reversible as thenardite, in turn, absorbs water and transforms into mirabilite. Other hydrated forms of sodium sulfate include sodium sulfate heptahydrate ($\text{Na}_2\text{SO}_4 \cdot 7\text{H}_2\text{O}$), a rare metastable phase of sodium sulfate, which can be formed during the rapid cooling of a solution that is saturated at 40 °C.

Samples were made by dipping the porous fused quartz filter discs in saturated sodium sulfate solution. The fused quartz filter discs made of bonded grains of quartz glass in different porosities can be an ideal medium to simulate the porous natural or artificial building materials for the study of salt behaviours. Then the discs were set up horizontally on the sample stage in room temperature for several hours, simulating the natural drying process of salts in the wall. The remote Raman system was at 3.8 m distance. Raman measurements were performed every 10 min for 160 min (every 5 min after 110 min), with 60 s integration time (20 s for each measurement, averaged 3 times) for each spectrum (Figure 4.11).

Strong Na_2SO_4 signal for solution was detected at 982.6 cm^{-1} , which agreed well with the reference data at 981.9 cm^{-1} . The peak shifted towards higher wavenumber afterwards. The first Raman spectrum collected on the salt-soaked disc revealed a Raman peak at 986.1 cm^{-1} , a value between Na_2SO_4 in solution and mirabilite (989.3 cm^{-1}), suggesting the co-existence of both phases. It was observed that crystals started to form even before the experiments began because of the saturated solution, resulting in the peak shift towards mirabilite. The next spectrum demonstrated a peak at 988.0 cm^{-1} , which is closer

to mirabilite, suggesting that the transition towards mirabilite continued. During 10–100 min, the peak position fluctuated at 988.0–991.8 cm^{-1} , confirming that the majority of the crystals were present as mirabilite. During 100–160 min, the signal kept shifting towards higher wavenumber to $\sim 993.7 \text{ cm}^{-1}$, corresponding to the emergence of thenardite (mean peak at 993.1 cm^{-1}), the anhydrous and stable phase. The environmental temperature and humidity were recorded during the experiment (Table 4.1). Both the room temperature and relative humidity remained relatively stable. Temperature fluctuated at 20.8–21.6 $^{\circ}\text{C}$, while the humidity was kept at 37–39% level. In such a stable condition, thenardite was formed in the end, with no mirabilite remained. According to literature, deliquescence humidity of thenardite is 86.6% at 20 $^{\circ}\text{C}$ [157].

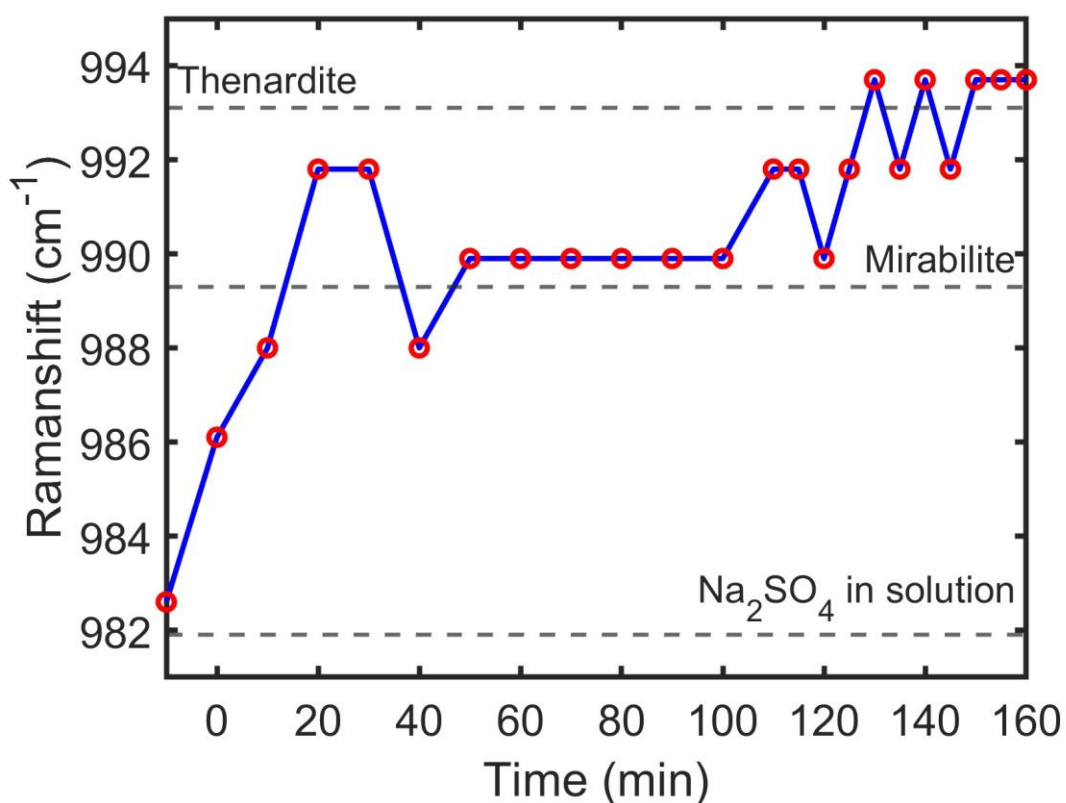


Figure 4.11. Time evolution of positions of the strongest Raman peak of sodium sulfate.

Table 4.1. Temperature and humidity records for mock-up salt monitoring in laboratory environment.

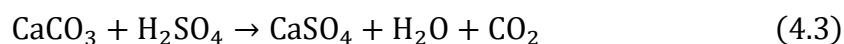
Measurement	Time	Room temperature (°C)	Relative humidity (%)
1	14:45	20.8	39
2	14:55	20.8	39
3	15:05	21	39
4	15:15	21	38
5	15:25	21.2	38
6	15:35	21.3	38
7	15:45	21.2	37
8	15:55	21.4	37
9	16:05	21.1	37
10	16:15	21.1	37
11	16:25	21.2	37
12	16:35	21.2	37
13	16:40	21.1	37
14	16:45	21.2	37
15	16:50	21.4	37
16	16:55	21.6	37
17	17:00	21.5	37
18	17:05	21.4	37
19	17:10	21.3	37
20	17:15	21.2	37
21	17:20	21.4	37
22	17:25	21.2	37

4.4.2. *In situ* analysis of salts in Fort Brockhurst

The instrumental setup used in Fort Brockhurst was an updated design, employing a beam expander that allowed for a focused beam (1 mm in diameter). Temperature and humidity were recorded during the measurements. It was found that both could change quickly, which made the situation more complex as different states of salts could form and co-exist.

In Bay 7, the first measurement was carried out at the white area on the ceiling (spot 1). Two types of calcium-based materials, chalk (CaCO_3) and gypsum ($\text{CaSO}_4 \cdot 2\text{H}_2\text{O}$) were identified. Two peaks at 1088 and 280 cm^{-1} agreed well with the Raman reference of

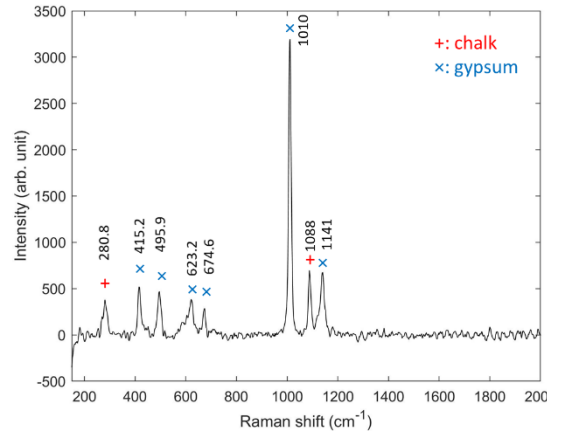
chalk, while multiple signals of gypsum at 1010, 1141, 415.2, 495.9, 623.2, and 674.6 cm^{-1} were present. Chalk could be the main component of the whitewash since it is a common white pigment. However, the role of gypsum can be interpreted in a variety of ways. Gypsum is also a widely used white pigment, and its mixed use with chalk was not uncommon. It could serve as an extender, filler or adulterant in paintings as well [158]. It can also be a major component of mortars, plasters and some building stones, hence an integral part of the building fabric [159]. On the other hand, gypsum is an important salt in the deterioration of building materials and, especially, wall paintings. The sulfur oxides (SO_x) in the air can convert to sulfuric acid (H_2SO_4) in the presence of moisture. The reaction of sulfuric acid with chalk in the whitewash leads to the formation of anhydrite which can then convert to gypsum [160,161]:



At a middle part of the wall (spot 2) and another area on the ceiling (spot 3), sharp peaks at 990.9 cm^{-1} and 989.9 cm^{-1} , respectively, were detected. It is known from the mock up experiments that the drying process of sodium sulfate from the solution (main peak at 981.9 cm^{-1}) is to form mirabilite (main peak at 989.3 cm^{-1}), and eventually to anhydrous thenardite (main peak at 993.1 cm^{-1}). The peak positions of the salts at the two measured spots suggest that they were at the early stage of the transition from mirabilite to thenardite. From the records during the measurements, the temperature and humidity change could be volatile. The temperature could drop by >5 $^\circ\text{C}$ within 50 min while the relative humidity increased by $>30\%$ at the same time (Table 4.2). Therefore, the direction of the transition might change accordingly.



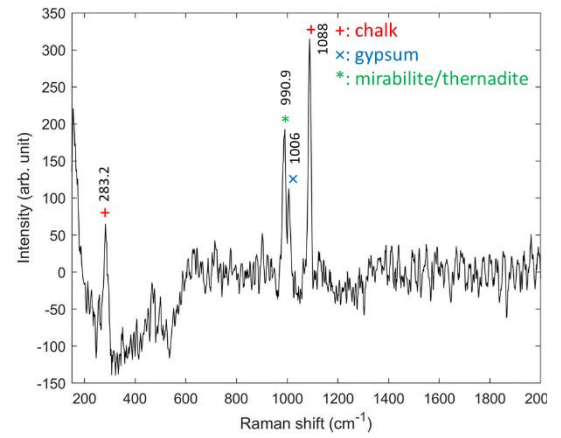
Bay 7 – spot 1



Bay 7 – spot 1



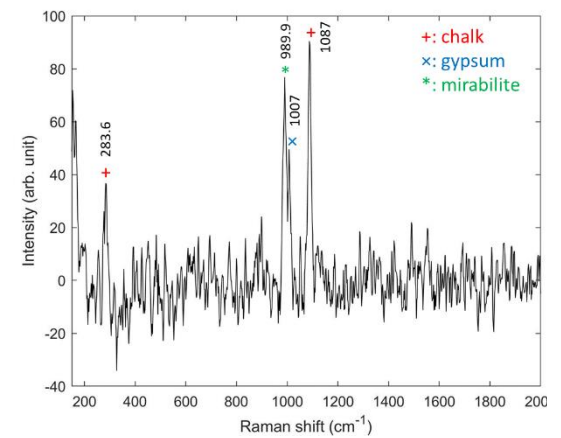
Bay 7 – spot 2



Bay 7 – spot 2



Bay 7 – spot 3



Bay 7 – spot 3

Figure 4.12. Raman measurements of salts at the Bay 7.

Table 4.2. Temperature and humidity records in Bay 7.

Location:	Bay 7		
Date:	18/02/2020		
Room temperature (°C)	Relative humidity (%)	Time	
16.0	42	11:10:00	
14.2	54	11:15:00	
12.1	61	11:20:00	
11.5	74	11:35:00	
11.2	72	11:45:00	
10.5	75	12:00:00	
10.5	76	12:15:00	
10.4	77	12:30:00	
12.0	74	13:00:00	
12.6	70	13:15:00	
12.8	70	13:30:00	
13.5	69	13:40:00	
13.9	68	13:45:00	
14.1	66	14:00:00	
13.9	67	14:15:00	
13.0	70	14:30:00	
13.5	68	14:37:00	
13.6	67	14:45:00	
13.9	68	15:00:00	
13.1	69	15:15:00	
13.4	69	15:20:00	
13.7	68	15:25:00	
13.8	68	15:30:00	
14.0	67	15:45:00	
14.1	67	16:00:00	
13.8	69	16:15:00	
14.0	67	16:30:00	
14.5	67	16:45:00	
13.2	70	17:00:00	
13.9	68	17:15:00	

In Bay 1, sharp peaks at 991.7 cm^{-1} for all three analysed spots suggested an intermediate state between mirabilite and thenardite. More information could be revealed by the weak peaks. For example, a peak at 446.6 cm^{-1} indicated that it was more likely to be mirabilite (reference: 446.7 cm^{-1}) rather than thenardite (reference: 451.8 cm^{-1}). The temperature was down to $10\text{ }^{\circ}\text{C}$, while the relative humidity was as high as 90% (Table 4.3). It is likely that under such circumstances, thenardite could convert to mirabilite. According to literature, deliquescence humidity of thenardite is 85.6% at $10\text{ }^{\circ}\text{C}$ [157].

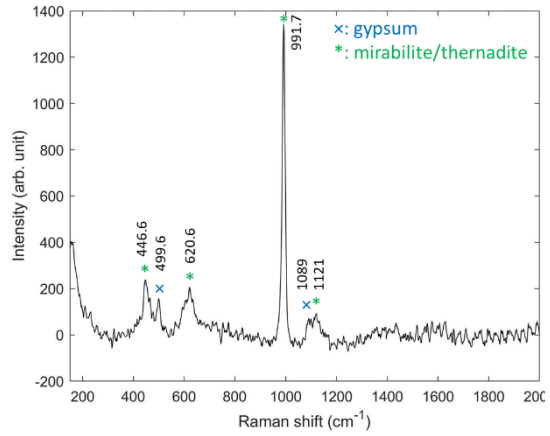
Table 4.3. Temperature and humidity records in Bay 1.

Location:	Bay 1
Date:	19/02/2020

Room temperature ($^{\circ}\text{C}$)	Relative humidity (%)	Time
11.7	76	11:20:00
11.5	77	11:22:00
11.2	78	11:23:00
11.0	79	11:25:00
10.8	79	11:27:00
10.3	82	11:42:00
10.2	82	11:47:00
10.9	84	13:00:00
10.3	87	13:10:00
10.1	89	14:00:00
10.1	90	14:15:00
10.1	90	14:30:00
10.1	90	14:45:00



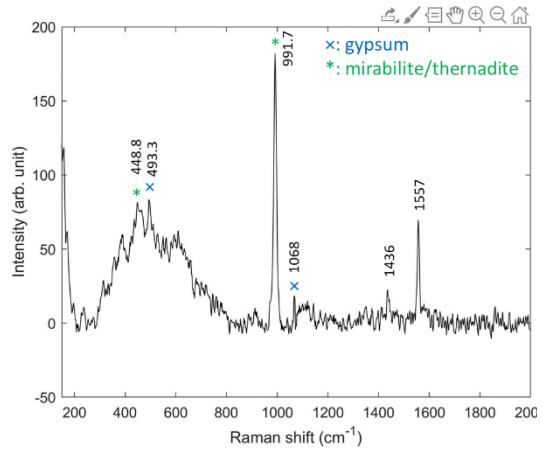
Bay 1 – spot 1



Bay 1 – spot 1



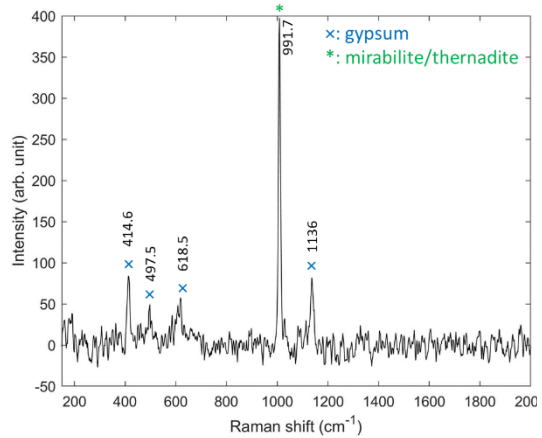
Bay 1 – spot 2



Bay 1 – spot 2



Bay 1 – spot 3



Bay 1 – spot 3

Figure 4.13. Raman measurements of salts at the Bay 1.

In Bay 8, a spot at the lower part of the wall revealed a peak at 992.4 cm⁻¹, very close to the thernadite reference at 993.1 cm⁻¹. The temperature was 10–11 °C, while the relative humidity was 82–86% (Table 4.4).

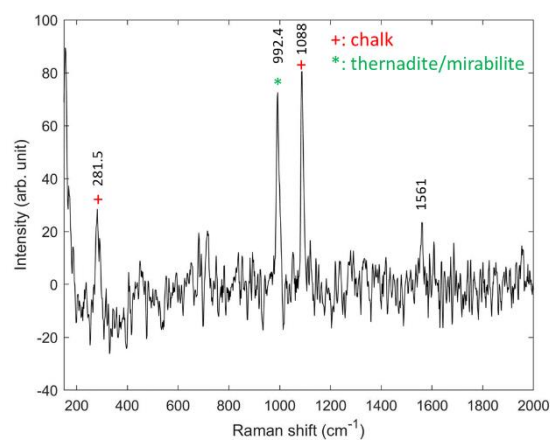
Table 4.4. Temperature and humidity records in Bay 8.

Location:	Bay 8
Date:	20/02/2020

Room temperature (°C)	Relative humidity (%)	Time
10.5	86	08:30:00
10.6	86	08:45:00
10.7	86	09:00:00
10.7	86	09:30:00
10.8	86	09:45:00
10.8	86	10:00:00
11.0	82	12:45:00



Bay 8 – spot 1



Bay 8 – spot 1

Figure 4.14. Raman measurements of salts at the Bay 8.

In addition to a series of point analyses on the salts at the Fort Brockhurst, a large area Raman mapping was carried out to study the salt distribution on the wall. From the previous mock up tests in the laboratory, our remote Raman system is capable of

distinguishing different forms and phases of salt materials. A large area investigation would help better understand the intricate formation and transition mechanisms of salts. The area of interest was chosen on a white wall in Bay 8. An area of 40 by 40 cm was chosen for macro-Raman mapping at a distance of 4.2 m (Figure 4.15). Figure 4.16 shows the Raman maps acquired in this location, as well as representative Raman spectra exhibiting the identified materials. Within the area, 25 spectra (5 by 5) were collected, with a step size of 10 cm. Positions of all the spots were recorded in a video during the scanning. The Raman spectra were acquired at each spot using a 40-second integration time and 3 accumulations for cosmic ray removal, accounting for 120 s for each measurement. The temperature and humidity were recorded during the mapping, as shown in Table 4.4.

In all the spectra, a sharp peak at 1088 cm^{-1} was detected as well as several weak peaks at 155, 281, and 711 cm^{-1} , which all correspond to chalk (CaCO_3). Gypsum was not identified. Therefore chalk is most likely the main whitewash material for the wall, and gypsum is not part of the original composition. In certain areas, signals at $990\text{--}992\text{ cm}^{-1}$ were identified as an intermediate state between mirabilite ($\text{Na}_2\text{SO}_4 \cdot 10\text{H}_2\text{O}$) and thernadite (Na_2SO_4). Distributions of chalk and mirabilite/thernadite can be visualised by plotting the net counts of corresponding signals in Raman spectra. Compared with the photos taken at the same area, it is revealed that the sodium sulfate salts mostly accumulated at the top left corner where salt grains were present, rather than the area where the fluffy substance emerged. The Raman intensity difference might come from the density difference between the two forms of salts.

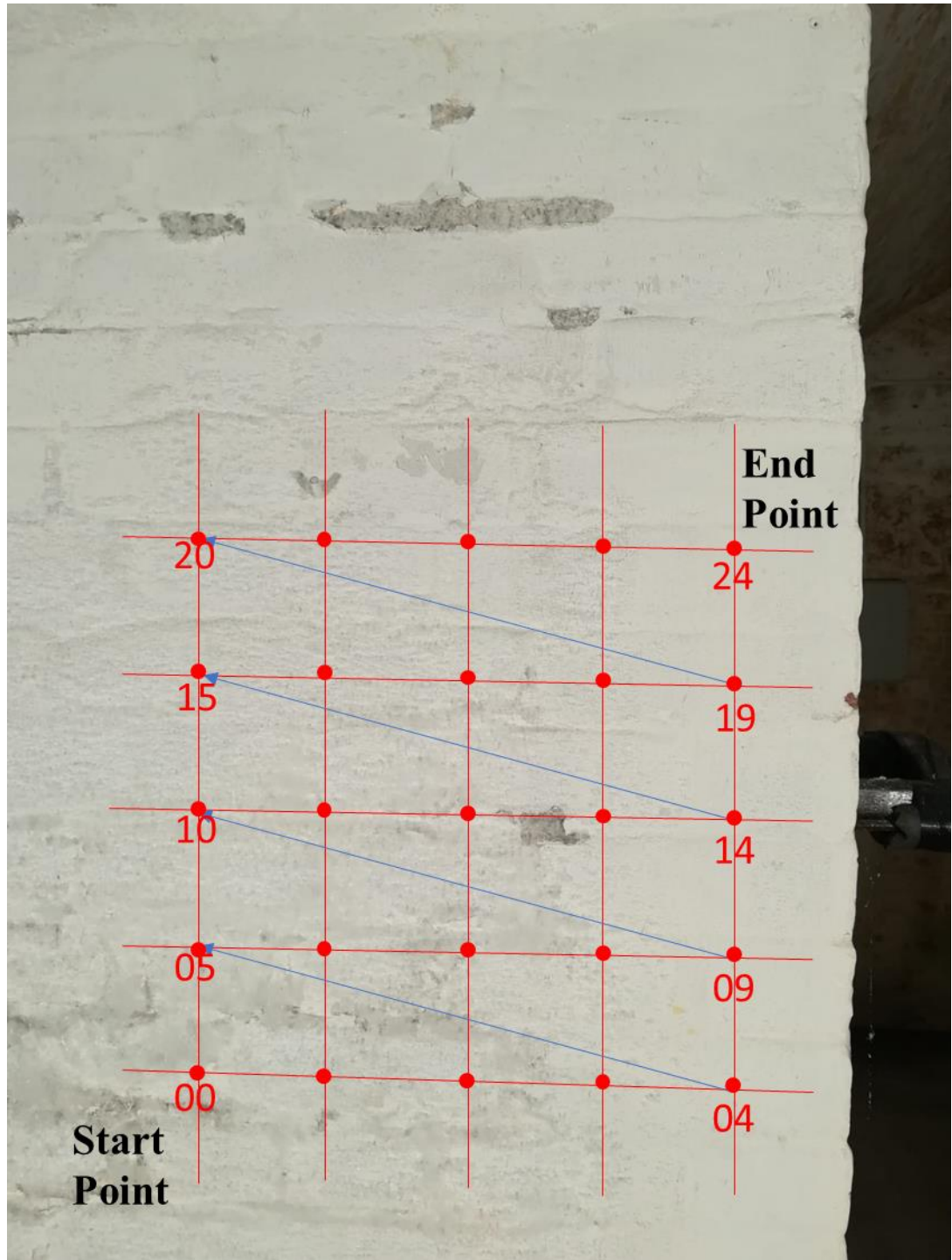
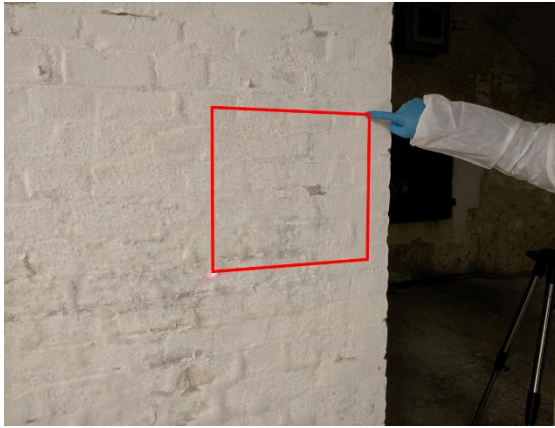
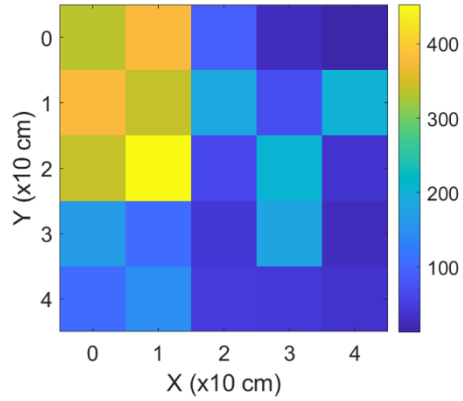


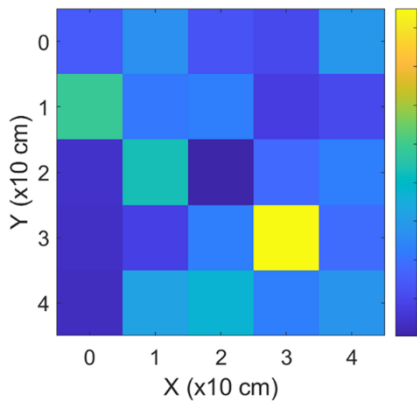
Figure 4.15. Scanned area of the remote Raman mapping at Fort Brockhurst.



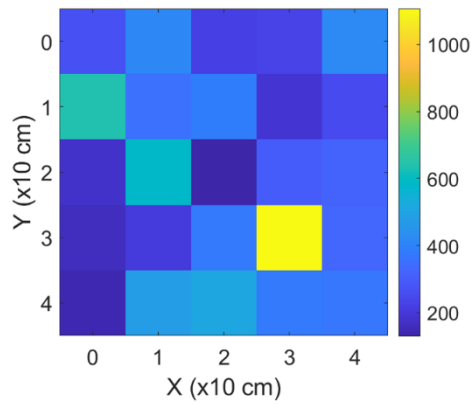
Mapped area



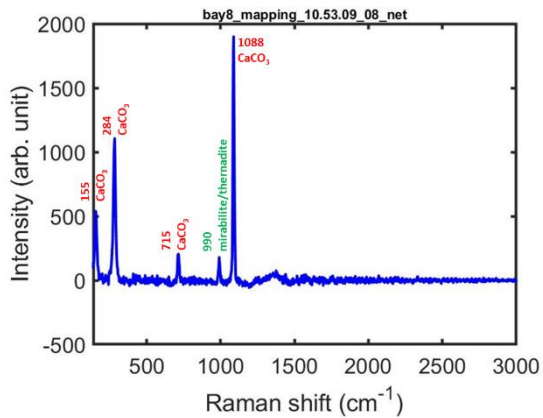
Distribution of mirabilite/thernadite



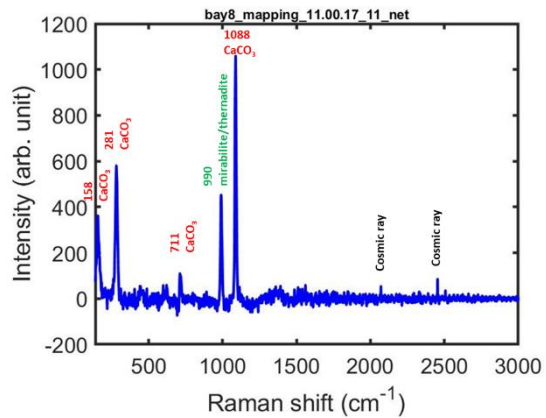
Distribution of chalk
(main Raman peak)



Distribution of chalk
(second strongest Raman peak)



Spot #08



Spot #11

Figure 4.16. Remote macro Raman mapping of salts at the Fort Brockhurst and representative spectra as numbered in Figure 4.15.

4.5. Conclusions

The remote standoff Raman system was successfully applied in a field campaign for the *in situ* analysis of wall paintings in the Cathedral Church of St Barnabas in Nottingham to identify the pigments used in the Blessed Sacrament Chapel in order to date the painting scheme and hence verify its attribution to the renowned architect Augustus Welby Pugin.

The *in situ* remote standoff Raman analysis was then conducted on wall paintings in a chapel of the Convent of Mercy in Nottingham designed also by Augustus Welby Pugin. The identification of traditional and modern pigments at different layers gives a better understanding of the history of the wall paintings to inform future conservation planning.

The remote standoff Raman spectroscopy system is demonstrated to be able to perform remote macro Raman mapping from a distance of 3–15 m for cultural heritage research.

The *in situ* remote macro Raman mapping was successfully conducted on a chinoiserie mural at the Royal Pavilion, Brighton. The spatial distribution of the identified pigments can help art conservators in better understanding the original painting technique and process.

The *in situ* remote macro Raman mapping with a focused laser beam was also performed for salt damage investigation in Fort Brockhurst. Point analyses effectively identified different types of salts. Distribution of salts in a large area can be revealed, which enables the further study of salt formation and transition mechanisms with temperature and humidity changes and helps better understanding of the salt damage mechanism for buildings.

Chapter 5

Remote standoff depth-resolved multimodal spectroscopic analysis

5.1. Introduction

Wall paintings are usually complex heterogeneous systems featuring a multilayer structure. The painting process typically involves successive applications of plaster, preparatory, ground, and paint layers to the support. The study of the paint stratigraphy can provide information about the painting skills, bringing insights into historical contexts and artist-specific techniques, which can inform decision-making processes for future conservation work.

Instrumental innovations in the past few decades have contributed to the transition of many analytical methods from the research laboratory to the real world. Compact portable and mobile instruments nowadays allow heritage objects to be examined *in situ*. Unfortunately, there is an absence of modalities to provide depth information with layer by layer material identification, which is crucial for understanding the wall painting stratigraphy. Optical coherence tomography (OCT) is a non-invasive imaging modality that provides real-time 3D volumetric images in depth [124]. However, it cannot give chemical information. X-ray fluorescence (XRF) spectroscopy is arguably the most widely adopted approach for *in situ* elemental analysis. XRF signals are collected from the bulk, which makes depth-resolved analysis difficult. Spatially offset Raman spectroscopy (SORS) is a novel approach which can interrogate subsurface molecular composition of turbid materials noninvasively [162]. It seems not capable to give accurate

depth information without external calibration. For other conventional non-invasive techniques, most are either not suitable for *in situ* analysis or tend not to be able to give depth information.

Laser-induced breakdown spectroscopy (LIBS) can be an ideal option for *in situ* elemental analysis. Being micro-destructive, a unique capability of LIBS is to ablate the material while revealing its elemental composition, which enables the collection of other information at different depths between the laser pulses when combined with other modalities. For instance, the synergy between LIBS and Raman spectroscopy can offer complementary material information about the sample: Raman spectroscopy uses molecular fingerprints to identify materials, while LIBS reveals elemental compositions, including contents of trace and minor elements [90]. The integration could include other modalities such as reflectance spectroscopy and fluorescence spectroscopy.

In cultural heritage studies, the integrated use of LIBS and other techniques (e.g. OCT, XRF, and reflectance spectroscopy) for depth-resolved analysis have been reported [64,65]. Among them, the most promising combined depth-resolved method is the LIBS + Raman hybrid working at close range, which has been applied to the analysis of various heritage objects [66,94,163–165]. Several research groups have been working on the development of a single benchtop or mobile apparatus that combines Raman spectroscopy, LIBS, and laser-induced fluorescence (LIF) [101,102,104]. However, to date no combined use of LIBS and other methods in a remote/standoff manner for depth-resolved analysis in heritage research has been reported.

In this chapter, a multimodal approach consisting of standoff LIBS, Raman and reflectance spectroscopy working in the range of 3–15 m for wall painting studies is presented. The capability of this system to perform standoff *in situ* depth-resolved

material identification of multilayer wall paintings has been demonstrated for the first time both in laboratory environment and in a field campaign (*in situ*) on whitewashed wall paintings of the Unity Chapel in the Cathedral Church of St Barnabas in Nottingham, UK. The multimodal information provided by standoff LIBS, Raman spectroscopy and reflectance spectroscopy enables the characterisation of the wall painting stratigraphy.

5.2. Remote standoff spectroscopy system for multimodal analysis

Following our development of a remote standoff Raman spectroscopy system with typical working distances of 10 m for material analysis at historical sites including wall paintings and large monuments [112], the system has been adopted as one of the Mobile Lab facilities on offer as part of the European Research Infrastructure for Heritage Science in the framework of the EU funded project IPERION HS. The development of a remote LIBS system could enrich our arsenal of a range of remote spectroscopy techniques and facilitate a remote multimodal approach for depth-resolved analysis. When assisted with our in-house developed remote spectral imaging system, PRISMS [11], the integrated system will have enhanced power to collect depth-resolved multimodal information containing elemental, molecular and reflectance results simultaneously at remote distances. The combined data can be interpreted self-consistently, allowing us to solve heritage research problems with a holistic perspective.

The schematic diagram of the hybrid remote standoff spectroscopy system consisting of LIBS, Raman spectroscopy, and reflectance spectroscopy is presented in Figure 5.1. The design of our system is giving priority to the actual demands for *in situ* analysis of heritage objects. Different from most of LIBS-Raman hybrid systems that utilise a single pulsed

laser for excitation for the sake of being compact, our system employs two laser sources, 780 nm continuous-wave (CW) and 1064 nm pulsed, for Raman spectroscopy and LIBS, respectively. Details of the Raman and LIBS setups are given in Section 2.1.6 and 2.2.2, respectively.

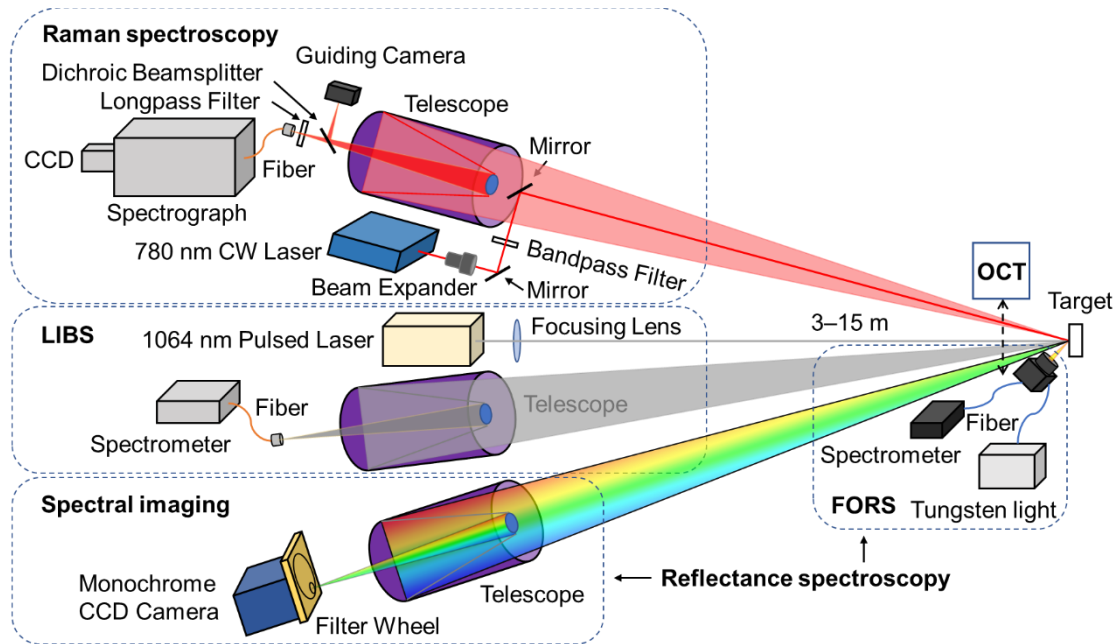


Figure 5.1. Schematic diagram of the hybrid remote standoff spectroscopy system consisting of LIBS, Raman spectroscopy, and reflectance spectroscopy. OCT is used in laboratory tests to monitor the formation of the crater by laser pulses during the LIBS analysis.

Regarding the detection system, the issues of using a single spectrometer for LIBS and Raman arise from different spectral ranges required for both techniques. Raman spectra usually covers a wavelength range of $\sim 100\text{--}300$ nm starting from the Rayleigh line, while typical LIBS signals emerge at a fixed yet much broader region at $\sim 200\text{--}850$ nm. There are other problems such as spectral sensitivity (sensor response) at different wavelength regions. Therefore, separate spectrometers with different detectors best suited for both techniques are used. For Raman spectroscopy, the reflected light passes through the longpass filter to remove the Rayleigh line and is then sent to a spectrograph (Andor

Shamrock 193i) coupled to a cooled (-70 °C) CCD detector (Andor iDus 416) by a fibre. The spectral resolution is $\sim 4 \text{ cm}^{-1}$ over the spectral range of 140–1300 cm^{-1} when recorded with a 1200 l/mm grating, or $\sim 8.5 \text{ cm}^{-1}$ over 140–3300 cm^{-1} with a 500 l/mm grating. Designed in an oblique geometry, a telescope is used for collecting the emitted light for LIBS. An optical fibre with a core diameter of 600 μm is attached to the rear port of the telescope to send the signals to the spectrometer. In laboratory evaluations, a 4-channel spectrometer system (Avantes AvaSpec-ULS2048CL-EVO) is adopted, which jointly covers a spectral range of 200–945 nm with resolution of 0.10–0.18 nm for 200–524 nm achieved by 1800 l/mm gratings (ch1&2), and 0.20–0.28 nm for 522–945 nm achieved by 1200 l/mm gratings (ch3&4), respectively. For *in situ* analysis, a compact Avantes AvaSpec-ULS2048CL spectrometer is used, which is configured for 364–925 nm with a spectral resolution of $\sim 0.5 \text{ nm}$ over the spectral range recorded with a 600 l/mm grating. The detector is a CMOS with 2048 linear pixels having dimensions of 14 $\mu\text{m} \times 200 \mu\text{m}$. Another telescope equipped with a guide camera is employed to help remotely align the laser beam as well as the telescope for collection and record the position where the LIBS measurement is performed.

Reflectance spectroscopy can be achieved remotely by our in-house developed remote standoff spectral imaging system, PRISMS, which consists of the same telescope as the remote standoff LIBS and Raman setups, a filter wheel with 10 spectral bands of bandwidth 40 nm with central wavelengths at 50 nm intervals from 400 nm to 850 nm, and a Jenoptic coolpix CCD camera [11]. The system typically operates at distances of 3–30 m. Depending on the availability of instruments, a conventional fibre optic reflectance spectroscopy (FORS) system can also be used as a substitute for the remote PRISMS system. Details of the FORS setup is given in Section 3.4.

Daylight subtraction is carried out for Raman spectra by subtracting two consecutive spectra (one with laser on and the other with laser off), which are recorded with the same integration time (1 s), and then combining all background subtracted spectra for multiple cycles. Second order polynomial fittings are performed to 13 known spectral lines from a mercury argon calibration light source (Ocean Optics HG-1) between 790 and 970 nm to establish the wavelength calibration of the laser and Raman signals. The baseline subtraction is conducted by smoothing the spectrum using a moving median filter, which is efficient in removing fluorescence and instrument related broad spectral features which we would want to retain to subtract from the original Raman spectrum such that only Raman peaks remain. Alternatively, manual subtraction can be performed using a polynomial fitting in user-defined regions of interest for more complicated situations.

LIBS measurements are done in time-integrated mode to capture the entire process of emission signals. It is worth noting that wavelengths below ~ 380 nm are cut off due to UV absorption by the aberration correction glass plate at the aperture of the telescope. An in-house written program for automated line assignments has been developed within the MATLAB software package, using LIBS spectral line references from NIST atomic spectral database [122], complemented by a table of major analytical emission lines of elements by D. Anglos et al. [123]. Background subtraction is then performed so that net counts for emission lines could be calculated.

To monitor the formation of the crater by laser pulses, a spectral domain optical coherence tomography (SD-OCT) imaging system (Thorlabs CALLISTO) at 930 nm was set up at close range for laboratory evaluation. The system provides an axial resolution of $4.5 \mu\text{m}$ in paint (assuming a refractive index of 1.5) and a transverse resolution of $9 \mu\text{m}$. OCT images were captured in high resolution (500×512 pixels) with the pixel size of $10 \times 3.1 \mu\text{m}$ in width and depth respectively. A motorised linear translation stage was employed

to mount the OCT probe, preventing it from obstructing the operation of remote/standoff instruments.

5.3. Laboratory evaluation of remote standoff multimodal spectral analysis

Prior to the *in situ* application of our hybrid remote standoff spectroscopy system in heritage sites, the standoff multimodal analysis was performed in the laboratory to evaluate the multi-analytical approach for the depth-resolved material identification of wall paintings, using a multilayer mock-up paint sample. It was painted on a plywood board (P.E.R. Belle Arti, Italy) covered by a white preparation layer. Rutile (TiO_2) and chalk (CaCO_3) had been identified by Raman spectroscopy at the surface of the white substrate. From bottom to top, gypsum, vermilion, Prussian blue mixed with lithopone, and calcite paint layers were applied successively, as shown in Figure 5.2. All of the layers were painted one year prior to this study. Oil was used as the binding medium for all the paint layers except for gypsum, which was applied to the substrate with water.

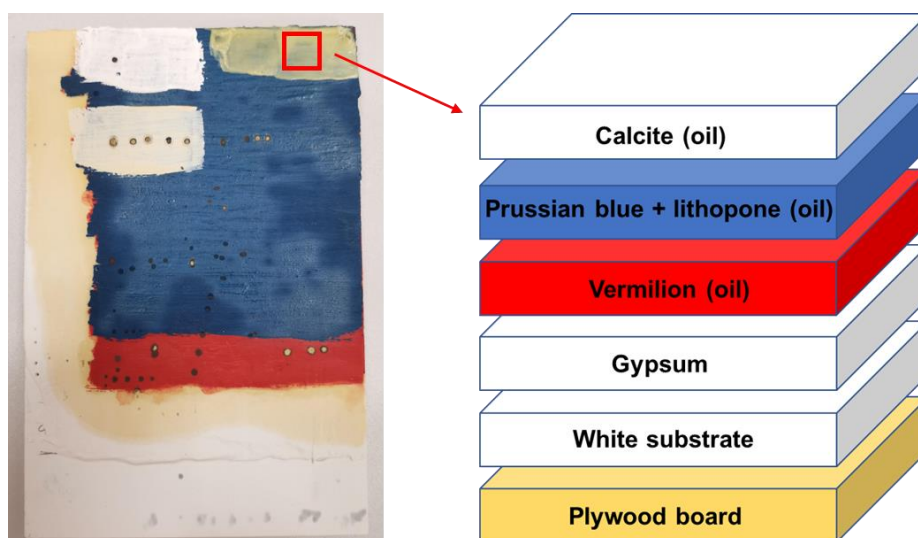


Figure 5.2. Layer structure of the mock-up paint sample.

The multilayer mock-up paint sample was mounted vertically at a distance of 5.6 m from the standoff multimodal system where LIBS, Raman spectroscopy, and spectral imaging systems were set up abreast in an oblique geometry (Figure 5.1). Assisted with OCT, the examined area was selected with relatively flat and smooth surface. Laser beams for both LIBS and Raman spectroscopy were focused to ~1 mm in diameter and guided to the same spot on the sample surface. PRISMS allowed the extraction of spectral imaging data from a small area, providing reflectance information where the ablation crater was formed. OCT was employed at close range to further examine the morphology of the crater. For multimodal analysis, non-invasive measurements were performed before LIBS in each cycle, in a sequence of Raman spectroscopy, OCT, reflectance spectroscopy, and LIBS. A holistic multimodal approach was adopted in data interpretation. For each laser pulse, data acquired from non-invasive techniques just before LIBS could be integrated to provide more consistent, accurate, and comprehensive information. Images reconstructed by PRISMS could give visual evidence of the ablation process, where colours of underlayers could be revealed at the edge of the crater. More importantly, reflectance information can be extracted from any single pixel in the image, offering another method for material identification. Reflectance spectra are compared with reference curves of standard materials. Kubelka-Munk (KM) modelling is adopted for cases where multiple painting materials might be applied [118,166]. To monitor the formation of the ablation crater, OCT virtual cross-section images were collected in a 5 mm line centred at the crater.

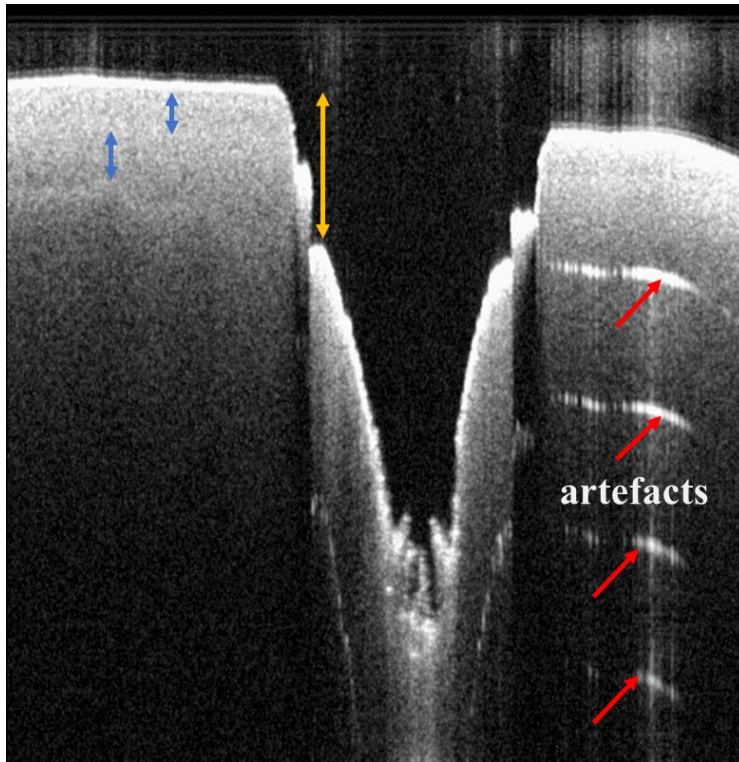


Figure 5.3. The ablation crater formed after 100 laser pulses. The red arrows indicate the artefacts. The yellow arrow marks all the paint layers. Two blue arrows show that the calcite layer was stratified.

In the first cycle (as shown in Figure 5.4), the reflectance spectrum obtained from the surface agreed well with calcite. Consistently, strong Raman signals of calcite at 1086 and 280 cm^{-1} were present, along with peaks corresponding to linseed oil at 1442 and 1304 cm^{-1} [167]. The 1st laser pulse for LIBS did not produce sufficient plasma because of the rough surface as well as the dust on it. Therefore, emission signals were weak.

Layer 1 (shot #001)

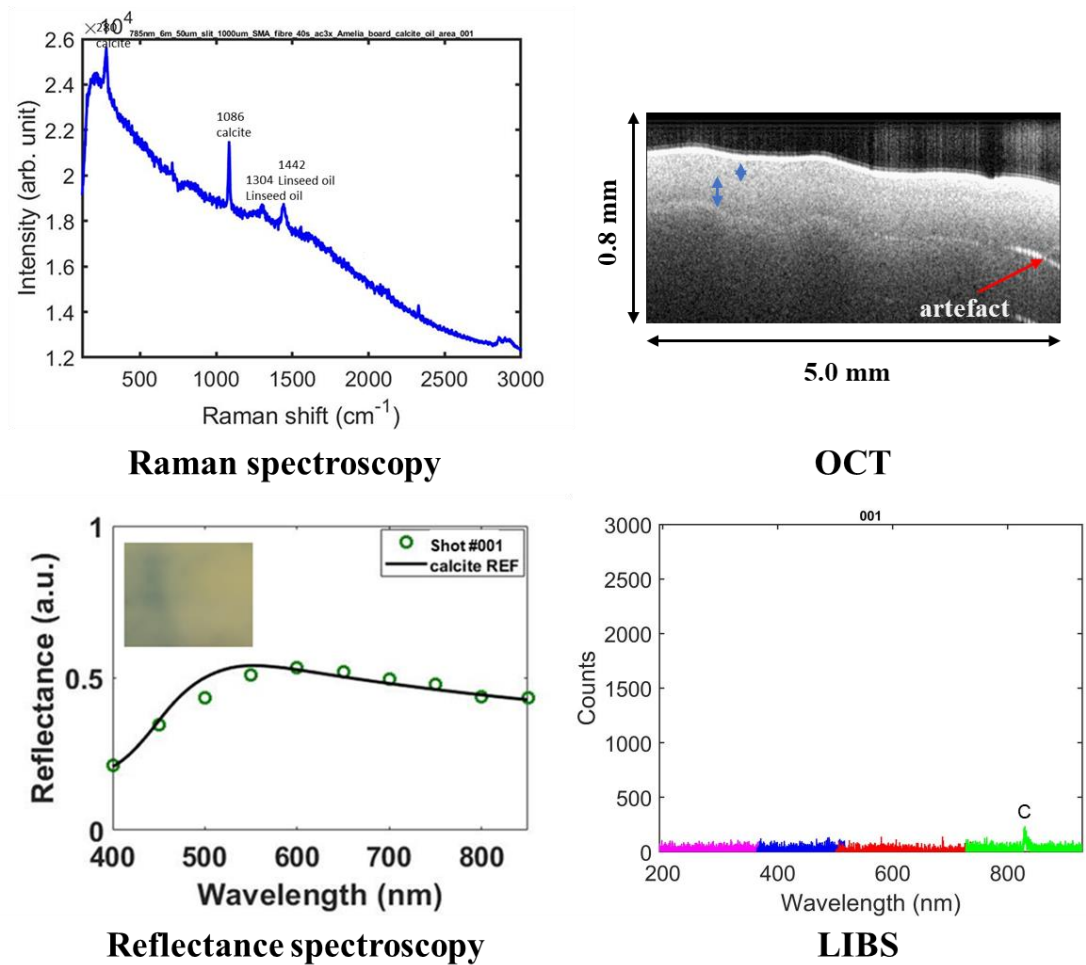


Figure 5.4. Material information of layer 1 collected from the multimodal approach consisting of the following sequence: Raman spectroscopy, OCT, reflectance spectroscopy, and LIBS (shot #001). The red arrow in the OCT image marks the artefact. Two blue arrows show that the calcite layer was stratified. The reflectance spectrum was obtained by spectral imaging and is plotted with a reference curve of calcite; the inset presents the colour image of the region of interest. It is worth noting that Raman, OCT, and reflectance spectroscopy were performed before shot #001. Spectral imaging data was processed by Sotiria Kogou.

As revealed by the OCT image (Figure 5.5), the 1st shot ablated a considerable amount of materials ($\sim 200 \mu\text{m}$ in depth). Assisted with the colour image from spectral imaging, it seems that the whole calcite layer was penetrated thus the bottom of the crater reached the Prussian blue/lithopone layer. Images from the spectral imaging and OCT suggested

that the greyish area at the centre might be degraded Prussian blue by the laser pulses. The reflectance spectrum acquired from the exposed blue area was in good agreement with a reference curve of the mixture of Prussian blue and lithopone from a best fit KM model. For Raman spectroscopy, a peak of Prussian blue at $\sim 2155 \text{ cm}^{-1}$ was identified, while weaker signals of calcite were present which might come from the remaining material at the edge of the crater. Multiple emission lines of Fe, Zn, and Ba were observed in the 2nd LIBS spectrum, confirming the presence of Prussian blue ($\text{Fe}_4[\text{Fe}(\text{CN})_6]_3 \cdot n\text{H}_2\text{O}$, $n = 14\text{--}16$) and lithopone (a mixture of ZnS and BaSO_4).

Layer 2 (shot #002)

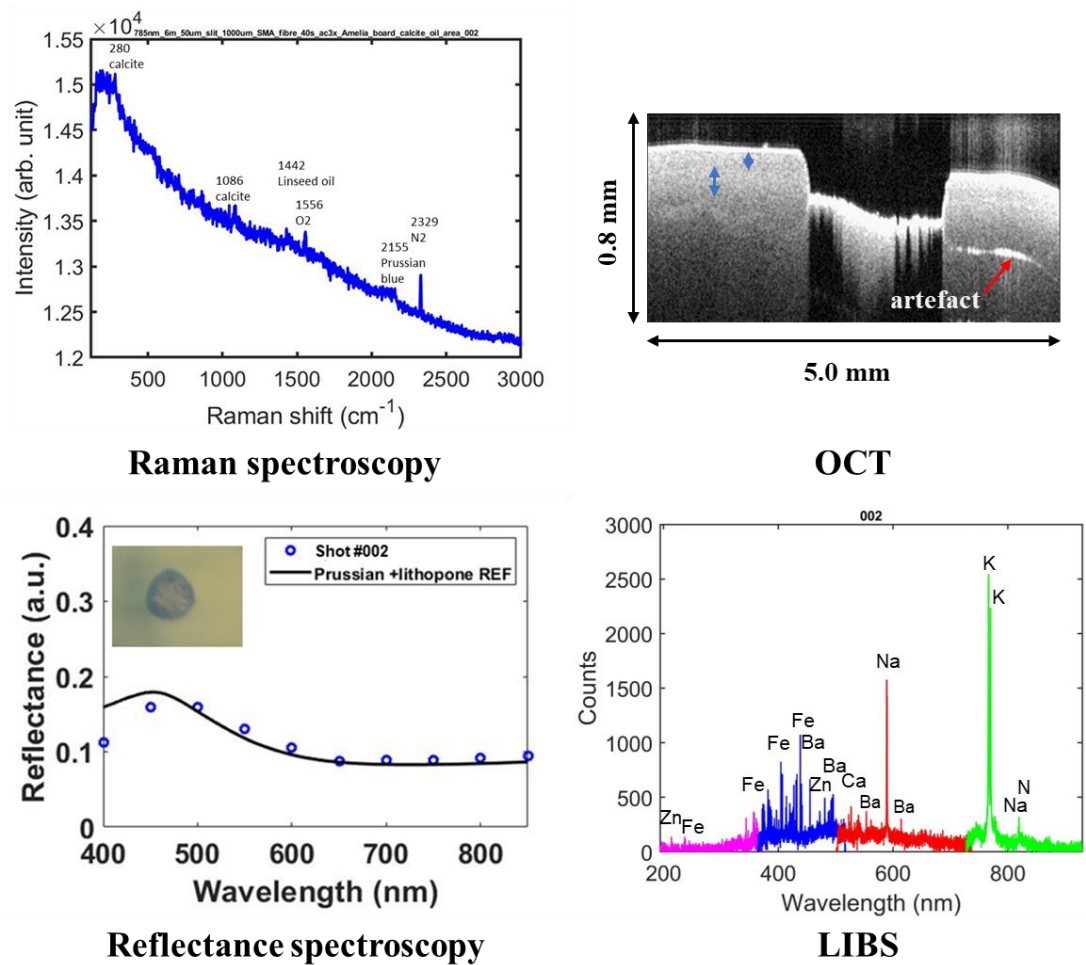


Figure 5.5. Material information of layer 2 (shot #002) collected from the multimodal approach consisting of Raman spectroscopy, OCT, reflectance spectroscopy, and LIBS. The red arrow in the OCT image marks the artefact. Two blue arrows show that the calcite layer was stratified. The reflectance spectrum, obtained by spectral imaging, was extracted from the blue area as shown in the inset, and is plotted with a reference curve of the mixture of Prussian blue and lithopone from the KM model. It is worth noting that Raman, OCT, and reflectance spectroscopy were performed before shot #002. KM fit was performed by Sotiria Kogou.

Layer 3 is represented by the multimodal information acquired during the 18th shot (Figure 5.6). As clearly revealed in the reconstructed colour image from spectral imaging, a white layer was exposed. A reflectance spectrum collected at the red edge of the crater

was consistent with reference vermilion (HgS) pattern, which was consistent with the LIBS spectrum where multiple intense Hg signals were evident. As complementary evidence to LIBS and reflectance results, a Raman peak of vermilion at 253 cm^{-1} was detected.

Layer 3 (shot #018)

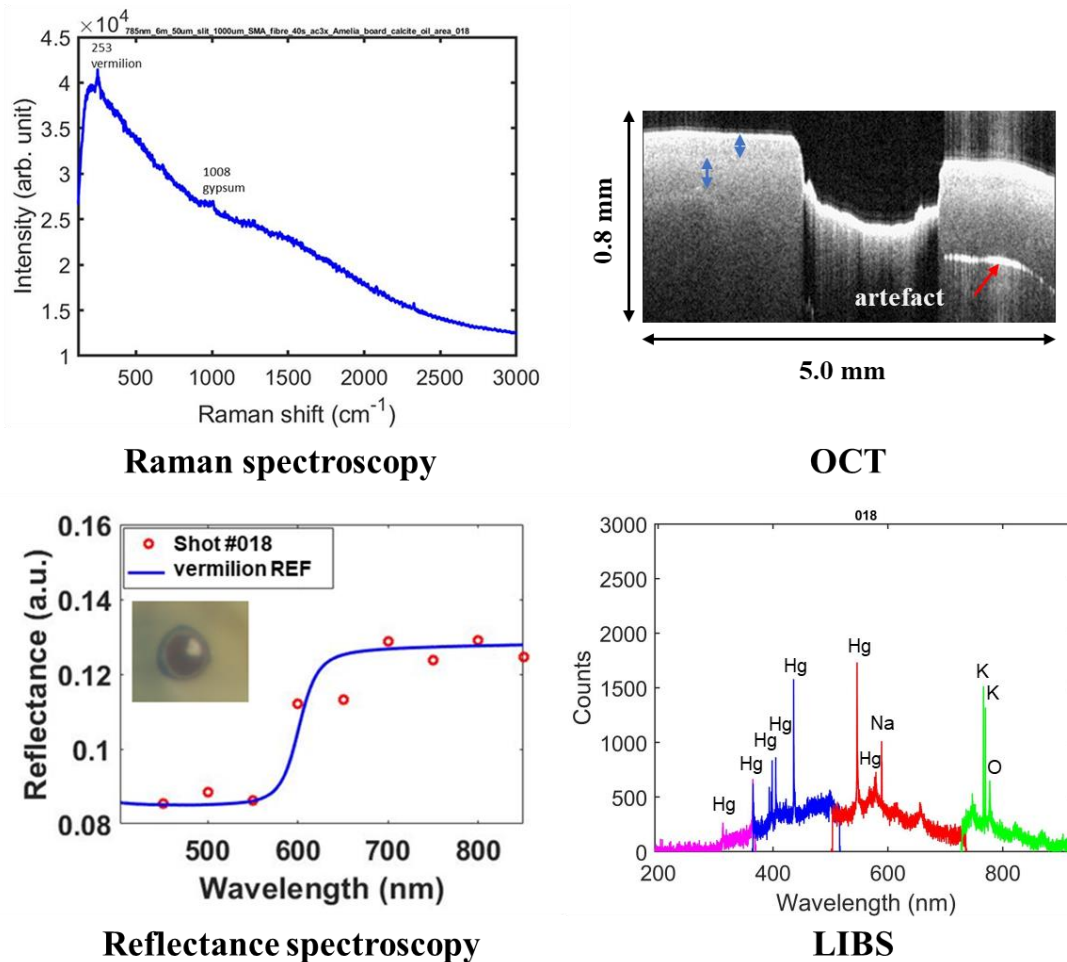


Figure 5.6. Material information of layer 3 (shot #018) collected from the multimodal approach consisting of Raman spectroscopy, OCT, reflectance spectroscopy, and LIBS. The red arrow in the OCT image marks the artefact. Two blue arrows show that the calcite layer was stratified. The reflectance spectrum, obtained by spectral imaging, was extracted from the edge of the crater as shown in the inset and is plotted with a reference curve of vermilion. It is worth noting that Raman, OCT, and reflectance spectroscopy were performed before shot #018. Spectral imaging data was processed by Sotiria Kogou.

Reflectance information extracted from the exposed white area before the 19th shot was in line with a reference gypsum curve (Figure 5.7). Weak Raman signals of gypsum at 1008 cm^{-1} was observed, while vermilion signals were also present, since the examined spot for Raman was larger than the exposed white area so that the surrounding vermilion layer was included. For LIBS, intensities of Ca lines at 393.38 and 396.83 nm increased while Hg signals declined.

Layer 4 (shot #019)

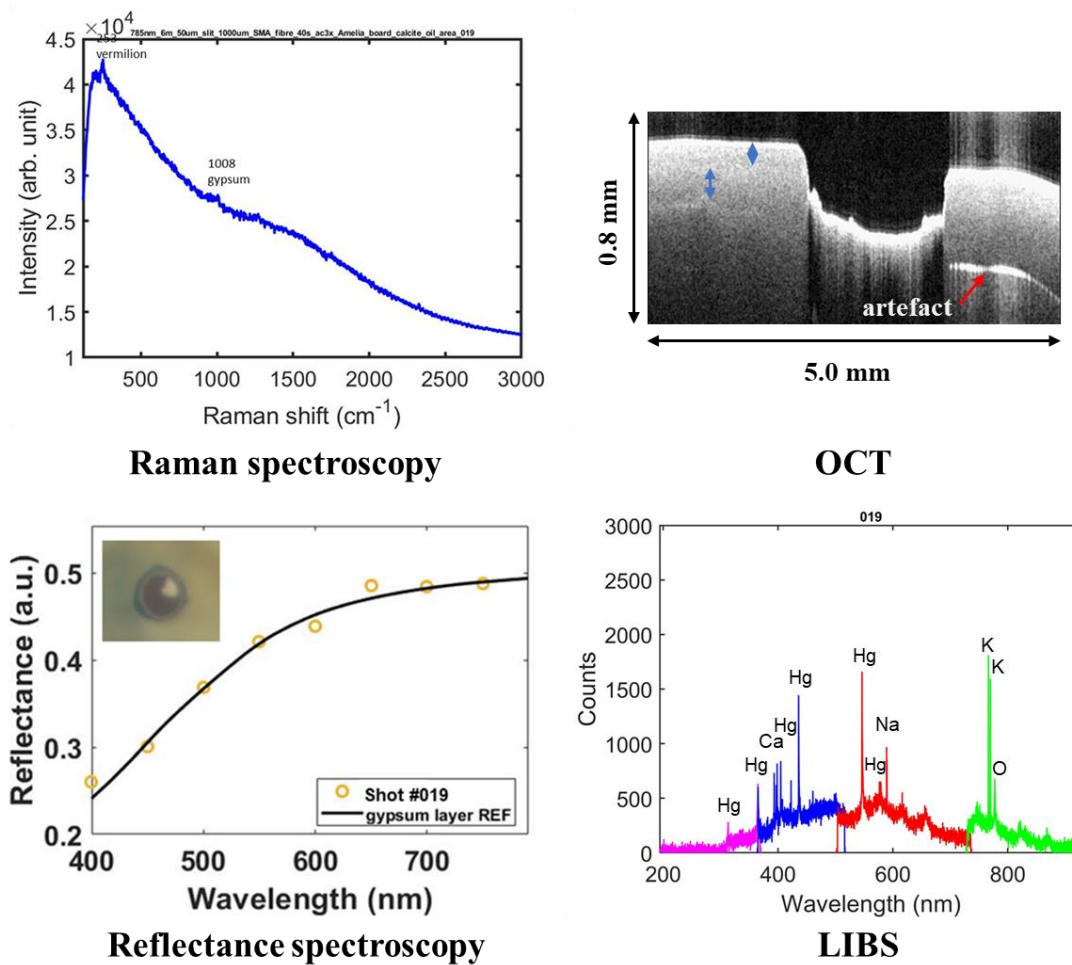


Figure 5.7. Material information of layer 4 (shot #019) collected from the multimodal approach consisting of Raman spectroscopy, OCT, reflectance spectroscopy, and LIBS. The red arrow in the OCT image marks the artefact. Two blue arrows show that the calcite layer was stratified. The reflectance spectrum, obtained by spectral imaging, was extracted from the white area at the bottom of the crater as shown in the inset and is plotted with a reference curve of gypsum. It is worth noting that Raman, OCT, and reflectance spectroscopy were performed before shot #019. Spectral imaging data was processed by Sotiria Kogou.

For Raman spectroscopy, calculation of the net peak counts could reveal the evolution of Raman signals with pulses, which clearly demonstrates the transitions of paint layers from calcite to Prussian blue, vermilion, and then to gypsum (Figure 5.8a). Depth information of the crater can be extracted from OCT images (Figure 5.8b). The analysis of crater

depths as a function of the number of pulses could demonstrate the variation of ablation rate when the crater reached different painting materials.

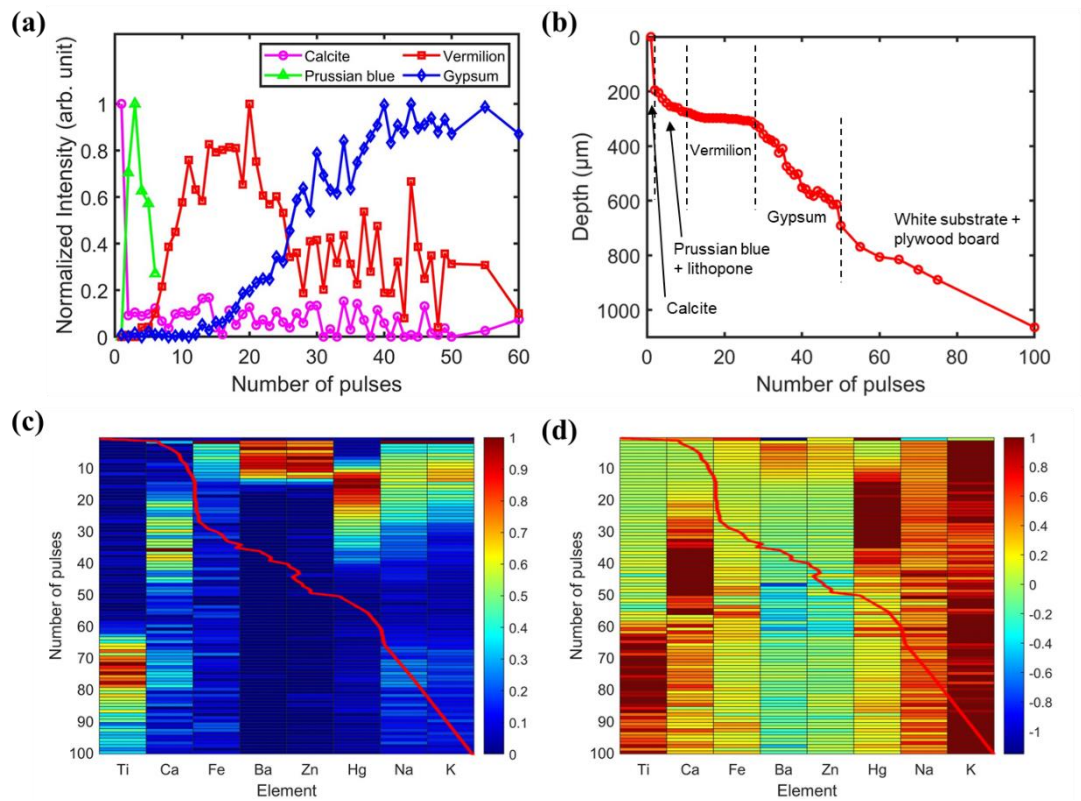


Figure 5.8. Evolution of (a) Raman spectroscopy results; (b) depth information revealed by OCT; (c) LIBS results with depth normalisation; (d) LIBS results with spectrum normalisation.

Similar processing method is also applied to LIBS data (Figure 5.8cd). Noted that typically dozens of emission lines of several or even tens of elements can be present in a single LIBS spectrum, which requires better visualisation methods when compared with tracking the evolutions of a few Raman lines. To simultaneously track the evolution of multiple detected elements, heatmaps extracted from normalised intensities of representative emission lines of elements were introduced to visualise the transitions of paint layers. For LIBS data cube, normalisation can be operated along two dimensions thus provides interpretation in different ways: 1) depth normalisation: intensities of each

emission line along the number of pulses are normalised to be read element by element (intensities are to be compared only in 'depth' per element and not between elements), which give the elemental distribution in depth; 2) spectrum normalisation: intensities of all the emission lines in a single spectrum are normalised, which reveal the dominant elements in each pulse and preserves the line ratios (to be read spectrum by spectrum and not to be compared in intensity between pulses). The depth normalisation is used for profiling the evolution of intensities of elements, while the spectrum normalisation is used for determining the relative elemental composition in each spectrum. The relative intensities of different elements should not be compared in depth normalisation. Similarly, the relative intensities of one element in different shots should not be compared in spectral normalisation. By combining information from both normalisations, the layer-by-layer elemental composition can be better understood. Representative emission lines of identified elements include Ti (453.40 nm), Ca (396.83 nm), Fe (407.14 nm), Ba (455.40 nm), Zn (481.05 nm), Hg (435.83 nm), Na (589.00 nm), and K (766.49 nm). The above lines were chosen carefully not to be overlapped with other signals. With elemental (LIBS) and depth (OCT) information combined, it is feasible to calculate the depth distribution of the elements.

From Raman spectroscopy evolution plot, the calcite signal was only significant before the 1st shot. Afterwards, LIBS signals of Fe, the main element in Prussian blue, peaked at the 2nd shot and were present during 2–14 shots, while Raman evolution curve demonstrated that Prussian blue was detected at 2–6 shots. Noted that with the decline of Prussian blue signals, vermilion signals emerged and then increased significantly. The remaining Fe signals in LIBS most likely came from the wall of the crater. As evidence of lithopone, the presence of Ba and Zn signals in 2–14 shots were in line with Fe patterns. It is worth noting that unlike the Fe signals that peaked at the 2nd shot and declined

afterwards, Ba and Zn signals culminated later, at around 4–7 shots, which might result from the heterogeneous mixture of Prussian blue and lithopone. Unfortunately, no Raman signal of lithopone was detected, probably because of the low amount of lithopone in the mixture. The ablation rate appeared to be steady in this mixed layer. It can be inferred that the thickness of this layer was $\sim 80 \mu\text{m}$. Hg signals corresponding to vermilion were present at 7–40 shots and culminated right after the disappearance of Ba and Zn features, at around 14–16 pulses. A Raman peak of vermilion at 253 cm^{-1} was detected at 6–27 shots, which agrees well with the LIBS evolution where Hg signals were at the peak. It was observed that during this period the ablation rate was exceedingly low. The ablation depth remained nearly unchanged during 15–20 shots, suggesting that vermilion is harder to ablate. The broadening of the crater was observed at the same time, indicating that the ablated material mainly came from the wall of the crater rather than its bottom, which could explain the presence of remaining Hg signals in LIBS until the 40th shot when Raman signals of vermilion were not present after the 27th shot. The vermilion layer was as thin as $\sim 25 \mu\text{m}$. Similarly, when the reflectance pattern was consistent with gypsum during the 19th shot, Ca signals emerged in LIBS evolution plot and lasted until the 50th shot. It peaked at the 36th shot when Hg signals ceased to exist. Raman signals of gypsum emerged before the 18th shot and remained until the end. OCT images demonstrated that the ablation rate in gypsum was significantly higher than the previous layers. It can be estimated that the thickness of the gypsum layer was $>350 \mu\text{m}$. Beyond gypsum, another sign of Ca was observed in LIBS evolution plot, appearing at the same time as the intense Ti signals starting from the 63rd shot until the end of the test, which confirmed the Raman detection of rutile and chalk at the surface of the white substrate layer prior to this study. The evolution plots of Raman and LIBS are in general consistent, which however do not mean they are exactly simultaneous in terms of the number of pulses. It seems that Raman

signals usually end earlier than LIBS signals. It is known that Raman signals are collected from the bulk, while LIBS signals come from the ablated layer of the materials. When a paint layer is almost penetrated, the remaining material at the bottom of the ablation crater can still generate sufficient LIBS signals, while Raman spectroscopy starts to reveal deeper information. In addition, later pulses could still ablate materials at the wall of the V-shaped crater (Figure 5.3), continuing to reveal elemental information from the depth that has already been reached.

The laboratory evaluation demonstrated the capability of the multimodal remote standoff spectroscopic approach for *in situ* depth-resolved material identification, where information collected from multiple techniques can be interpreted in a combined manner. The experimental methodology tested in laboratory environment laid a solid foundation for *in situ* analysis of historical wall paintings.

5.4. *In situ* analysis of wall paintings

Following the successful laboratory tests, a unique *in situ* application in the Cathedral Church of St Barnabas in Nottingham, UK, was arranged for this remote standoff multimodal spectroscopy system to perform depth-resolved analysis on wall paintings. The Cathedral Church of St Barnabas in Nottingham, consecrated as a church in 1844 and then raised to cathedral status in 1852, is an outstanding outcome of the Gothic Revival movement in England. Augustus Welby Pugin (1812–1852), a leading figure in the English Roman Catholic and Gothic Revivals and perhaps the foremost British architect of the 19th century, was its architect and interior designer. Within the Unity Chapel, Pugin's wall paint scheme was covered over in several later redecorations (not well documented) and is the object of this investigation. Since nowadays the walls of the Unity

Chapel are whitewashed, the unknown paint stratigraphy could hardly be analysed by conventional non-destructive methods. Our *in situ* multimodal remote standoff spectroscopic approach could be an ideal solution for such a research subject. The stratigraphy of the mural was the focus of our investigation since it could help understand Pugin's original paint scheme and how later refurbishment was done.

The standoff multimodal system was set up where LIBS and Raman systems were arranged in an oblique design (Figure 5.1) for *in situ* analysis. Different areas of the mural in the Unity Chapel were studied at a distance of 6.7 m from the same position on the ground. Measurements were performed across the East wall paintings of the Unity Chapel (Figure 5.9). To minimise the impact of the analysis, LIBS measurements were performed near the edges of already damaged areas: four whitewashed spots, WG1, WG2, WB1 and WB2, were selected for examination. Reflectance spectroscopy was achieved using a FORS system since our remote spectral imaging system, PRISMS, was unfortunately occupied in other projects during this field campaign. For time efficiency reasons, Raman and FORS measurements were performed only when clear alterations in LIBS spectra were observed. LIBS heatmaps were plotted to visualise the normalised intensities for the representative emission lines of identified elements: Ti (453.40 nm), Ca (422.69 nm), Ba (553.55 nm), Zn (481.05 nm), Pb (405.78 nm), Na (589.00 nm), K (766.49 nm), Mn (601.99 nm), Sr (460.73 nm), Cr (520.67 nm), Sn (645.36 nm), Cl (837.60 nm), Cd (508.56 nm), and Mg (448.10 nm). The above lines were chosen carefully not to be overlapped with other signals.

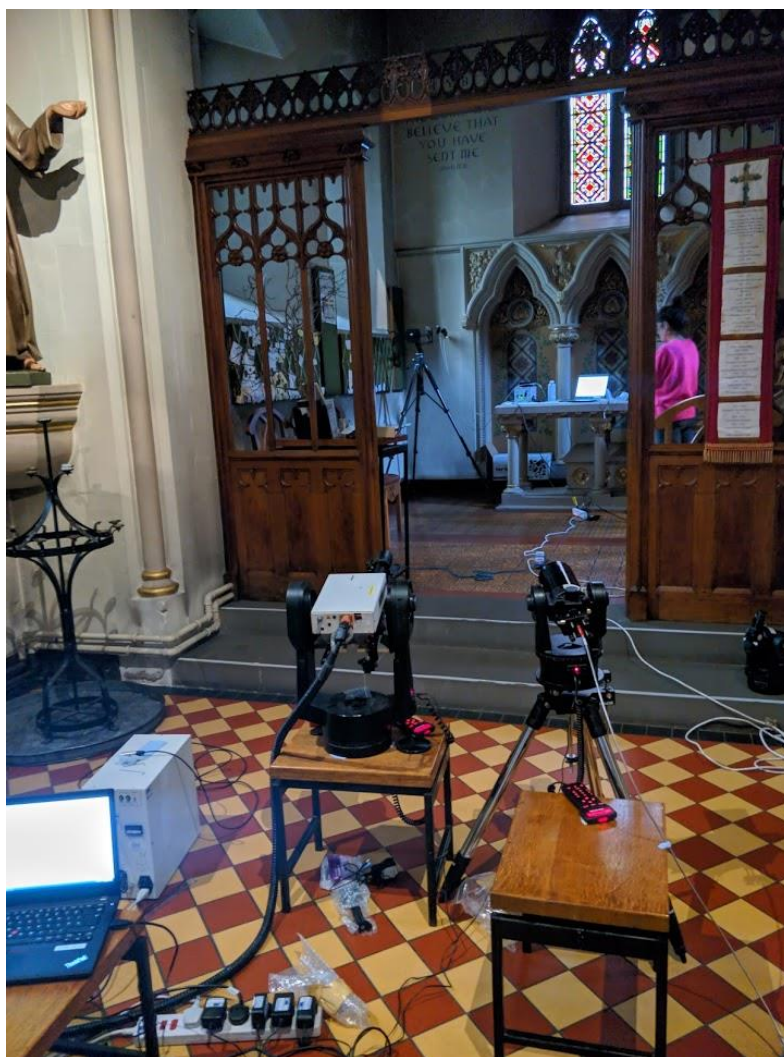


Figure 5.9. The multimodal remote standoff spectroscopic system performing *in situ* depth-resolved analysis of the whitewashed wall paintings in the Unity Chapel, Cathedral Church of St Barnabas, Nottingham.

The investigation started from two spots on the whitewash surface (WG1 and WG2) neighbouring an exposed green paint. LIBS and Raman spectra were collected for the first examined spot WG1 (Figure 5.10a,b, 5.11a). For Raman spectroscopy, it was observed that before the 1st LIBS shot, peaks at 450 and 609 cm^{-1} corresponding to rutile (titanium dioxide, TiO_2) were detected (Figure 5.11a), and these continued to be detected (but getting weaker) after the 7th shot. The 1st laser pulse removed the dust from the

sample surface. From the 2nd to 40th pulse, LIBS spectra were dominated by Ti peaks, with also the presence of Ca, Ba, Na, K, Sn, Cl, Cd, Mg. All of the above elements illustrate similar pattern except for Ba, which peaked at the 4th spectrum, suggesting that the stratigraphy of the whitewash layer might not be uniform in composition. No clear signals could be identified in the Raman spectrum after the 39th shot. After the 40th shot, Cr signals emerged with Pb, and peaked at the 45th spectrum, while most of the previously dominating elements, including Ti, Cl, Cd and Mg, disappeared abruptly. Starting from the 46th shot, Ba, Zn, Mn, Sr and Sn signals appeared simultaneously until the 54th shot, suggesting a new layer right after the Cr dominated layer. One Raman peak at 990 cm^{-1} appeared throughout the spectra before the 43rd, 49th and 52nd shots, indicating the presence of barium sulfate (BaSO_4). It is worth noting that before the 49th shot, another Raman peak at 439 cm^{-1} was detected, which could be assigned to zinc oxide (ZnO). Before the 55th shot, no clear Raman signals could be identified. One shot before that, intense Pb signals were detected in LIBS spectra, along with Ca and Ba.

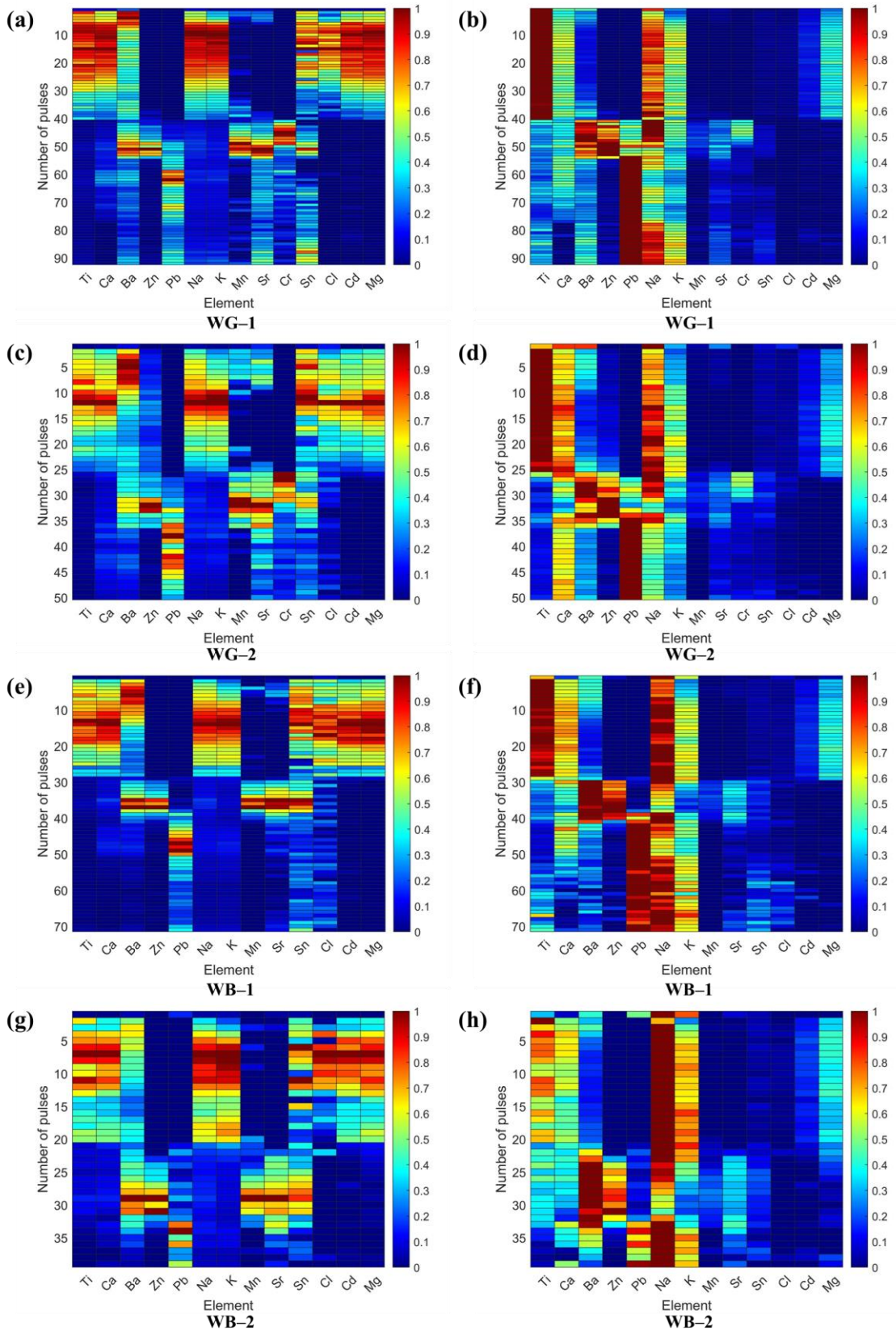


Figure 5.10. (a) heatmaps normalised along depth (a,c,e,g) and spectrum (b,d,f,h) dimensions of LIBS results in four whitewashed spots, WG1, WG2, WB1 and WB2.

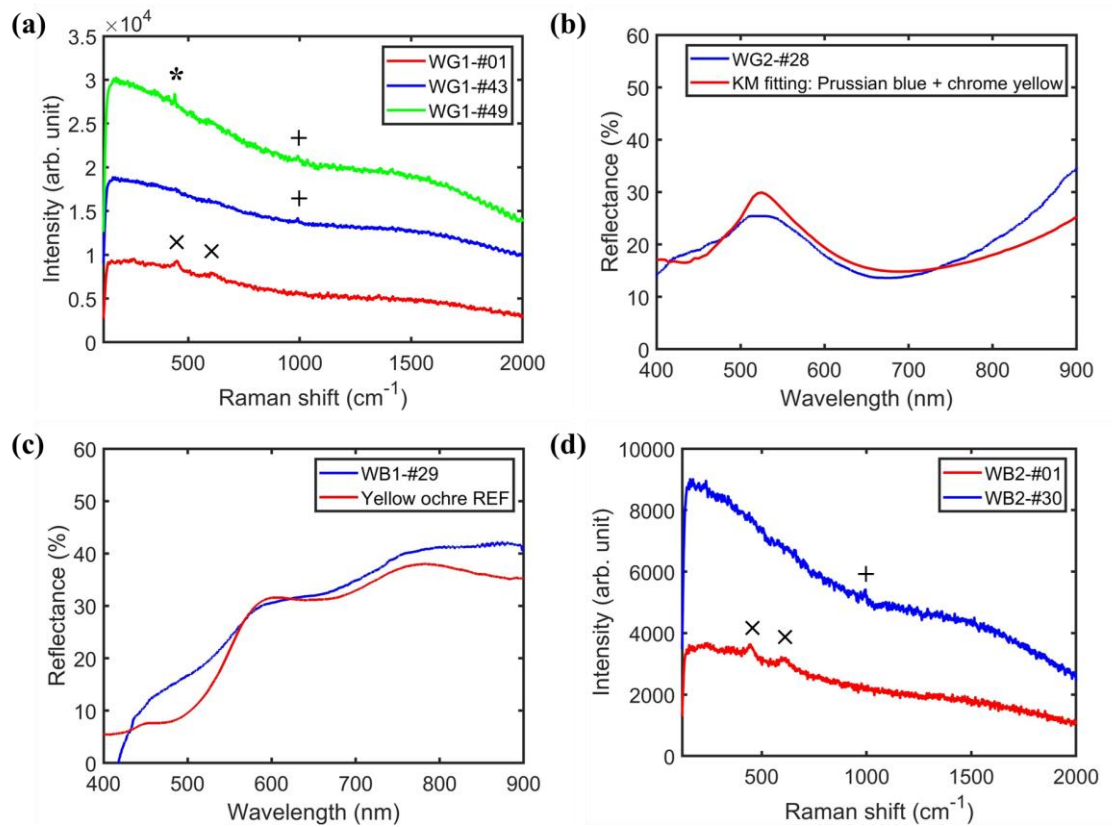


Figure 5.11. Result of Raman spectroscopy and reflectance spectroscopy. (a) Raman results of WG1. (b) reflectance spectrum of a green layer in WG2 with KM fitting using a mixture of Prussian blue and chrome yellow. (c) reflectance spectrum of an exposed brown layer in WB1, compared with the reference curve of yellow ochre. (d) Raman results of WB2. For Raman signals, rutile peaks are marked as X; BaSO₄ peaks are marked as +; ZnO peaks are marked as *. KM fit was performed by Sotiria Kogou.

LIBS and FORS spectra were collected for the second examined spot WG2 (Figure 5.10cd). Layer information extracted from LIBS results of WG2 is largely in line with that of WG1, except that the signal of the elements marking the possible whitewash layer (Ti, Ca, Ba, Na, K, Sn Cl, Cd, Mg) only lasted around 25 shots, much fewer than what was required for WG1 (40 shots). This may suggest the non-uniform thickness of the whitewash layer. Among these elements, Ba still peaked first. Cr signal appeared later with Pb and was strong at the 26–27th spectrum, which agrees with the FORS findings.

A detailed inspection of signals from the reflectance spectrum taken before the 28th shot revealed spectral features of the green pigment layer (Figure 5.11b). Images of the investigated area collected from the guiding camera of the standoff Raman system offered visual evidence of the ablation process, which, in accordance with the FORS results, clearly revealed a green layer before the 28th shot, while the images corresponding to the previous two shots presented the whitewash layer upon it (Figure 5.12).

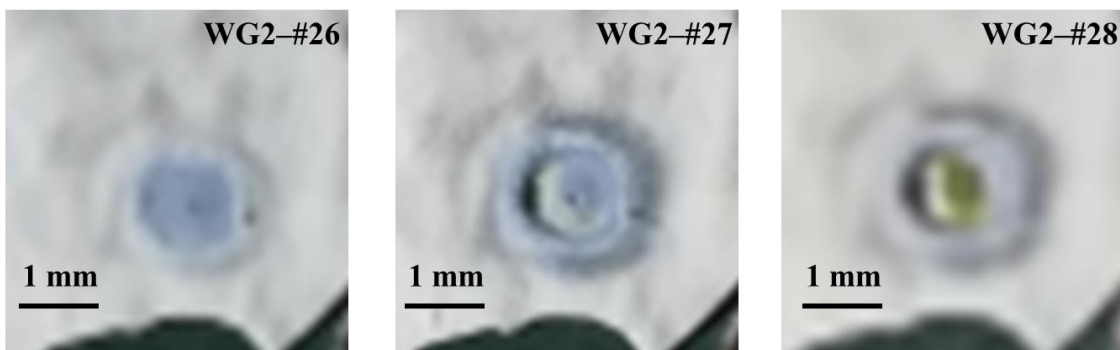


Figure 5.12. Images taken from the guiding camera on the standoff Raman system recording the ablation process that reveals the green layer of this stratigraphy.

Two whitewashed spots, neighbouring an exposed brown paint layer at the edge, were examined. LIBS and FORS spectra were collected for the first spot WB1 (Figure 5.10e,f). The composition of the whitewash is consistent with that found from the WG datasets. Different from the results of the green area, no Cr signals were detected after the whitewash. The FORS spectrum taken before the 29th shot (Figure 5.11c) demonstrated spectral features similar to yellow ochre ($\text{FeO}(\text{OH})$) [168]. Unfortunately, most Fe lines are distributed in UV region, thus hardly detectable due to absorption by the aberration correction glass plate of the telescope, which makes the analysis of Fe distribution difficult. Later layers were consistent with the results of WG1 and WG2. Intensities of Ba, Zn, Mn, Sr and Sn lines peaked at around 35–37th shots. Subsequently, dominant Pb

signals, as well as Ca, Ba, Na, and K, were present during the 43rd to 50th shots. A deeper layer (after ~60 shots), characterised by increasing intensity of Pb, Na, K Sr, Sn and Cl, was revealed afterwards.

LIBS and Raman spectra were collected for the second examined spot WB2 (Figure 5.10gh). Layer information concluded from LIBS data is pretty much the same as the previous dataset. The 1st Raman spectrum (Figure 5.11d), taken before the LIBS measurements, revealed two peaks at 446 and 608 cm^{-1} , which are assigned to rutile. No clear signals regarding ochre were captured after the 17th and 20th shots, respectively, where the brown layer was suggested by results of WB1. According to previous pigment survey conducted in the laboratory using reference samples, the minimum integration time required for the detection of ochre is 10 min, which is much longer than what was used in this *in situ* analysis. The next Raman spectrum collected before the 22nd shot revealed a peak of BaSO_4 at 993 cm^{-1} , which remained until the 34th shot, then disappeared after the 39th shot. The period when Raman signals of BaSO_4 were present was consistent with the LIBS evolution plot, where Ba peaked during the same time.

5.5. Interpretation of the wall painting structure

Although different depths had been reached due to various numbers of pulses, evolution plots of LIBS results from different spots suggest that layer structures are largely consistent with each other. Therefore, it is reasonable to take a comprehensive view of the wall painting stratigraphy that was revealed by the combined information obtained from LIBS and complementary spectroscopic techniques (Raman spectroscopy and reflectance spectroscopy).

For the two areas under investigation, except for the colour layer (green and brown) revealed by the crater colour and the spectroscopic analysis, it is indicated that they have similar multilayer structure when results of all three techniques are taken into consideration. This indicates that the green and the brown paints belong to the same layer. In total, at least 7 layers have been revealed from top to bottom of the stratigraphy. Layer information extracted from all techniques is summarised in Table 5.1.

Table 5.1. Summary of layer information based on the results obtained from multimodal remote standoff spectroscopic approach.

Stratigraphy	Identification		
	LIBS	Raman spectroscopy	Reflectance spectroscopy
Layer 1	Ti, Ca, Ba, Na, K, Sn, Cl, Cd, Mg	Rutile (TiO ₂)	-
Layer 2	Ti, Ca, Ba, Na, K, Sn, Cl, Cd, Mg	Rutile (TiO ₂)	-
Layer 3	WG: Cr, Pb WB: -	-	WG2: Prussian blue (Fe ₄ [Fe(CN) ₆] ₃ ·nH ₂ O, n =14–16) and chrome yellow (PbCrO ₄) WB1: Yellow ochre
Layer 4	Ca, Ba, Zn, Na, K, Mn, Sr, Sn	BaSO ₄ , ZnO	-
Layer 5	Ca, Pb, Na, K	-	-
Layer 6	Ca, Ba, Pb, Na, K, Sr	-	-
Layer 7	Ca, Ba, Pb, Na, K, Sr, Sn	-	-

Starting with the surface, the whitewash is distinguished by the presence of Ti, Ca, Ba, Na, K, Mn, Sr, Sn, Cl, Cd, and Mg in terms of the elemental composition. The evolution patterns are found to be consistent for the majority of the aforementioned elements. However, it is clear in almost all datasets that Ba signals peaked earlier than the others. Therefore layer 1 is defined as a Ba-rich layer on top of the rest of the whitewash, which is then regarded as layer 2. Layer 1 is mainly composed of TiO₂, confirmed by Raman spectroscopy in the form of rutile, a white pigment that was not available in Europe until after 1945 [169], which suggests that this layer does not correspond to the interventions of the 1930s. This white paint layer is characterised by the presence of Ba, suggesting a white composite paint comprised of rutile and BaSO₄ which is often used as an extender

[170]. Layer 2 is characterised by Ti, Ca, Na, K, Cd, Mg, Cl, and Sn, and required higher number of pulses to ablate than for layer 1.

Layer 3 revealed two distinct paint colours as the laser pulses approached the end of the whitewashes. Reflectance data collected from the brown areas of the 3rd layer gave the best fit using yellow ochre as reference (Figure 5.11c). Cr was identified by LIBS to be the dominating element in the green area. All Cr-containing pigments were tested as references for the KM fitting. The mixture of Prussian blue ($\text{Fe}_4[\text{Fe}(\text{CN})_6]_3 \cdot n\text{H}_2\text{O}$, $n = 14-16$) and chrome yellow (PbCrO_4) generated the best KM fitting that matches the FORS spectra obtained from the green area (Figure 5.11b). Although Pb signals appear to be insignificant in the evolution plot using depth normalisation, it is clear that Pb is present in this green layer and is consistent with the appearance of Cr signals in the evolution plot using spectrum normalisation, which strongly supports chrome yellow (PbCrO_4) as the yellow pigment in this paint layer. It was common practice to mix Prussian Blue and Chrome Yellow to achieve a green hue in the 19th century [170].

Then, a layer 4 featuring Ba, Zn, Na, Mn, Sr, Sn, as well as Ca and K, appeared underneath both the green and brown regions. BaSO_4 and ZnO , both confirmed by Raman spectroscopy, constitute a common white mixture [171], thus suggesting a white layer. The presence of Mn possibly as MnO_2 alone or in combination with iron oxides (iron black) might give the white substrate a darker tone.

The determination of layer 5 is largely assisted by the evolution plot using spectrum normalisation rather than depth normalisation (Figure 5.10b,d,f). The former clearly indicates that Pb takes over and becomes dominant from this stratum onwards. Other discovered elements include Ca, Na, and K.

Strong Pb and Ca signals predominate in layer 6, along with certain amounts of Ba, Na, K, and Sr. Pb signals in this layer are substantially stronger than those in the preceding layer, where Pb first appears and then maintains a certain level, indicating a different material composition. Given the simultaneous presence of high Ca, the white layer might be made of lead white ($2\text{PbCO}_3 \cdot \text{Pb(OH)}_2$) and chalk/gypsum, with a small amount of BaSO_4 added.

The deepest layer (layer 7), characterised by increasing intensity of Pb, Na, K, Sr, and Sn, is revealed at the very bottom. Whether the laser pulses penetrated the substrate plaster is difficult to assess. However, evolution plots of several datasets (Figure 5.10b,f) show a similar pattern that with considerably more pulses, compared with numbers of pulses required to remove preceding layers, no new layer is revealed afterwards. Additionally, another depth-profiling LIBS analysis on a patch of exposed plaster revealed a similar elemental composition.

5.6. Conclusions

In this work, the combination of remote standoff LIBS, Raman spectroscopy, and reflectance spectroscopy enables the multimodal analysis for the material identification of multilayer wall paintings. The multimodal approach was evaluated in laboratory environment for the capability of depth-resolved analysis and to gain insight on how to interpret the results, and then successfully implemented in the Cathedral Church of St Barnabas in Nottingham to analyse the material structure of the whitewashed wall paintings in the Unity Chapel in order to better understand the original painting scheme designed by the celebrated architect Augustus Welby Pugin and details of later redecorations, and therefore inform decision-making for future conservation plans. The elemental composition evolution suggests that at least 7 distinct layers can be revealed. Different colour areas present similar underlayer patterns, suggesting a uniform stratigraphy.

Chapter 6

Conclusions

The objective of this work was the development of remote standoff laser spectroscopy systems for the study of wall paintings, monuments and architectural interiors, as well as their combined use for *in situ* multimodal material analysis in cultural heritage research such as history of wall paintings and salt damage in historical buildings.

The study was focused on two directions: the design and development of remote standoff laser spectroscopy systems with unique requirements in heritage research considered, and their deployment and operation for *in situ* analysis in field campaigns.

The major achievements in this project are: 1) The development of a remote standoff Raman spectroscopy system dedicated to heritage research, in particular for wall paintings. It is the first of its kind in cultural heritage studies as acknowledged by recent reviews in this field [133,172], which successfully performed *in situ* investigations of wall paintings at distances of 3–15 m [112]. 2) This Raman spectroscopy system successfully pioneered *in situ* remote standoff macro Raman mapping of wall paintings [136]. 3) Following the development of a remote standoff LIBS system, the combined use of remote standoff systems, LIBS, Raman spectroscopy and spectral imaging, pioneered remote *in situ* multimodal analysis of wall painting stratigraphy from a fixed position on the ground at a large distance.

The idea of developing remote standoff laser spectroscopy stemmed from the challenges of *in situ* cultural heritage research encountered during our group's previous field campaigns. It is difficult to study upper parts of large wall paintings on high walls or those painted on ceilings, using conventional mobile analytical instruments. Environmental

restrictions also hinder their deployment and operation for measurements at close range. Even with the aid of scaffolding, sensitive measurements requiring long integration time are hard to perform. Remote analytical techniques can be a good solution. A visible/near infrared (VIS-NIR) remote spectral imaging system, PRISMS, has been developed with the ability to image wall paintings at sub-millimeter resolutions at 3–30 m [11], which can provide reflectance spectroscopy information. Other remote standoff spectroscopic methods that can give complementary information such as molecular and elemental compositions are desirable. Remote standoff systems employing lasers such as Raman spectroscopy, LIBS and LIF are ideal choices.

First of all, a remote standoff Raman spectroscopy system using a CW laser source at 780 nm was developed with ability to work from a distance of 3–15 m. It is capable of identifying most of common historic artist pigments (as presented in Appendix 1). The decision of the preferred excitation wavelength was based on considerations of Raman efficiency, avoiding laser induced fluorescence and potential laser induced degradation. A daylight subtraction procedure achieved by laser modulation was developed, which made the remote standoff Raman system capable of operating under the influence of indoor ambient light. Remote standoff Raman spectroscopy was demonstrated to be able to provide molecular information of high specificity remotely, complementing PRISMS, our current visible/near infrared remote spectral imaging for wall paintings.

LIBS is an elemental analytical technique with unique advantages over other conventional methods adopted in heritage research. The remote standoff LIBS system was designed in an oblique geometry, that can work at >6 m distances. A pulsed laser at 1064 nm was employed as the excitation source, providing a pulse energy of 50 mJ and a pulse width of 5–7 ns. With the laser beam focused to ~1 mm on a distant target surface, peak intensity of the laser pulse at sample could reach 1.27 GW/cm². The system was

configured to operate in time-integrated mode. The evolution of LIBS signals is used for depth-resolved analysis. The signal processing was assisted by an in-house written software for automated emission line assignment, which adopted the NIST atomic spectral database and additional data according to literature. The standoff LIBS system was capable of detecting characteristic emission lines of elements on a range of pigment samples.

Another laser spectroscopy technique LIF is implemented, which can be an efficient tool in many areas of heritage studies, including identification of fluorescent pigments, stones and biodeteriogens. A remote LIF system was developed employing telescopes. The same Q-switched laser source used for LIBS was used in LIF, with its excitation wavelength configured to the third harmonic (355 nm). Several fluorescent semiconductor pigments were selected to test the remote standoff LIF system. The resulting fluorescence signals were in good agreement with findings in literature.

Following the development of our remote standoff Raman system, the main concern was its safe use in heritage studies in terms of laser induced degradation effect. A combined system of standoff Raman spectroscopy and reflectance spectroscopy was set up to verify the safety of the Raman laser and the sensitivity of Raman as a tool for identification of laser-induced degradation effects on pigment samples. Raman spectroscopy was found not sensitive enough to detect subtle laser-induced degradation effects, compared to reflectance spectroscopy. Reversible degradation effects were observed for the first time. Laser irradiation experiments were designed using three different laser sources in our laboratory, including a 780 nm CW, a 532 nm CW and a 532 nm pulsed lasers. With regard to laser wavelength, 780 nm CW seemed to be less damaging than 532 nm CW to the studied pigments as changes in reflectance spectra post irradiation was observed when using the 532 nm CW, while no damage or temporary alteration was noticed when

applying the 780 nm CW, given that the 780 nm CW even has higher intensity (0.36 W/cm²) than the 532 nm one (0.26 W/cm²). Given the same total energy, a higher laser intensity seemed to be more damaging, as tested on a range of common pigments. The degradation as reflected by the scale of changes in reflectance was at a more serious level, when longer irradiation time was applied, indicating that with the same laser power and spot size hence same intensity, more laser energy accumulated posed a greater risk in laser-induced damage. The upgraded 780 nm remote standoff Raman system with a focused beam of 1 mm at sample was shown to be able to operate safely for most pigments tested when using typical time required for Raman measurements. Although alterations in reflectance were detected post laser irradiation for some pigments, reversions were observed shortly afterwards, indicating a non-permanent process.

The standoff Raman system was successfully deployed in several field campaigns of heritage sites:

1. It managed to identify the pigments used in the Blessed Sacrament Chapel of the Cathedral Church of St Barnabas in Nottingham. Combined with historical records of the building and the history of various historic and modern synthetic pigments, the current painting scheme is most likely applied after the church consecration in 1844 but before the 1933 renovations, therefore might not be the original scheme of the celebrated architect Augustus Welby Pugin.
2. The *in situ* remote standoff Raman analysis was successfully conducted on wall paintings in a chapel of the Convent of Mercy designed also by Augustus Welby Pugin in Nottingham. The identification of vermilion in a cleaning test area and a modern pigment, phthalocyanine blue at the surface layer suggested that the

underneath paint layer is likely to be from before the early 20th century and the redecoration was carried out after the 1950s.

3. The remote standoff Raman system allows *in situ* remote macro Raman mapping, which could reveal the spatial distribution of pigments and degradation products and monitor the condition of material degradation on a macroscopic scale. An in-house written program controlling the motion of the Raman system enables automated Raman mapping. The *in situ* remote macro Raman mapping was successfully performed on a small area of a chinoiserie wall painting at the Royal Pavilion, Brighton, as proof of concept, revealing the distribution of vermilion and chrome yellow, which are the main pigments in the painting scheme.
4. The application of the remote standoff Raman system can be further extended from wall paintings to general architectural materials, e.g. for determination of the types of stones or to monitor the deterioration of buildings under the influence of the environment. For instance, the system was proved to be able to conduct long-time monitoring of salt formation process for several hours, and was used for the inspection of salt damage in historical buildings at Fort Brockhurst. It successfully detected different types of salts on the walls. Distribution of salts in a large area was revealed by remote standoff macro-Raman mapping, which contributed to the better understanding of the salt formation mechanism and transformation in buildings in coastal environments.
5. A multimodal approach using LIBS to ablate the materials and other complementary techniques including Raman and reflectance spectroscopy to achieve *in situ* standoff depth-resolved material identification of historic architectural interiors at standoff distances was demonstrated for the first time. The remote standoff spectroscopic systems were successfully deployed *in situ* for the examination of the whitewashed

wall paintings in the Unity Chapel of St Barnabas Cathedral Church in Nottingham. Integration of evidence from LIBS, Raman and reflectance spectroscopy revealed the multilayer structure of the hidden wall paintings, providing important insights for better understanding the painting materials and the conservation history of the Cathedral.

Based on the above results and conclusions, prospects for the future work can be suggested:

1. Fully automated control of the remote standoff laser spectroscopy systems: Motorised beam expander can be used, with the assistance of the images taken from the guiding camera, for automated focusing of the laser beam. It can be more convenient for *in situ* alignments where manual focusing can be difficult due to restricted environmental conditions, such as when the systems sit on wooden floor. System programming that controls the entire measurement process can be implemented, including the integration of the software that controls the motion of the laser beam and the collection of the spectra, the synchronisation of LIBS and Raman measurements using alternating laser beams for automated depth-resolved analysis, etc.
2. Optimisation of spectrum collection: Telescopes with smaller f-number should be adopted in the remote standoff laser spectroscopy systems, which are able to collect more reflected light. Multi-channel detector systems are used for LIBS collection, which often require a multi-branch fibre bundle to divide light. Instead, it would be more efficient to use a series of dichroic beamsplitters that split the light into different wavelength regions.

3. A promising method that can be easily utilised using the current remote standoff Raman setup is the spatially offset Raman spectroscopy (SORS). It allows the non-invasive characterisation of diffusely scattering materials at different depths by applying a specific spatial offset to the laser spot. In testing of the co-axial remote standoff Raman system, such phenomenon has been observed when the laser beam was misaligned, but not well studied. The automated control of the system could adjust the focusing and positioning of the laser, thus enable SORS analysis using varying spatial offsets.

Bibliography

1. C. V. RAMAN and K. S. KRISHNAN, "A New Type of Secondary Radiation," *Nature* **121**(3048), 501–502 (1928).
2. R. L. McCreery, *Raman Spectroscopy for Chemical Analysis* (John Wiley & Sons, 2001), **12**(5).
3. P. Vandenabeele, *Practical Raman Spectroscopy - An Introduction* (John Wiley & Sons, Ltd, 2013), **29**(5).
4. E. Smith and G. Dent, *Modern Raman Spectroscopy* (Wiley, 2019).
5. F. Brech and L. Cross, "Optical microemission stimulated by a ruby maser," *Appl.Spectrosc* **16**, 59 (1962).
6. E. F. Runge, R. W. Minck, and F. R. Bryan, "Spectrochemical analysis using a pulsed laser source," *Spectrochim. Acta* **20**(4), 733–736 (1964).
7. D. A. Cremers and L. J. Radziemski, *Handbook of Laser-Induced Breakdown Spectroscopy* (John Wiley & Sons, 2006).
8. R. Noll, *Laser-Induced Breakdown Spectroscopy: Fundamentals and Applications* (Springer Berlin Heidelberg, 2012).
9. R. N. Zare, "My life with IIF: A personal account of developing laser-induced fluorescence," *Annu. Rev. Anal. Chem.* **5**(1), 1–14 (2012).
10. R. W. Wood, " LVIII. The fluorescence of sodium vapour and the resonance radiation of electrons ," *London, Edinburgh, Dublin Philos. Mag. J. Sci.* **10**(59), 513–525 (1905).

11. H. Liang, A. Lucian, R. Lange, C. Cheung, and B. Su, "Remote spectral imaging with simultaneous extraction of 3D topography for historical wall paintings," *ISPRS J. Photogramm. Remote Sens.* **95**, 13–22 (2014).
12. M. Delhaye and P. Dhamelincourt, "Raman microprobe and microscope with laser excitation," *J. Raman Spectrosc.* **3**(1), 33–43 (1975).
13. P. Dhamelincourt, "Laser raman molecular microprobe (MOLE)," *Anal. Chem.* **51**(3), 414A-420A (1979).
14. H. G. M. Edwards, D. W. Farwell, and M. R. D. Seaward, "Raman spectra of oxalates in lichen encrustations on Renaissance frescoes," *Spectrochim. Acta Part A Mol. Spectrosc.* **47**(11), 1531–1539 (1991).
15. H. G. M. Edwards, D. W. Farwell, M. R. D. Seaward, and C. Giacobini, "Preliminary Raman microscopic analyses of a lichen encrustation involved in the biodeterioration of renaissance frescoes in Central Italy," *Int. Biodeterior.* **27**(1), 1–9 (1991).
16. A. C. Williams, H. G. M. Edwards, and B. W. Barry, "The "Iceman": molecular structure of 5200-year-old skin characterised by raman spectroscopy and electron microscopy," *Biochim. Biophys. Acta (BBA)/Protein Struct. Mol.* **1246**(1), 98–105 (1995).
17. I. M. Bell, R. J. H. Clark, and P. J. Gibbs, "Raman spectroscopic library of natural and synthetic pigments (pre-~ 1850 AD)," *Spectrochim. Acta - Part A Mol. Biomol. Spectrosc.* **53**(12), 2159–2179 (1997).

18. R. J. H. Clark and P. J. Gibbs, "Identification of lead(II) sulfide and pararealgar on a 13th century manuscript by Raman microscopy," *Chem. Commun.* (11), 1003–1004 (1997).
19. G. D. Smith and R. J. H. Clark, "The role of H₂S in pigment blackening," *J. Cult. Herit.* **3**(2), 101–105 (2002).
20. L. Burgio, R. J. H. Clark, and S. Firth, "Raman spectroscopy as a means for the identification of plattnerite (PbO₂), of lead pigments and of their degradation products," *Analyst* **126**(2), 222–227 (2001).
21. P. Vandenabeele, F. Verpoort, and L. Moens, "Non-destructive analysis of paintings using fourier transform Raman spectroscopy with fibre optics," *J. Raman Spectrosc.* **32**(4), 263–269 (2001).
22. P. Vandenabeele, T. L. Weis, E. R. Grant, and L. J. Moens, "A new instrument adapted to in situ Raman analysis of objects of art," *Anal. Bioanal. Chem.* **379**(1), 137–142 (2004).
23. P. Colomban, "The on-site/remote Raman analysis with mobile instruments: A review of drawbacks and success in cultural heritage studies and other associated fields," *J. Raman Spectrosc.* **43**(11), 1529–1535 (2012).
24. A. Rousaki and P. Vandenabeele, "In situ Raman spectroscopy for cultural heritage studies," *J. Raman Spectrosc.* **52**(12), 2178–2189 (2021).
25. D. A. Leonard, "Observation of Raman scattering from the atmosphere using a pulsed nitrogen ultraviolet laser," *Nature* **216**(5111), 142 (1967).

26. J. Cooney, J. Orr, and C. Tomasetti, "Measurements separating the gaseous and aerosol components of laser atmospheric backscatter," *Nature* **224**(5224), 1098 (1969).
27. R. L. McCreery, M. Fleischmann, and P. Hendra, "Fiber Optic Probe for Remote Raman Spectrometry," *Anal. Chem.* **55**(1), 146–148 (1983).
28. J. D. Stopar, P. G. Lucey, S. K. Sharma, A. K. Misra, G. J. Taylor, and H. W. Hubble, "Raman efficiencies of natural rocks and minerals: Performance of a remote Raman system for planetary exploration at a distance of 10 meters," *Spectrochim. Acta - Part A Mol. Biomol. Spectrosc.* **61**(10), 2315–2323 (2005).
29. M. W. Sandford, A. K. Misra, T. E. Acosta-Maeda, S. K. Sharma, J. N. J. N. Porter, M. J. Egan, N. Abedin, M. N. Abedin, and N. Abedin, "Detecting Minerals and Organics Relevant to Planetary Exploration Using a Compact Portable Remote Raman System at 122 Meters," *Appl. Spectrosc.* **75**(3), 000370282094366 (2021).
30. T. E. Acosta-Maeda, A. K. Misra, L. G. Muzangwa, G. Berlanga, D. Muchow, J. Porter, and S. K. Sharma, "Remote Raman measurements of minerals, organics, and inorganics at 430 m range," *Appl. Opt.* **55**(36), 10283 (2016).
31. A. K. Misra, T. E. Acosta-Maeda, J. N. Porter, M. J. Egan, M. W. Sandford, T. Oyama, and J. Zhou, "Remote Raman Detection of Chemicals from 1752 m During Afternoon Daylight.," *Appl. Spectrosc.* **74**(2), 233–240 (2020).
32. S. K. Sharma, A. K. Misra, and B. Sharma, "Portable remote Raman system for monitoring hydrocarbon, gas hydrates and explosives in the environment," *Spectrochim. Acta - Part A Mol. Biomol. Spectrosc.* **61**(10), 2404–2412 (2005).

33. M. Gaft and L. Nagli, "UV gated Raman spectroscopy for standoff detection of explosives," *Opt. Mater. (Amst)*. **30**(11), 1739–1746 (2008).
34. H. Östmark, M. Nordberg, and T. E. Carlsson, "Stand-off detection of explosives particles by multispectral imaging Raman spectroscopy," *Appl. Opt.* **50**(28), 5592–5599 (2011).
35. S. M. Angel, N. R. Gomer, S. K. Sharma, C. McKay, and N. Ames, "Remote Raman spectroscopy for planetary exploration: A review," *Appl. Spectrosc.* **66**(2), 137–150 (2012).
36. F. Rull, A. Vegas, A. Sansano, and P. Sobron, "Analysis of Arctic ices by Remote Raman Spectroscopy," *Spectrochim. Acta - Part A Mol. Biomol. Spectrosc.* **80**(1), 148–155 (2011).
37. R. C. Wiens, S. Maurice, S. H. Robinson, A. E. Nelson, P. Cais, P. Bernardi, R. T. Newell, S. Clegg, S. K. Sharma, S. Storms, J. Deming, D. Beckman, A. M. Ollila, O. Gasnault, R. B. Anderson, Y. André, S. Michael Angel, G. Arana, E. Auden, P. Beck, J. Becker, K. Benzerara, S. Bernard, O. Beyssac, L. Borges, B. Bousquet, K. Boyd, M. Caffrey, J. Carlson, K. Castro, J. Celis, B. Chide, K. Clark, E. Cloutis, E. C. Cordoba, A. Cousin, M. Dale, L. Deflores, D. Delapp, M. Deleuze, M. Dirmyer, C. Donny, G. Dromart, M. George Duran, M. Egan, J. Ervin, C. Fabre, A. Fau, W. Fischer, O. Forni, T. Fouchet, R. Fresquez, J. Frydenvang, D. Gasway, I. Gontijo, J. Grotzinger, X. Jacob, S. Jacquino, J. R. Johnson, R. A. Klisiewicz, J. Lake, N. Lanza, J. Laserna, J. Lasue, S. Le Mouélic, C. Legett, R. Leveille, E. Lewin, G. Lopez-Reyes, R. Lorenz, E. Lorigny, S. P. Love, B. Lucero, J. M. Madariaga, M. Madsen, S. Madsen, N. Mangold, J. A. Manrique, J. P. Martinez, J. Martinez-Frias, K. P. McCabe, T. H. McConnochie, J. M. McGlown, S. M.

- McLennan, N. Melikechi, P. Y. Meslin, J. M. Michel, D. Mimoun, A. Misra, G. Montagnac, F. Montmessin, V. Mousset, N. Murdoch, H. Newsom, L. A. Ott, Z. R. Ousnamer, L. Pares, Y. Parot, R. Pawluczyk, C. Glen Peterson, P. Pilleri, P. Pinet, G. Pont, F. Poulet, C. Provost, B. Quertier, H. Quinn, W. Rapin, J. M. Reess, A. H. Regan, A. L. Reyes-Newell, P. J. Romano, C. Royer, F. Rull, B. Sandoval, J. H. Sarrao, V. Sautter, M. J. Schoppers, S. Schröder, D. Seitz, T. Shepherd, P. Sobron, B. Dubois, V. Sridhar, M. J. Toplis, I. Torre-Fdez, I. A. Trettel, M. Underwood, A. Valdez, J. Valdez, D. Venhaus, and P. Willis, "The SuperCam Instrument Suite on the NASA Mars 2020 Rover: Body Unit and Combined System Tests," *Space Sci. Rev.* **217**(1), 4 (2021).
38. N. Altangerel, G. O. Ariunbold, C. Gorman, M. H. Alkahtani, E. J. Borrego, D. Bohlmeier, P. Hemmer, M. V. Kolomiets, J. S. Yuan, and M. O. Scully, "In vivo diagnostics of early abiotic plant stress response via Raman spectroscopy," *Proc. Natl. Acad. Sci. U. S. A.* **114**(13), 3393–3396 (2017).
39. A. Brambilla, I. Osticioli, A. Nevin, D. Comelli, C. Dandrea, C. Lofrumento, G. Valentini, and R. Cubeddu, "A remote scanning Raman spectrometer for in situ measurements of works of art," *Rev. Sci. Instrum.* **82**(6), 063109 (2011).
40. A. K. Misra, S. K. Sharma, and P. G. Lucey, "Remote Raman spectroscopic detection of minerals and organics under illuminated conditions from a distance of 10 m using a single 532 nm laser pulse," *Appl. Spectrosc.* **60**(2), 223–228 (2006).
41. S. K. Sharma, A. K. Misra, T. E. Acosta, P. G. Lucey, and M. N. Abedin, "Compact time-resolved remote Raman system for detection of anhydrous and hydrous minerals and ices for planetary exploration," in *Space Missions and Technologies*, J. L. Cox, M. G. Bester, and W. Fink, eds. (2010), **7691**, p. 76910F.

42. G. Berlanga, T. E. Acosta-Maeda, S. K. Sharma, J. N. Porter, P. Dera, H. Shelton, G. J. Taylor, and A. K. Misra, "Remote Raman spectroscopy of natural rocks," *Appl. Opt.* **58**(32), 8971 (2019).
43. V. Spizzichino and R. Fantoni, "Laser Induced Breakdown Spectroscopy in archeometry: A review of its application and future perspectives," *Spectrochim. Acta Part B At. Spectrosc.* **99**, 201–209 (2014).
44. A. Botto, B. Campanella, S. Legnaioli, M. Lezzerini, G. Lorenzetti, S. Pagnotta, F. Poggialini, and V. Palleschi, "Applications of laser-induced breakdown spectroscopy in cultural heritage and archaeology: A critical review," *J. Anal. At. Spectrom.* **34**(1), 81–103 (2019).
45. D. Anglos, "Laser-induced breakdown spectroscopy in heritage science," *Phys. Sci. Rev.* **4**(7), (2019).
46. V. Lazic, L. Caneve, F. Colao, R. Fantoni, L. Fornarini, and V. Spizzichino, "Quantitative elemental analyses of archaeological materials by laser-induced breakdown spectroscopy (LIBS): an overview," in *Optical Methods for Arts and Archaeology*, R. Salimbeni and L. Pezzati, eds. (2005), **5857**, p. 58570H.
47. J. Rakovský, P. Čermák, O. Musset, and P. Veis, "A review of the development of portable laser induced breakdown spectroscopy and its applications," *Spectrochim. Acta - Part B At. Spectrosc.* **101**, 269–287 (2014).
48. P. Vandenaabeele and M. K. Donais, "Mobile spectroscopic instrumentation in archaeometry research," *Appl. Spectrosc.* **70**(1), 27–41 (2016).

49. G. S. Senesi, R. S. Harmon, and R. R. Hark, "Field-portable and handheld LIBS: Historical review, current status and future prospects," *Spectrochim. Acta Part B At. Spectrosc.* **175**, 106013 (2020).
50. J. L. Gottfried, F. C. De Lucia, C. A. Munson, and A. W. Miziolek, "Double-pulse standoff laser-induced breakdown spectroscopy for versatile hazardous materials detection," *Spectrochim. Acta - Part B At. Spectrosc.* **62**(12), 1405–1411 (2007).
51. F. C. De Lucia, J. L. Gottfried, C. A. Munson, and A. W. Miziolek, "Multivariate analysis of standoff laser-induced breakdown spectroscopy spectra for classification of explosive-containing residues," *Appl. Opt.* **47**(31), G112 (2008).
52. C. López-Moreno, S. Palanco, J. J. Laserna, F. DeLucia, A. W. Miziolek, J. Rose, R. A. Walters, and A. I. Whitehouse, "Test of a stand-off laser-induced breakdown spectroscopy sensor for the detection of explosive residues on solid surfaces," *J. Anal. At. Spectrom.* **21**(1), 55–60 (2006).
53. R. González, P. Lucena, L. M. Tobaría, and J. J. Laserna, "Standoff LIBS detection of explosive residues behind a barrier," *J. Anal. At. Spectrom.* **24**(8), 1123–1126 (2009).
54. R. C. Wiens, S. Maurice, B. Barraclough, M. Saccoccio, W. C. Barkley, J. F. Bell, S. Bender, J. Bernardin, D. Blaney, J. Blank, M. Bouyé, N. Bridges, N. Bultman, P. Caïs, R. C. Clanton, B. Clark, S. Clegg, A. Cousin, D. Cremers, A. Cros, L. Deflores, D. Delapp, R. Dingler, C. D'Uston, M. Darby Dyar, T. Elliott, D. Enemark, C. Fabre, M. Flores, O. Forni, O. Gasnault, T. Hale, C. Hays, K. Herkenhoff, E. Kan, L. Kirkland, D. Kouach, D. Landis, Y. Langevin, N. Lanza, F. Larocca, J. Lasue, J. Latino, D. Limonadi, C. Lindensmith, C. Little, N. Mangold, G. Manhes, P. Mauchien, C. McKay, E. Miller, J. Mooney, R. V. Morris, L.

- Morrison, T. Nelson, H. Newsom, A. Ollila, M. Ott, L. Pares, R. Perez, F. Poitrasson, C. Provost, J. W. Reiter, T. Roberts, F. Romero, V. Sautter, S. Salazar, J. J. Simmonds, R. Stiglich, S. Storms, N. Striebig, J. J. Thocaven, T. Trujillo, M. Ulibarri, D. Vaniman, N. Warner, R. Waterbury, R. Whitaker, J. Witt, and B. Wong-Swanson, "The ChemCam instrument suite on the Mars Science Laboratory (MSL) rover: Body unit and combined system tests," *Space Sci. Rev.* **170**(1–4), 167–227 (2012).
55. R. B. Anderson, O. Forni, A. Cousin, R. C. Wiens, S. M. Clegg, J. Frydenvang, T. S. J. Gabriel, A. Ollila, S. Schröder, O. Beyssac, E. Gibbons, D. S. Vogt, E. Clavé, J.-A. Manrique, I. V. Carey Legett, P. Pilleri, R. T. Newell, J. Sarrao, S. Maurice, G. Arana, K. Benzerara, P. Bernardi, S. Bernard, B. Bousquet, A. J. Brown, C. Alvarez-Llamas, B. Chide, E. Cloutis, J. Comellas, S. Connell, E. Dehouck, D. M. Delapp, A. Essunfeld, C. Fabre, T. Fouchet, C. Garcia-Florentino, L. García-Gómez, P. Gasda, O. Gasnault, E. M. Hausrath, N. L. Lanza, J. Laserna, J. Lasue, G. Lopez, J. M. Madariaga, L. Mandon, N. Mangold, P.-Y. Meslin, A. E. Nelson, H. Newsom, A. L. Reyes-Newell, S. Robinson, F. Rull, S. Sharma, J. I. Simon, P. Sobron, I. T. Fernandez, A. Udry, D. Venhaus, S. M. McLennan, R. V. Morris, and B. Ehlmann, "Post-landing major element quantification using SuperCam laser induced breakdown spectroscopy," *Spectrochim. Acta Part B At. Spectrosc.* 106347 (2021).
56. O. Kokkinaki, A. Klini, M. Polychronaki, N. C. Mavrikakis, K. G. Siderakis, E. Koudoumas, D. Pylarinos, E. Thalassinakis, K. Kalpouzios, and D. Anglos, "Assessing the type and quality of high voltage composite outdoor insulators by remote laser-induced breakdown spectroscopy analysis: A feasibility study," *Spectrochim. Acta - Part B At. Spectrosc.* **165**(October 2019), 105768 (2020).

57. A. Lang, D. Engelberg, N. T. Smith, D. Trivedi, O. Horsfall, A. Banford, P. A. Martin, P. Coffey, W. R. Bower, C. Walther, M. Weiß, H. Bosco, A. Jenkins, and G. T. W. Law, "Analysis of contaminated nuclear plant steel by laser-induced breakdown spectroscopy," *J. Hazard. Mater.* **345**, 114–122 (2018).
58. R. Grönlund, M. Lundqvist, and S. Svanberg, "Remote imaging laser-induced breakdown spectroscopy and laser-induced fluorescence spectroscopy using nanosecond pulses from a mobile lidar system," *Appl. Spectrosc.* **60**(8), 853–859 (2006).
59. I. Gaona, P. Lucena, J. Moros, F. J. Fortes, S. Guirado, J. Serrano, and J. J. Laserna, "Evaluating the use of standoff LIBS in architectural heritage: Surveying the Cathedral of Málaga," *J. Anal. At. Spectrom.* **28**(6), 810–820 (2013).
60. V. Lazic, A. Trujillo-Vazquez, H. Sobral, C. Márquez, A. Palucci, M. Ciaffi, and M. Pistilli, "Corrections for variable plasma parameters in laser induced breakdown spectroscopy: Application on archeological samples," *Spectrochim. Acta - Part B At. Spectrosc.* **122**, 103–113 (2016).
61. S. Guirado, F. J. Fortes, and J. J. Laserna, "Elemental analysis of materials in an underwater archeological shipwreck using a novel remote laser-induced breakdown spectroscopy system," *Talanta* **137**, 182–188 (2015).
62. F. J. Fortes, S. Guirado, A. Metzinger, and J. J. Laserna, "A study of underwater stand-off laser-induced breakdown spectroscopy for chemical analysis of objects in the deep ocean," *J. Anal. At. Spectrom.* **30**(5), 1050–1056 (2015).
63. M. López-Claros, F. J. Fortes, and J. J. Laserna, "Subsea spectral identification of shipwreck objects using laser-induced breakdown spectroscopy and linear discriminant analysis," *J. Cult. Herit.* **29**, 75–81 (2018).

64. E. Pospíšilová, K. Novotný, P. Pořízka, D. Hradil, J. Hradilová, J. Kaiser, and V. Kanický, "Depth-resolved analysis of historical painting model samples by means of laser-induced breakdown spectroscopy and handheld X-ray fluorescence," *Spectrochim. Acta - Part B At. Spectrosc.* **147**, 100–108 (2018).
65. E. A. Kaszewska, M. Sylwestrzak, J. Marczak, W. Skrzeczanowski, M. Iwanicka, E. Szmit-Naud, D. Anglos, and P. Targowski, "Depth-resolved multilayer pigment identification in paintings: Combined use of laser-induced breakdown spectroscopy (LIBS) and optical coherence tomography (OCT)," *Appl. Spectrosc.* **67**(8), 960–972 (2013).
66. R. Bruder, V. Detalle, and C. Coupry, "An example of the complementarity of laser-induced breakdown spectroscopy and Raman microscopy for wall painting pigments analysis," *J. Raman Spectrosc.* **38**(7), 909–915 (2007).
67. B. Chide, O. Beyssac, M. Gauthier, K. Benzerara, I. Estève, J. C. Boulliard, S. Maurice, and R. C. Wiens, "Acoustic monitoring of laser-induced phase transitions in minerals: implication for Mars exploration with SuperCam," *Sci. Rep.* **11**(1), (2021).
68. X. Ren, T. Cai, D. Liu, J. Liu, H. Zhang, Q. Fu, Z. Zhang, and W. Xu, "Preliminary Scientific Exploration Programs for Mars Surface Composition Detection Package of China's First Mars Exploration," in *European Planetary Science Congress 2018, Held 16-21 September 2018 at TU Berlin, Berlin, Germany, Id.EPSC2018-759* (2018), **12**, pp. 2–3.
69. A. Nevin, G. Spoto, and D. Anglos, "Laser spectroscopies for elemental and molecular analysis in art and archaeology," *Appl. Phys. A Mater. Sci. Process.* **106**(2), 339–361 (2012).

70. T. Miyoshi, M. Ikeya, S. Kinoshita, and T. Kushida, "Laser-Induced fluorescence of oil colours and its application to the identification of pigments in oil paintings," *Jpn. J. Appl. Phys.* **21**(7), 1032–1036 (1982).
71. D. Anglos, M. Solomidou, I. Zergioti, V. Zafiropulos, T. G. Papazoglou, and C. Fotakis, "Laser-Induced Fluorescence in Artwork Diagnostics: An Application in Pigment Analysis," *Appl. Spectrosc.* **50**(10), 1331–1334 (1996).
72. G. Cecchi, L. Pantani, V. Raimondi, L. Tomaselli, G. Lamenti, P. Tiano, and R. Chiari, "Fluorescence lidar technique for the remote sensing of stone monuments," *J. Cult. Herit.* **1**(1), 29–36 (2000).
73. L. Pantani, G. Ballerini, G. Cecchi, H. Edner, D. Lognoli, T. Johansson, V. Raimondi, S. Svanberg, P. Tiano, L. Tomaselli, and P. Weibring, "Experiments on stony monument monitoring by laser-induced fluorescence," *J. Cult. Herit.* **1**(2), S345–S348 (2000).
74. V. Spizzichino, L. Bertani, L. Caneve, and M. F. Caso, "Rapid analysis of marble treatments by laser induced fluorescence," *Opt. Quantum Electron.* **52**(2), 117 (2020).
75. V. Lazic, F. Colao, R. Fantoni, A. Palucci, V. Spizzichino, I. Borgia, B. G. Brunetti, and A. Sgamellotti, "Characterisation of lustre and pigment composition in ancient pottery by laser induced fluorescence and breakdown spectroscopy," *J. Cult. Herit.* **4**(SUPPL. 1), 303–308 (2003).
76. R. Fantoni, L. Caneve, F. Colao, L. Fiorani, A. Palucci, R. Dell'Erba, and V. Fassina, "Laser-induced fluorescence study of medieval frescoes by Giusto de' Menabuoi," *J. Cult. Herit.* **14**(3 SUPPL), S59–S65 (2013).

77. M. Romani, G. Capobianco, L. Pronti, F. Colao, C. Seccaroni, A. Puiu, A. C. Felici, G. Verona-Rinati, M. Cestelli-Guidi, A. Tognacci, M. Vendittelli, M. Mangano, A. Acconci, G. Bonifazi, S. Serranti, M. Marinelli, and R. Fantoni, "Analytical chemistry approach in cultural heritage: the case of Vincenzo Pasqualoni's wall paintings in S. Nicola in Carcere (Rome)," *Microchem. J.* **156**, 104920 (2020).
78. E. W. Chappelle, F. M. Wood, J. E. McMurtrey, and W. W. Newcomb, "Laser-induced fluorescence of green plants 1: A technique for the remote detection of plant stress and species differentiation," *Appl. Opt.* **23**(1), 134 (1984).
79. E. W. Chappelle, J. E. McMurtrey, F. M. Wood, and W. W. Newcomb, "Laser-induced fluorescence of green plants 2: LIF caused by nutrient deficiencies in corn," *Appl. Opt.* **23**(1), 139 (1984).
80. E. W. Chappelle, F. M. Wood, W. Wayne Newcomb, and J. E. McMurtrey, "Laser-induced fluorescence of green plants 3: LIF spectral signatures of five major plant types," *Appl. Opt.* **24**(1), 74 (1985).
81. E. W. Chappelle, J. E. McMurtrey, and M. S. Kim, "Identification of the pigment responsible for the blue fluorescence band in the laser induced fluorescence (LIF) spectra of green plants, and the potential use of this band in remotely estimating rates of photosynthesis," *Remote Sens. Environ.* **36**(3), 213–218 (1991).
82. J. H. & K. B. R. Grönlund, M. Bengtsson, M. Sjöholm, G. Somesfalean, T. Johansson, P. Weibring, H. Edner, S. Svanberg, "Lidar remote-sensing assessment of the cultural heritage using laser-induced fluorescence and laser-induced breakdown spectroscopy," in *Air Pollution and Cultural Heritage*, 1st ed. (CRC Press, 2004), pp. 179–182.

83. R. Grönlund, J. Hällström, A. Johansson, K. Barup, and S. Svanberg, "Remote multicolor excitation laser-induced fluorescence imaging," *Laser Chem.* **2006**, 1–6 (2006).
84. R. Grönlund, J. Hällström, S. Svanberg, and K. Barup, "Fluorescence Lidar Multispectral Imaging for Diagnosis of Historical Monuments, Övedskloster: A Swedish Case Study," in *Lasers in the Conservation of Artworks* (Springer Berlin Heidelberg, 2007), pp. 583–591.
85. J. Hällström, K. Barup, R. Grönlund, A. Johansson, S. Svanberg, L. Palombi, D. Lognoli, V. Raimondi, G. Cecchi, and C. Conti, "Documentation of soiled and biodeteriorated facades: A case study on the Coliseum, Rome, using hyperspectral imaging fluorescence lidars," *J. Cult. Herit.* **10**(1), 106–115 (2009).
86. L. Palombi, D. Lognoli, V. Raimondi, G. Cecchi, J. Hällström, K. Barup, C. Conti, R. Grönlund, A. Johansson, and S. Svanberg, "Hyperspectral fluorescence lidar imaging at the Colosseum, Rome: Elucidating past conservation interventions," *Opt. Express* **16**(10), 6794 (2008).
87. J. Moros, J. A. Lorenzo, P. Lucena, L. Miguel Tobaría, and J. J. Laserna, "Simultaneous Raman Spectroscopy–Laser-Induced Breakdown Spectroscopy for instant standoff analysis of explosives using a mobile integrated sensor platform," *Anal. Chem.* **82**(4), 1389–1400 (2010).
88. J. Moros, J. A. Lorenzo, and J. J. Laserna, "Standoff detection of explosives: Critical comparison for ensuing options on Raman spectroscopy-LIBS sensor fusion," *Anal. Bioanal. Chem.* **400**(10), 3353–3365 (2011).

89. J. Moros and J. J. Laserna, "New Raman-laser-induced breakdown spectroscopy identity of explosives using parametric data fusion on an integrated sensing platform," *Anal. Chem.* **83**(16), 6275–6285 (2011).
90. R. C. Wiens, S. K. Sharma, J. Thompson, A. Misra, and P. G. Lucey, "Joint analyses by laser-induced breakdown spectroscopy (LIBS) and Raman spectroscopy at stand-off distances," *Spectrochim. Acta - Part A Mol. Biomol. Spectrosc.* **61**(10), 2324–2334 (2005).
91. S. K. Sharma, A. K. Misra, P. G. Lucey, R. C. Wiens, and S. M. Clegg, "Combined remote LIBS and Raman spectroscopy at 8.6 m of sulfur-containing minerals, and minerals coated with hematite or covered with basaltic dust," *Spectrochim. Acta - Part A Mol. Biomol. Spectrosc.* **68**(4), 1036–1045 (2007).
92. S. K. Sharma, A. K. Misra, P. G. Lucey, and R. C. F. Lentz, "A combined remote Raman and LIBS instrument for characterizing minerals with 532 nm laser excitation," *Spectrochim. Acta Part A Mol. Biomol. Spectrosc.* **73**(3), 468–476 (2009).
93. A. K. Misra, B. Chee, D. Muchow, G. Berlanga, J. N. Porter, S. K. Sharma, and T. E. Acosta-Maeda, "A Two Components Approach for Long Range Remote Raman and Laser-Induced Breakdown (LIBS) Spectroscopy Using Low Laser Pulse Energy," *Appl. Spectrosc. Vol. 73, Issue 3, pp. 320-328* **73**(3), 320–328 (2019).
94. M. Hoehse, D. Mory, S. Florek, F. Weritz, I. Gornushkin, and U. Panne, "A combined laser-induced breakdown and Raman spectroscopy Echelle system for elemental and molecular microanalysis," *Spectrochim. Acta - Part B At. Spectrosc.* **64**(11–12), 1219–1227 (2009).

95. K. M. M. Muhammed Shameem, V. S. S. Dhanada, S. Harikrishnan, S. D. George, V. B. B. Kartha, C. Santhosh, and V. K. K. Unnikrishnan, "Echelle LIBS-Raman system: A versatile tool for mineralogical and archaeological applications," *Talanta* **208**, 120482 (2020).
96. D. Anglos, "Laser-induced breakdown spectroscopy in art and archaeology," *Appl. Spectrosc.* **55**(6), 186A-205A (2001).
97. P. Pouli, K. Melessanaki, A. Giakoumaki, V. Argyropoulos, and D. Anglos, "Measuring the thickness of protective coatings on historic metal objects using nanosecond and femtosecond laser induced breakdown spectroscopy depth profiling," *Spectrochim. Acta - Part B At. Spectrosc.* **60**(7–8), 1163–1171 (2005).
98. R. Grönlund, M. Lundqvist, and S. Svanberg, "Remote imaging laser-induced breakdown spectroscopy and remote cultural heritage ablative cleaning," *Opt. Lett.* **30**(21), 2882 (2005).
99. S. K. Sharma, S. Ismail, S. M. Angel, P. G. Lucey, C. P. McKay, A. K. Misra, P. J. Mougini-Mark, H. Newsom, E. R. D. Scott, U. N. Singh, and G. J. Taylor, "Remote Raman and laser-induced fluorescence (RLIF) emission instrument for detection of mineral, organic, and biogenic materials on Mars to 100 meters radial distance," in *Instruments, Science, and Methods for Geospace and Planetary Remote Sensing*, C. A. Nardell, P. G. Lucey, J.-H. Yee, and J. B. Garvin, eds. (2004), **5660**, p. 128.
100. B. J. Bozlee, A. K. Misra, S. K. Sharma, and M. Ingram, "Remote Raman and fluorescence studies of mineral samples," in *Spectrochimica Acta - Part A: Molecular and Biomolecular Spectroscopy* (Elsevier, 2005), **61**(10), pp. 2342–2348.

101. I. Osticioli, N. F. C. Mendes, A. Nevin, A. Zoppi, C. Lofrumento, M. Becucci, and E. M. Castellucci, "A new compact instrument for Raman, laser-induced breakdown, and laser-induced fluorescence spectroscopy of works of art and their constituent materials," *Rev. Sci. Instrum.* **80**(7), 076109 (2009).
102. A. Martínez-Hernández, M. Oujja, M. Sanz, E. Carrasco, V. Detalle, and M. Castillejo, "Analysis of heritage stones and model wall paintings by pulsed laser excitation of Raman, laser-induced fluorescence and laser-induced breakdown spectroscopy signals with a hybrid system," *J. Cult. Herit.* **32**, 1–8 (2018).
103. V. Detalle, X. Bai, E. Bourguignon, M. Menu, and I. Pallot-Frossard, "LIBS-LIF-Raman: a new tool for the future E-RIHS," in *Optics for Arts, Architecture, and Archaeology VI* (International Society for Optics and Photonics, 2017), **10331**, p. 103310N.
104. D. Syvilay, X. S. Bai, N. Wilkie-Chancellor, A. Texier, L. Martinez, S. Serfaty, and V. Detalle, "Laser-induced emission, fluorescence and Raman hybrid setup: A versatile instrument to analyze materials from cultural heritage," *Spectrochim. Acta - Part B At. Spectrosc.* **140**, 44–53 (2018).
105. X. Bai, M. Oujja, M. Sanz, M. Lopez, C. L. Koch Dandolo, M. Castillejo, and V. Detalle, "Integrating LIBS LIF Raman into a single multi-spectroscopic mobile device for in situ cultural heritage analysis," in *Optics for Arts, Architecture, and Archaeology VII*, P. Targowski, R. Groves, and H. Liang, eds. (SPIE, 2019), p. 43.
106. P. Vandenaabeele, H. G. M. Edwards, and J. Jehlička, "The role of mobile instrumentation in novel applications of Raman spectroscopy: Archaeometry, geosciences, and forensics," *Chem. Soc. Rev.* **43**(8), 2628–2649 (2014).

107. S. P. Best, R. J. H. Clark, and R. Withnall, "Non-destructive pigment analysis of artefacts by Raman microscopy," *Endeavour* **16**(2), 66–73 (1992).
108. R. J. H. Clark, "Raman microscopy: application to the identification of pigments on medieval manuscripts," *Chem. Soc. Rev.* **24**(3), 187 (1995).
109. M. Pérez-Alonso, K. Castro, and J. M. Madariaga, "Investigation of degradation mechanisms by portable Raman spectroscopy and thermodynamic speciation: The wall painting of Santa María de Lemoniz (Basque Country, North of Spain)," *Anal. Chim. Acta* **571**(1), 121–128 (2006).
110. L. Bellot-Gurlet, F.-X. Le Bourdonnec, G. Poupeau, and S. Dubernet, "Raman micro-spectroscopy of western Mediterranean obsidian glass: one step towards provenance studies?," *J. Raman Spectrosc.* **35**(89), 671–677 (2004).
111. B. I. Łydzba-Kopczyńska, B. Gediga, J. Chojcan, and M. Sachanbiński, "Provenance investigations of amber jewelry excavated in Lower Silesia (Poland) and dated back to Early Iron Age," *J. Raman Spectrosc.* **43**(11), 1839–1844 (2012).
112. Y. Li, C. S. Cheung, S. Kogou, F. Liggins, and H. Liang, "Standoff Raman spectroscopy for architectural interiors from 3-15 m distances," *Opt. Express* **27**(22), 31338 (2019).
113. S. K. Sharma, A. K. Misra, S. M. Clegg, J. E. Barefield, R. C. Wiens, T. E. Acosta, and D. E. Bates, "Remote-Raman spectroscopic study of minerals under supercritical CO₂ relevant to Venus exploration," *Spectrochim. Acta - Part A Mol. Biomol. Spectrosc.* **80**(1), 75–81 (2011).

114. A. Pettersson, I. Johansson, S. Wallin, M. Nordberg, and H. Östmark, "Near real-time standoff detection of explosives in a realistic outdoor environment at 55 m distance," *Propellants, Explos. Pyrotech.* **34**(4), 297–306 (2009).
115. S. K. Sharma, P. G. Lucey, M. Ghosh, H. W. Hubble, and K. A. Horton, "Stand-off Raman spectroscopic detection of minerals on planetary surfaces," *Spectrochim. Acta - Part A Mol. Biomol. Spectrosc.* **59**(10), 2391–2407 (2003).
116. R. L. Aggarwal, L. W. Farrar, and D. L. Polla, "Measurement of the absolute Raman scattering cross sections of sulfur and the standoff Raman detection of a 6-mm-thick sulfur specimen at 1500 m," *J. Raman Spectrosc.* **42**(3), 461–464 (2011).
117. H. Liang, R. Lange, B. Peric, and M. Spring, "Optimum spectral window for imaging of art with optical coherence tomography," *Appl. Phys. B Lasers Opt.* **111**(4), 589–602 (2013).
118. S. Kogou, A. Lucian, S. Bellesia, L. Burgio, K. Bailey, C. Brooks, and H. Liang, "A holistic multimodal approach to the non-invasive analysis of watercolour paintings," *Appl. Phys. A Mater. Sci. Process.* **121**(3), 999–1014 (2015).
119. L. Burgio and R. J. H. Clark, "Library of FT-Raman spectra of pigments, minerals, pigment media and varnishes, and supplement to existing library of Raman spectra of pigments with visible excitation," *Spectrochim. Acta - Part A Mol. Biomol. Spectrosc.* **57**(7), 1491–1521 (2001).
120. I. Osticioli, N. F. C. Mendes, A. Nevin, F. P. S. C. Gil, M. Becucci, and E. Castellucci, "Analysis of natural and artificial ultramarine blue pigments using laser induced breakdown and pulsed Raman spectroscopy, statistical analysis and light microscopy," *Spectrochim. Acta - Part A Mol. Biomol. Spectrosc.* **73**(3), 525–531 (2009).

121. S. Kogou, G. Shahtahmassebi, A. Lucian, H. Liang, B. Shui, W. Zhang, B. Su, and S. van Schaik, "From remote sensing and machine learning to the history of the Silk Road: large scale material identification on wall paintings," *Sci. Rep.* **10**(1), (2020).
122. A. Kramida, K. Olsen, and Y. Ralchenko, "NIST LIBS Database," <https://physics.nist.gov/PhysRefData/ASD/LIBS/lib-form.html>.
123. D. Anglos and J. C. Miller, "Cultural heritage applications of LIBS," in *Laser Induced Breakdown Spectroscopy* (Cambridge University Press, 2006), pp. 332–367.
124. C. S. Cheung, M. Spring, and H. Liang, "Ultra-high resolution Fourier domain optical coherence tomography for old master paintings," *Opt. Express* **23**(8), 10145 (2015).
125. G. Burns, "The Covalent Bond," in *Solid State Physics* (Academic Press, 1985), pp. 147–186.
126. A. De Santis, E. Mattei, and C. Pelosi, "Micro-Raman and stratigraphic studies of the paintings on the 'Cembalo' model musical instrument (A.D. 1650) and laser-induced degradation of the detected pigments," *J. Raman Spectrosc.* **38**(10), 1368–1378 (2007).
127. R. Mulholland, D. Howell, A. Beeby, C. E. Nicholson, and K. Domoney, "Identifying eighteenth century pigments at the Bodleian library using in situ Raman spectroscopy, XRF and hyperspectral imaging," *Herit. Sci.* **5**(1), 43 (2017).

128. E. Mattei, G. de Vivo, A. De Santis, C. Gaetani, C. Pelosi, and U. Santamaria, "Raman spectroscopic analysis of azurite blackening," *J. Raman Spectrosc.* **39**(2), 302–306 (2008).
129. J. Yu, W. S. Warren, and M. C. Fischer, "Visualization of vermilion degradation using pump-probe microscopy," *Sci. Adv.* **5**(6), eaaw3136 (2019).
130. H. Liang, R. Lange, A. Lucian, P. Hyndes, J. H. Townsend, and S. Hackney, "Development of portable microfading spectrometers for measurement of light sensitivity of materials," in *ICOM-CC 16th Triennial Conference Lisbon 19-23 September 2011: Preprints* (2011), pp. 19–23.
131. G. D. Smith, L. Burgio, S. Firth, and R. J. H. Clark, "Laser-induced degradation of lead pigments with reference to Botticelli's *Trionfo d'Amore*," *Anal. Chim. Acta* **440**(2), 185–188 (2001).
132. G. Moretti and C. Gervais, "Raman spectroscopy of the photosensitive pigment Prussian blue," *J. Raman Spectrosc.* **49**(7), 1198–1204 (2018).
133. A. Philippidis, A. Mikallou, and D. Anglos, "Determining optimum irradiation conditions for the analysis of vermilion by Raman spectroscopy," *Eur. Phys. J. Plus* 2021 13611 **136**(11), 1–15 (2021).
134. H. Liang, M. Mari, C. S. Cheung, S. Kogou, P. Johnson, and G. Filippidis, "Optical coherence tomography and non-linear microscopy for paintings – a study of the complementary capabilities and laser degradation effects," *Opt. Express* **25**(16), 19640 (2017).

135. A. Lerwill, A. Brookes, J. H. Townsend, S. Hackney, and H. Liang, "Micro-fading spectrometry: investigating the wavelength specificity of fading," *Appl. Phys. A Mater. Sci. Process.* **118**(2), 457–463 (2015).
136. Y. Li, C. S. Cheung, S. Kogou, A. Hogg, H. Liang, and S. Evans, "Standoff laser spectroscopy for wall paintings, monuments and architectural interiors," in *Transcending Boundaries: Integrated Approaches to Conservation. ICOM-CC 19th Triennial Conference Preprints* (2021).
137. M. R. Luo, G. Cui, and B. Rigg, "The development of the CIE 2000 colour-difference formula: CIEDE2000," *Color Res. Appl.* **26**(5), 340–350 (2001).
138. A.R. Robertson, H. Terstiege, and J.F. Verrill, *CIE Standard Illuminants for Colorimetry* (1999).
139. M. M. Cummins, *Nottingham Cathedral - a History of Catholic Nottingham*, Third Edit (Regeena Printing Ltd., 1994).
140. M. Vagnini, C. Miliani, L. Cartechini, P. Rocchi, B. G. Brunetti, and A. Sgamellotti, "FT-NIR spectroscopy for non-invasive identification of natural polymers and resins in easel paintings," *Anal. Bioanal. Chem.* **395**(7), 2107–2118 (2009).
141. M. de Keijzer, "The history of modern synthetic inorganic and organic artists' pigments," *Contrib. to Conserv. Res. Conserv. Netherlands Inst. Cult. Herit.* 42–54 (2002).
142. P.-L. Lee, E. Huang, and S.-C. Yu, "High-pressure Raman and X-ray studies of barite, BaSO₄," *High Press. Res.* **23**(4), 439–450 (2003).

143. A. Fairbrother, V. Izquierdo-Roca, X. Fontané, M. Ibáñez, A. Cabot, E. Saucedo, and A. Pérez-Rodríguez, "ZnS grain size effects on near-resonant Raman scattering: optical non-destructive grain size estimation," *CrystEngComm* **16**(20), 4120 (2014).
144. R. Capua, "The Obscure History of a Ubiquitous Pigment: Phosphorescent Lithopone and Its Appearance on Drawings By John La Farge," *J. Am. Inst. Conserv.* **53**(2), 75–88 (2014).
145. T. Brittain-Catlin, "A. W. N. Pugin's English convent plans," *J. Soc. Archit. Hist.* **65**(3), 356–377 (2006).
146. J. Taylor, "Treated Rutile Type Titanium Dioxide Pigments and their Properties," *J. Oil Colour Chem. Assoc.* **38**, 233–249 (1955).
147. N. C. Scherrer, Z. Stefan, D. Françoise, F. Annette, and K. Renate, "Synthetic organic pigments of the 20th and 21st century relevant to artist's paints: Raman spectra reference collection," *Spectrochim. Acta - Part A Mol. Biomol. Spectrosc.* **73**(3), 505–524 (2009).
148. H. de Diesbach and E. von der Weid, "Quelques sels complexes des o-dinitriles avec le cuivre et la pyridine," *Helv. Chim. Acta* **10**(1), 886–888 (1927).
149. M. de Keijzer, "Microchemical Analysis on Synthetic Organic Artists' Pigments Discovered in the Twentieth Century," in *ICOM Committee for Conservation, 9th Triennial Meeting, German Democratic Republic, 26-31 August 1990* (1990), pp. 220–225.

150. G. Shetty, C. Kendall, N. Shepherd, N. Stone, and H. Barr, "Raman spectroscopy: elucidation of biochemical changes in carcinogenesis of oesophagus," *Br. J. Cancer* **94**(10), 1460–1464 (2006).
151. A. Bonifacio, C. Beleites, F. Vittur, E. Marsich, S. Semeraro, S. Paoletti, and V. Sergo, "Chemical imaging of articular cartilage sections with Raman mapping, employing uni- and multi-variate methods for data analysis," *Analyst* **135**(12), 3193 (2010).
152. C. Krafft, T. Knetschke, A. Siegner, R. H. W. Funk, and R. Salzer, "Mapping of single cells by near infrared Raman microspectroscopy," *Vib. Spectrosc.* **32**(1), 75–83 (2003).
153. P. Ropret, C. Miliani, S. A. Centeno, Č. Tavzes, and F. Rosi, "Advances in Raman mapping of works of art," *J. Raman Spectrosc.* **41**(11), 1462–1467 (2010).
154. F. Casadio, C. Daher, and L. Bellot-Gurlet, *Raman Spectroscopy of Cultural Heritage Materials: Overview of Applications and New Frontiers in Instrumentation, Sampling Modalities, and Data Processing* (Springer, Cham, 2016), **374**(5), pp. 161–211.
155. *Meade Telescope Serial Command Protocol* (2010).
156. A. Loske, "The decorative scheme of the Royal Pavilion, Brighton: George IV's design ideas in the context of European colour theory, 1765 – 1845," (2014).
157. M. Steiger and S. Asmussen, "Crystallization of sodium sulfate phases in porous materials: The phase diagram Na₂SO₄-H₂O and the generation of stress," *Geochim. Cosmochim. Acta* **72**(17), 4291–4306 (2008).

158. L. Carlyle, "Authenticity and adulteration: What materials were 19th century artists really using?," *Conserv.* **17**(1), 56–60 (1993).
159. E. C. Eckel, *Cements, Limes, and Plasters: Their Materials, Manufacture, and Properties* (J. Wiley & Sons, 1907).
160. M. Steiger, "Salts and Crusts," in *The Effects of Air Pollution on the Built Environment. Air Pollution Reviews, Vol 2.* (Imperial College Press, 2003), pp. 133–181.
161. A. E. Charola, J. Pühringer, and M. Steiger, "Gypsum: A review of its role in the deterioration of building materials," *Environ. Geol.* **52**(2), 207–220 (2007).
162. S. Mosca, P. Dey, M. Salimi, B. Gardner, F. Palombo, N. Stone, and P. Matousek, "Spatially Offset Raman Spectroscopy - How Deep?," *Anal. Chem.* **93**(17), 6755–6762 (2021).
163. R. Glaus and D. W. Hahn, "Fiber-coupled laser-induced breakdown and Raman spectroscopy for flexible sample characterization with depth profiling capabilities," *Spectrochim. Acta - Part B At. Spectrosc.* **100**, 116–122 (2014).
164. Y. Lu, Y. Li, Y. Li, Y. Wang, S. Wang, Z. Bao, and R. Zheng, "Micro spatial analysis of seashell surface using laser-induced breakdown spectroscopy and Raman spectroscopy," *Spectrochim. Acta Part B At. Spectrosc.* **110**, 63–69 (2015).
165. I. Osticioli, N. F. C. C. Mendes, S. Porcinai, A. Cagnini, and E. Castellucci, "Spectroscopic analysis of works of art using a single LIBS and pulsed Raman setup," *Anal. Bioanal. Chem.* **394**(4), 1033–1041 (2009).
166. H. Liang, "Advances in multispectral and hyperspectral imaging for archaeology and art conservation," *Appl. Phys. A Mater. Sci. Process.* **106**(2), 309–323 (2012).

167. A. Schönemann and H. G. M. Edwards, "Raman and FTIR microspectroscopic study of the alteration of Chinese tung oil and related drying oils during ageing," *Anal. Bioanal. Chem.* 2011 4004 **400**(4), 1173–1180 (2011).
168. N. Eastaugh, V. Walsh, T. Chaplin, and R. Siddall, *Pigment Compendium: A Dictionary of Historical Pigments* (Routledge, 2007).
169. C. Coupry, J. Le Marec, J. Corset, A. Duval, C. Lahanier, J. P. Rioux, M. C. Papillon, and R. Lefèvre, "Analyses de pigments blancs appliquées à l'étude chronologique des peintures de chevalet-blanc de titane," in *ICOM Committee for Conservation: 8th Triennial Meeting, Sydney, Australia, 6-11 September, 1987. Preprints* (1987), **1**, pp. 25–32.
170. E. W. FitzHugh, ed., *Artists' Pigments: A Handbook of Their History and Characteristics, Volume 3* (National Gallery of Art, 1997).
171. L. A. Carlyle, *The Artist's Assistant: Oil Painting Instruction Manuals and Handbooks in Britain 1800-1900, with Reference to Selected Eighteenth-Century Sources* (2001).
172. J. Jehlička and A. Culka, "Critical evaluation of portable Raman spectrometers: From rock outcrops and planetary analogs to cultural heritage – A review," *Anal. Chim. Acta* **1209**, (2022).

Appendix 1

Pigment survey

The detection with the remote standoff Raman system of reference paint samples made of a range of common historic artist pigments are listed in Table A1. The acquisition time for detection is determined using the early version of the 780 nm CW remote standoff Raman system employing a collimated beam of ~4 mm at 4 m, the upgraded one will be more efficient. Most of the pigments not detected are organics, some green inorganic pigments, and Cd pigments [117].

Table A1. Detection of paint samples using the remote standoff Raman spectroscopy system.

No.	Pigment	Binding medium	Substrate	Minimum acquisition time for detection (s)
REDS				
1	Iron oxide	animal glue	chalk	600
2	Red lead	animal glue	chalk	5
3	Vermilion	animal glue	chalk	1
4	Realgar	animal glue	chalk	1
5	Lac	animal glue	paper	-
6	Sappanwood lake	egg tempera	glass slide	-
7	Madder lake	animal glue	paper	600
8	Cochineal	animal glue	paper	-
9	Safflower	animal glue	paper	-
10	Alizarin crimson	animal glue	paper	1800
11	Rose madder	egg tempera	glass slide	-
12	Cadmium red	egg tempera	chalk	-
13	Chrome red	egg tempera	chalk	1
YELLOWS				
14	Lead yellow	animal glue	chalk	1
15	Yellow ochre	animal glue	chalk	10
16	Gamboge	animal glue	paper	1800
17	Orpiment	animal glue	chalk	1
18	Weld lake	animal glue	paper	-
19	Quercitron lake	animal glue	paper	-
20	Buckthorn lake	animal glue	paper	-

21	Cadmium yellow (dark)	egg tempera	chalk	-
22	Cadmium yellow (light)	egg tempera	chalk	-
23	Chrome yellow (medium)	egg tempera	chalk	5
24	Cobalt yellow (Aureolin)	egg tempera	chalk	1
25	Lead tin yellow (light, type I)	egg tempera	chalk	10
26	Lemon yellow (barium chromate)	egg tempera	chalk	1
27	Naples yellow (light)	egg tempera	chalk	60
<hr/>				
GREENS				
28	Malachite	animal glue	chalk	-
29	Verdigris	animal glue	paper	-
30	Bavarian green earth	egg tempera	chalk	1800
31	Viridian green	egg tempera	chalk	-
32	Cobalt bottle green	egg tempera	chalk	60
33	Atacamite	animal glue	glass slide	-
34	Cobalt turquoise	egg tempera	chalk	60
35	Milori green	egg tempera	glass slide	10
36	Phthalo green	egg tempera	glass slide	1
<hr/>				
BLUES				
37	Indigo	animal glue	chalk	10
38	Azurite	animal glue	chalk	1800
39	Ultramarine	animal glue	paper	30
40	Cobalt blue	egg tempera	glass slide	600
41	Prussian blue	animal glue	glass slide	600
42	Smalt	animal glue	paper	600
43	Cerulean blue	egg tempera	chalk	60
44	Manganese blue	egg tempera	chalk	-
45	Phthalo blue	animal glue	glass slide	1
46	Milori blue	animal glue	glass slide	600
47	Maya blue	animal glue	glass slide	10
<hr/>				
PURPLES				
48	Cobalt violet (dark)	egg tempera	chalk	10
49	Cobalt violet (light)	egg tempera	chalk	10
50	Manganese violet	egg tempera	chalk	600
<hr/>				
WHITES				
51	White shell powder	animal glue	chalk	20
52	Lead white	egg tempera	glass slide	10
53	Gypsum	-	glass slide	5
54	Calcite	-	glass slide	10
55	Titanium white	egg tempera	chalk	1
56	Zinc white	linseed oil	glass slide	60
<hr/>				
BLACKS				
57	Bone black	egg tempera	chalk	1800
58	Charcoal (from beech)	egg tempera	chalk	1800

Appendix 2

Laser safety

At the beginning of this PhD project, the author has attended laser safety training courses organised by Public Health England and gained a certificate, before operating the laser sources. Risk assessments to identify the hazards and their associated risks have been conducted with regard to the operations of related laser instruments both in the laboratory environment and in field campaigns. The designated laser area in the lab is fully enclosed by black curtains to prevent the exposure to direct, scattered or reflected laser light. A warning sign indicating laser operations is placed at the entrance to the laser area. In cases where longer distances are required for remote experiments, the whole lab is enclosed with the door locked and windows curtained. A large board labelled with a warning sign is placed in front of the door.

The CW and pulsed laser sources used in our remote standoff Raman, LIBS and LIF systems are classified as Class 3B. For the 780/785 nm CW lasers used for Raman spectroscopy, their calculated irradiances are above the maximum permissible exposure (MPE) for the human eye. For the 1064 nm and 355 nm pulsed lasers for LIBS and LIF excitation respectively, the calculated irradiances exceed MPE of both the eye and the skin. Personal protective equipment (PPE) including laser safety goggles with appropriate optical density (OD), protective gloves, full face shields and laboratory coats is required to avoid the eye and skin exposure. It is worth noting that when laser alignment work is carried out either in the lab or *in situ*, the laser power is reduced significantly.

During the field campaigns, the space where the remote standoff laser instruments are deployed and *in situ* analysis performed is enclosed as best as possible. Most field campaigns showcased in the thesis have been conducted at sites under maintenance, thus

not accessible to the public. Within the churches, the small chapels are temporarily closed to churchgoers and fenced with objects such as tables, chairs, luggage cases, and roll-up banners. Appropriate PPE mentioned above is provided for the operators and observers (colleagues on site).